UNIVERSITY OF CAMBRIDGE

CRITICAL DYNAMICS OF ACTIVE PHASE SEPARATION

A SCALAR FIELD THEORY APPROACH

FERNANDO M. CABALLERO PEDRERO

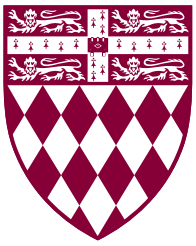

FITZWILLIAM COLLEGE

Dept. of Applied Mathematics and Theoretical Physics (DAMTP)
University of Cambridge

May, 2020

This thesis is submitted for the degree of *Doctor of Philosophy*.

Fernando M. Caballero Pedrero: *Critical dynamics of active phase separation,* A scalar field theory approach, PhD in Applied Mathematics and Theoretical Physics, © 2020

SUPERVISOR:
Prof. Michael E. Cates

LOCATION:
Fitzwilliam College, Cambridge

SUBMISSION:
May 2020

DECLARATION

This dissertation is the result of my own work and includes nothing which is the outcome of work done in collaboration except as declared in the Preface and specified in the text.

It is not substantially the same as any that I have submitted, or, is being concurrently submitted for a degree or diploma or other qualification at the University of Cambridge or any other University or similar institution except as declared in the Preface and specified in the text. I further state that no substantial part of my dissertation has already been submitted, or, is being concurrently submitted for any such degree, diploma or other qualification at the University of Cambridge or any other University of similar institution except as declared in the Preface and specified in the text.

It does not exceed the prescribed word limit for the relevant Degree Committee.

Fitzwilliam College, Cambridge, 2020

Fernando M. Caballero Pedrero

Critical dynamics of active phase separation
A scalar field theory approach
Fernando M. Caballero Pedrero

ABSTRACT

This thesis studies the critical properties of several systems under the overarching theme of active matter. These are systems that constantly consume energy at particle level and transform it into motion. Several field theories have been proposed as continuum descriptions of isotropic systems of self-propelled particles, that are able to reproduce some of the phenomena observed in these systems at particle level, mainly motility-induced phase separation (MIPS). This is a form of phase separation in the absence of attractive interactions that is not present in these systems' passive counterparts. These theories are built as extensions of models of equilibrium phase separation (Model B) that minimally break detailed balance.

This thesis addresses the question of how these field theories behave at criticality, in the transition between uniform and phase separated states, and whether this transition lies in the Ising-like universality class of the background equilibrium model, or instead belongs to a new universality class.

The first model analysed, named here conserved KPZ+, is a simplification of the main MIPS model studied, and proves to be a general model for surface growth with conserved mass, not present in the literature. This system has an Renormalization Group flow that, to one loop, shows a strong coupling regime in and above its critical dimension $d_c = 2$ that was not present in the previous systems considered to model this physical process. This strong coupling regime is also explored numerically, showing that the equation of motion indeed has a more complex phase diagram than it was thought for these surfaces.

The full field theory for MIPS is then analysed using Renormalization Group. The results are that, between 2 and 4 dimensions, a new fixed point appears as an extension of the Wilson-Fisher fixed point. This new fixed point rules a new transition to a strong coupling regime not present in the equilibrium Model B. The perturbative nature of the RG approach leaves the quantitative characterization of this phase as an open question, but the phase diagram obtained matches roughly the one explored numerically in the literature, and strongly suggests that the strong coupling regime represents a new universality class of nonequilibrium phase separation.

Finally, the entropy production rate (EPR) is studied for these active field theories close to the equilibrium critical points. The results indicate that the EPR per correlation volume can be constant or even diverge close to the equilibrium critical points, meaning that even though the dynamics of these systems are effectively in equilibrium, there is a nontrivial critical scaling for the EPR that is part of Ising-like universality classes.

PUBLICATIONS

The novel results of this thesis have been published in the following papers, which correspond roughly to Chapters 3, 4 and 5.

F. Caballero, C. Nardini, F. van Wijland, & M. E. Cates. *Strong Coupling in Conserved Surface Roughening: A New Universality Class?* Physical Review Letters, 121, 020601 (2018).

F. Caballero, C. Nardini, & M. E. Cates. *From bulk to microphase separation in scalar active matter: a perturbative renormalization group analysis.* Journal of Statistical Mechanics: Theory and Experiment, 2018(12), 123208 (2018).

F. Caballero, & M. E. Cates. *Stealth Entropy Production in Active Field Theories near Ising Critical Points.* Physical Review Letters, 124, 240604 (2020).

PREFACE

This thesis is made of six chapters. Chapters 1 and 2 introduce the topic of active matter and the techniques used in the thesis respectively. Chapter 3 to 5 roughly contain the novel results obtained from this work and published in the papers found in the Publications section. The last Chapter is dedicated to conclusions. The results of Chapter 3 were co-supervised by Cesare Nardini and Frédéric van Wijland, while the results of Chapter 4 were co-supervised by Cesare Nardini.

It is specified throughout the thesis what specific parts are original work or bibliographic review. The same applies to figures, which have been prepared for the thesis unless specified in each caption.

CONTENTS

1

INTRODUCTION

The physics of irreversibility is present in the theory of thermodynamics via its fundamental second law. However, thermodynamics initially dealt with only stationary equilibrium systems, for which the second law translates into a null change of entropy. This includes either systems that are in thermodynamical equilibrium, or processes that happen infintesimally slowly, allowing for the assumption that the system is in equilibrium at each point in time. Note that this assumption requires the process to be infinitely slow; in general any change of a real system will carry with it some, even if small, heat dissipation, and so an increase in entropy.

The study of systems out of equilibrium took off later in history, and its main difficulty is that, unlike in the case of equilibrium systems, nonequilibrium ones lack a universal mathematical framework with which we can calculate statistical quantities for an arbitrary model, i.e. we do not have a non-equilibrium version of Boltzmann's distribution.

Systems out of thermodynamic equilibrium comprise an extremely wide range of phenomenologies, and with that comes a similarly wide range of mathematical challenges to model, explain and understand them.

A rough classification of non-equilibrium phenomena is as follows. First, we can consider systems that are temporarily out of equilibrium, that it, systems that have been put out of equilibrium but are not kept out of it, so that they are relaxing back to equilibrium conditions. The second class would be systems that kept out of equilibrium continously. There are, in principle, several ways to do this.

One of the simplest to understand and analyse mathematically is to consider systems kept out of equilibrium by boundary conditions, e.g. gases in a container in which boundaries of the container are connected to heat reservoirs at different temperatures, thus producing steady currents within the system.

Historically these systems were among the first to be analysed mathematically, more specifically when they are still close to equilibrium. This allows to approximate entropy change by linear relations between the forces that are driving the system out of equilibrium (the boundary conditions), and the currents they produce (flows of heat). This work, developed by Onsager, was a big first step in the understanding of nonequilibrium physics [1].

There is another class of systems that are kept out of equilibrium due to the microscopic behaviour of their constituent particles and not any boundary conditions. These systems are made of particles that constantly dissipate heat. Thus if any part of the system is isolated, this isolated subsystem will still be out of equilibrium. As opposed to the previous class of systems, here there may not be obvious steady currents that point to a non-equilibrium situation.

The field of active matter deals primarily with this last class of systems. It is so far a very general and open definition and as such can include many, very different systems with very different phenomenology. Many examples come from biology, since we need systems in which each particle is, by itself, dissipating heat into the environment, typical examples being flocks of birds, where each bird consumes energy to transform into motion (i.e. to fly) [2, 3] or colonies of bacteria where each bacterium consumes energy from the medium to propel [4, 5]; but there are as well systems synthetically created in the laboratory, usually some kind of colloidal particle that can interact with its environment to dissipate heat [6].

Also, it is worth mentioning the classificaction made above can be vague at times, therefore should not be taken as a formal classification such that any system can be placed in a particular type unambigously. For example, as has been done experimentally, heat dissipation at particle level in a two-dimensional system (which would fall on the third class) could be induced by some energy input through a boundary condition on a third dimension, which could be argued to be a system in the second class. This is exactly what is done in [7, 8].

As mentioned above, biological systems have been one of the main driving forces in the field of active matter. Of these, a lot of work has revolved around the study of motile particles, intiated, or popularized, by the work of Vicsek and coworkers for the study of the dynamics of flocks of birds [9]. From this a big field arose studying the phenomenology of motility for spherical particles, particles with orientational order, particles with different interactions, etc. There are also many experimental studies, some of them cited above. We will from now on focus on this particular type of active matter systems: systems of motile particles with spherical symmetry. Coarse grained versions of these systems usually wash out the nonequilibrium aspect of it since no matter currents are visible at big scales, which does not happen when there is some alignment interaction, like systems of active nematics or the Toner & Tu model [3]. There are, however, a few experimental examples of self-propelled particles in which irreversibility is made visual macroscopically, usually using the fact that self-propelled par-

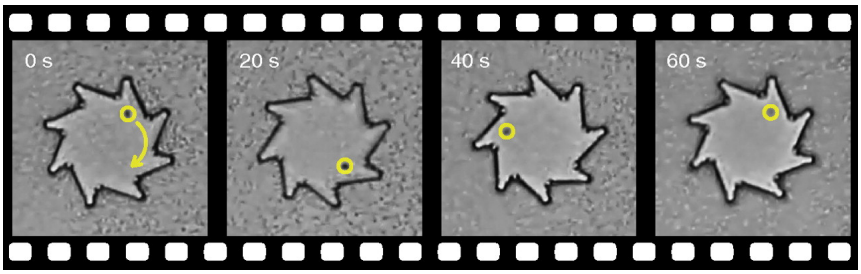

Figure 1.1: Self-propelled particles accumulate at sharp corners due to the persistence in their direction, and make the small ratchet rotate. This would be impossible in equilibrium, since it breaks time reversibility, each image is at different time instants. Taken from [10].

ticles tend to accumulate in places in which their motion is restricted due to the fact that their direction has long time correlation (i.e. they will accumulate at sharp corners). For instance, Figures 1.1 and 1.2 show how this fact makes self-propelled particles (*E. coli*) rotate a gear [10], or how sharp funnel like structures can be used to accumulate them [11].

In the next section we will explain in detail the main phenomenon this thesis studies, motility induced phase separation, which is also possible only in systems out of equilibrium and in which nontrivial matter currents can also be found macroscopically.

1.1 MOTILITY INDUCED PHASE SEPARATION

One major class of active matter systems, and one of the most studied, consists of those made of self-propelled particles. In this case, each individual particle will consume energy via some interaction with the environment to turn part of that energy into motion.

This gives rise to many interesting collective behaviours that cannot be present in the systems' equilibrium counterparts, and one of them, that this thesis will mainly focus around, is known as motility induced phase separation.

This kind of phase separation occurs in systems made of self-propelled particles, in the absence of attractive interactions, making it somewhat unexpected at first. If particles are able to display other forms of ordered states, like nematic or polar order, then they will have a more complex phase diagram, but we will focus on the simplest case, that of spherical particles with self-propulsion and no polar or nematic interactions, so that any large scale correlations that appear have to be isotropic.

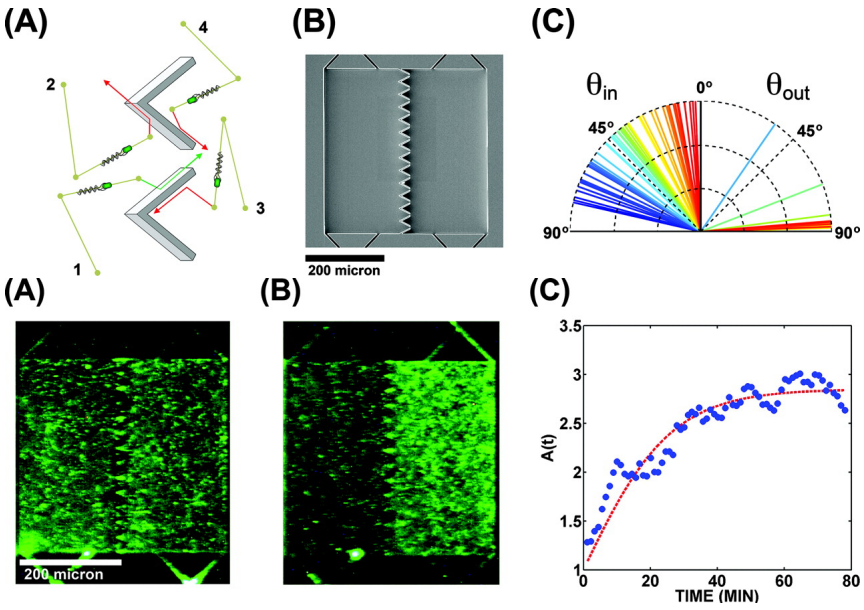

Figure 1.2: The funnels on top, arranged in a line, allow self-propelled particles to flow mainly in one direction, also due to the persistence in their direction of movement, increasing the density only in half of the space they occupy. This would be impossible in equilibrium where the density of, for example, Brownian particles, would be constant in space. The bottom row of images shows the density at an initial time (A), and after 80 seconds (B). Taken from [11].

The self-propulsion can be modelled in different ways. Two typical ones give rise to two very studied systems, run and tumble particles (RTPs), and active Brownian particles (ABPs) [12]. The first, RTPs, are particles that move in a straight line and, with a rate α, change direction from the old one to a random one. ABPs move with a velocity v, where the orientation of this velocity, ϑ, undergoes a Brownian motion, $\dot{\vartheta} = \xi$, for a white Gaussian noise ξ.

To illustrate this, Figure 1.3 shows a snapshot of a simulation of particles with this kind of self-propulsion, in the part of its parameter space where it shows phase separation. These particles have self-propulsion with Brownian noise in its direction, so they are ABPs, and the only interaction between particles is hard core repulsion, corresponding to a potential energy that is 0 if the particles do not overlap and ∞ if they do. In this particular case, the system has 300,000 particles, with a radius of $r = 0.06$, the systems side is $L = 102$, and the rotational diffusion constant is 0.3. It clearly shows phase separation into dilute and dense phases.

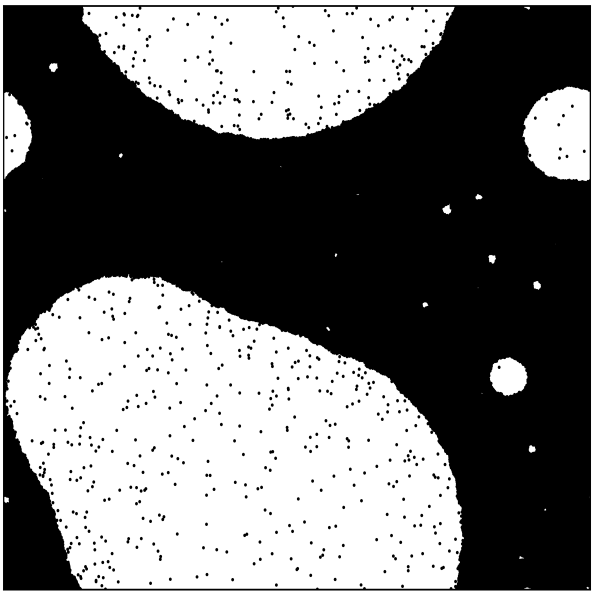

Figure 1.3: An instance of MIPS in a simulated system of self-propelled particles with periodic boundary conditions.

Of course, depending on the parameters, we observe, as we would expect, anything from full phase separation to uniform states. Figure 1.4 shows snapshots of simulations for several configurations.

The mechanism by which these systems show phase separation in the absence of attractive interactions between the particles can be intuitively understood in terms of the two main time scales that these systems have. One of them is the typical collision time between two particles and the other is the typical time in which the velocity of the particle decorrelates with itself, t_d. This time will be $t_d \sim \alpha^{-1}$ for RTPs and $t_d \sim \tau_\vartheta$ for ABPs.

When a collision happens, unlike in an equilibrium system in which particles display Brownian motion, the particles will stay together for some amount of time, since their velocity has a persistence time. Intuitively, if this time is bigger than the typical time between collisions, then clusters will form, and new particles will come in to the cluster before inner particles have time to turn around and leave.

It is important to note that this phenomenon is a collective behaviour that cannot be deduced from the dynamics of a single particle. Each single

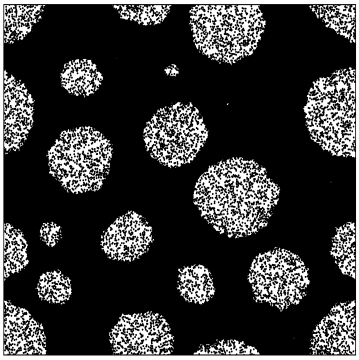

Number of particles: 300.000,
Rotational diffusion: 1.5.

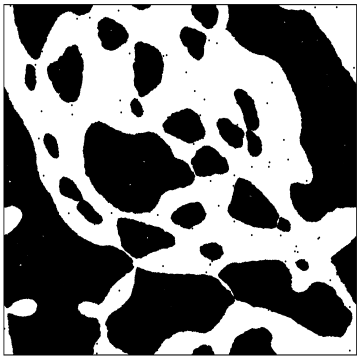

Number of particles: 300.000,
Rotational diffusion: 0.06.

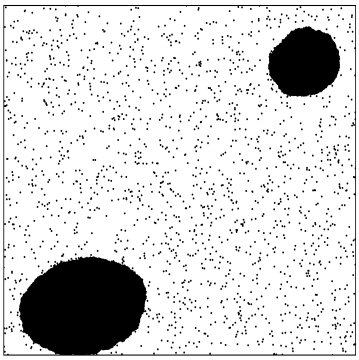

Number of particles: 60.000,
Rotational diffusion: 0.3.

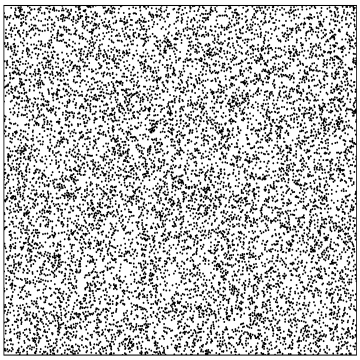

Number of particles: 12.000,
Rotational diffusion: 0.3.

Figure 1.4: Several instances of the phase separation of self-propelled particles for different total densities, before reaching steady state. The last one is an instance of low density where no phase separation occurs. All systems are of the same size ($L = 102$) and particle radius is also fixed ($r = 0.06$)

particle for both ABPs and RTPs behaves Brownianly at large scales of space and time. In particular, it can be shown [12, 13] that the dynamics of a single RTP can be coarse grained to the dynamics of a Brownian particle with a diffusivity of $D = v_0^2/(d\alpha)$, where v_0 is its velocity and d is the dimension of the system. And likewise an ABPs dynamics can be coarse grained to the dynamics of an RTP upon the substitution $\alpha \leftrightarrow (d-1)D_r$, where D_r is the rotational diffusivity of the ABP.

The most naive comparison of these timescales is to take t_d/t_c and argue that this ratio will set whether there is phase separation or not. In fact, this can be related to the more usual parameter used to study this kind of phase separation which is the Péclet number. This parameter, usually used as a dimensionless number to compare advection with diffusion as means of transport in a system, can be used here in a similar way, comparing translational diffusion with the diffusion of the direction of the particle [13]. The Péclet number, with σ being the diameter of the particle, is defined as follows

$$\mathrm{Pe} = \frac{3v_0}{\sigma D_r}.$$

Figure 1.4 shows more simulations for several values of the Péclet number (by changing the value of D_r) showing that it indeed rules the onset and stability of the phase separate state. The phase diagram as a function of the Péclet number and the volume fraction (or density) of the system, has been studied before in the case of active Brownian particles [13]. It has a phase diagram with a region in which the uniform state in unstable and the system will phase separate, as shown in figure 1.5. The tip of this region points to a second order phase transition, with scale invariance and critical properties.

This is somewhat equivalent to what we find in many equilibrium systems, such as standard, equilibrium phase separation. For instance, one of the most simple descriptions of symmetric phase separation of two species is a ϕ^4 theory, called Model B, that will be reviewed below in more detail. Setting a quench by tuning the temperature (or mass) of the theory will produce a phase diagram qualitatively similar to the one we find in MIPS; for a temperature that is low enough the uniform state can become unstable, and we find a second order phase transition for a given value of these parameters (usually setting the mass and the field to 0).

This equivalence is only qualitative, since the phase separated state is fundamentally different than the one that might be found in an equilibrium system. As it comes from nonequilibrium dynamics, we know that at least microscopically, there are net currents in the system, meaning that detailed

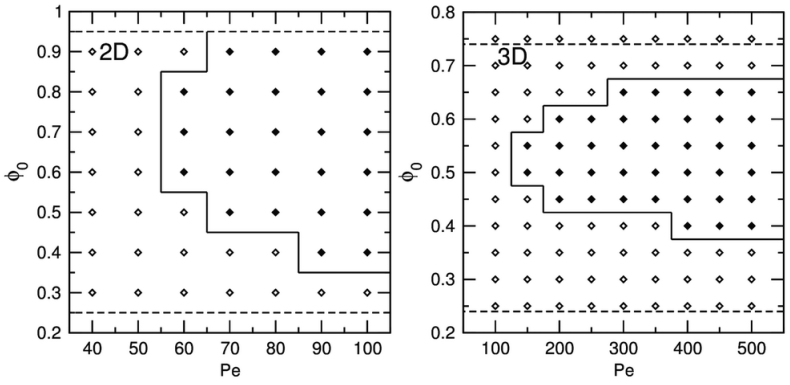

Figure 1.5: Phase diagram of a system of ABPs in 2 and 3 dimensions as a function of the Péclet number and the density, where empty points mean uniform phase and filled points mean phase separated state. Taken from [13]

balance is broken, which is an intrinsic property of nonequilibrium physics and simply means that given any two states A and B, the probability of observing the system move from A to B may not be the same as the probability of observing it move from B to A. An equilibrium system will obey detailed balance for any pair of states. There is a difference, however, between a system breaking detailed balance and currents being visible macroscopically. It may be the case that when a system is coarse grained and looked at from larger scales no currents are visible and the system seems to regain detailed balance again. This sometimes allow us to map a non-equilibrium system to a equilibrium one in certain regimes and obtain effective equilibrium models for systems that are microscopically out of equilibrium [14, 15, 16, 17].

As mentioned in the introduction, there are sometimes no visible signs of irreversibility when one looks at how these systems behave at big scales. Sometimes, these currents can be made more obvious macroscopically, like it was also mentioned above, in Figures 1.1 and 1.2, but in some other systems this does not happen, for example in Active Model B [18], which will be described below. This does not exactly mean that the system is effectively equilibrium and there are certain subtleties with regards to how the entropy production of this systems evolves after coarse graining. This will be discussed later in Chapters 4 and 5.

In the case of MIPS that has been shown in this section, this irreversibility can actually be observed in the phase separated state in the form of a different, more subtle current, that would not be possible in an equilibrium system. What happens here is that, within the dense phase, bubbles of diluted phase coalesce until they reach a certain size (they do not grow

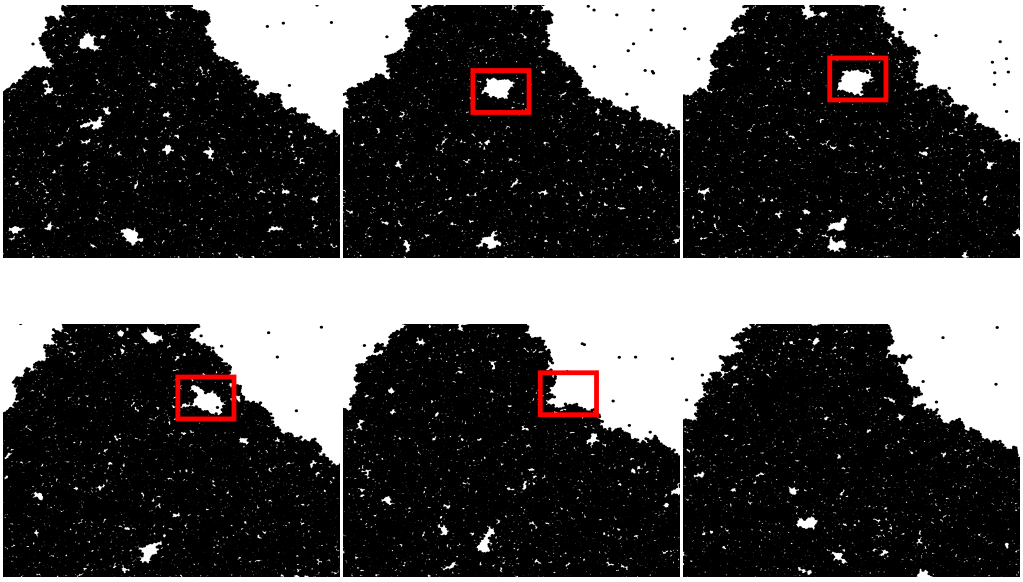

Figure 1.6: Irreversible process in the bulk of of the dense phase in MIPS. Time order is left to right and top to bottom. The system size is $L = 102$, and 30.000 particles of radius $r = 0.3$. Images are zoomed in and cropped from the whole system, which is ~ 2 times bigger than what is shown. These bubbles are formed and expelled from the bulk continuously in this simulation.

indefinitely), and move in what seems a Brownian motion within the dense phase until they reach the interface and are expelled into the dilute phase. The reverse is never observed, that is, the dense phase never absorbs a bubble out of the dilute phase and dissolves it in the bulk. This process is shown in Figure 1.6, in a simulation with bigger particles so that these bubbles can be seen better. Observe, though, that this can also be seen in the bulk in the images above, Figure 1.4, for some values of the simulation parameters, and has been observed as well in the literature for particle level simulations [13, 19, 20, 21].

This thesis deals with the critical properties of MIPS at its phase transition (at the tip of the instability region of the phase diagram). This includes several questions that we consider. One of the first that comes to mind is then whether or not the phase transition between these states lie in the same universality class as the continuous phase transition of its equilibrium counterpart (which is the universality class of the conserved Ising model).

A different question is concerned with what happens macroscopically when the system seems to recover equilibrium properties. This is a feature

of the models we use, as well as others that can be mapped to equilibrium systems as mentioned above. This question is addressed in Chapter 5 studying the entropy production, which will be defined in the following section along with the models we use.

There are different ways to obtain field theories for MIPS, and the one we will use here, explained in detail in the next section, is built on scalar field theories that break detailed balance locally via nonlinearities of the field. Another popular way of obtaining these theories is known as quorum sensing, which consists of having a systems of self-propelled particles with a velocity that decreases as a function of the local density. This is observed in experiments, usually linked to chemotaxis [22], and has been studied in detail in the literature [12, 5].

1.2 MODELS

Since we are going to study the critical properties of MIPS using renormalization group, we need to first set a proper continuous theory for our systems. This will allow us to apply all the machinery of RG as it has been used in other fields, mainly in statistical and high energy physics.

There is a lot of variety when it comes to field theories for active matter. Probably one of the first worth mentioning is the Toner & Tu model [3, 23], a field theory developed to describe bird flocking. This is a hydrodynamic model with two fields (one for density and one for velocity), similar to the Navier-Stokes equation for an incompressible fluid, devised following the work of Vicsek and coworkers based on particle models [9].

The approach for MIPS is, in principle, simpler, since a system with the kind of MIPS we aim to describe has to remain isotropic in both coexisting phases. We will build our model taking as a starting point what is known as Model B [24]. This model has the following dynamical equation:

$$\begin{aligned} \dot{\phi}(r,t) &= -\nabla \cdot J(r,t), \\ J(r,t) &= -\nabla\mu(r,t) + \Lambda(r,t), \\ \mu &= \frac{\delta \mathcal{F}[\phi]}{\delta \phi}. \end{aligned} \tag{1.1}$$

The first line is a continuity equation, since matter is conserved, for the concentration field $\phi(r,t)$. This field will be symmetric around 0 for Model B, but this can be easily mapped to a real concentration field $\rho(r,t)$ that varies between low and high density values ρ_L and ρ_H by the substitution $\phi/\phi_B = (2\rho - \rho_H - \rho_L)/(\rho_H - \rho_L)$, where ϕ_B is the value of the field at

the minima of the free energy. The second one just writes that the current is proportional to the gradient of a chemical potential, and $\Lambda(r,t)$ is a white Gaussian noise, with the following correlation:

$$\langle \Lambda_i(r,t)\Lambda_j(r',t')\rangle = 2D\delta_{ij}\delta(r-r')\delta(t-t'), \tag{1.2}$$

with D being the strength of the noise. The third line of equation 1.1 writes μ as the functional derivative of a free energy $\mathcal{F}[\phi]$. This is crucial since this particular equation then makes the dynamics equilibrium, with a Boltzmann distribution of steady states associated with the free energy, so that the stationary probability of a given state $\phi(r,t)$ is

$$P(\{\phi(r,t)\}) = Z^{-1}e^{-\mathcal{F}[\phi]}, \tag{1.3}$$

where Boltzmann's constant is set to 1 and the temperature is absorbed in the parameters of the free energy.

Naturally, we will eventually break this equilibrium structure, but it is worth describing first the nature of Model B. The free energy that finally defines Model B is the free energy of standard ϕ^4 theory, or Landau-Ginzburg free energy:

$$\begin{aligned}\mathcal{F}[\phi] &= \int d^d r f[\phi] + \frac{\kappa}{2}(\nabla\phi)^2 \\ &= \int d^d r \frac{a}{2}\phi^2 + \frac{u}{4}\phi^4 + \frac{\kappa}{2}(\nabla\phi)^2,\end{aligned} \tag{1.4}$$

which for the sake of studying critical phenomena can be justified as a series expansion in the field and its gradients, assumed to be small around continuous phase transitions.

This free energy has a very well known behaviour in a mean field approximation. Minimizing it for uniform values of the field in the bulk shows that there are two values the field will take, either 0 or $\pm\phi_B = \pm\sqrt{-a/u}$, for positive and negative a respectively, as shown in figure 1.7.

This points to a continuous phase transition when $a = 0$, since ϕ_B tends continuously to 0 as we take a to 0. From the form of the free energy we can extract some of the behaviour of the main quantities we can measure across or close to the transition. First, observe that because a close to 0 sets the transition across the critical temperature, then close to the transition we must have that $a \propto (T - T_c)$, where T_c is the critical temperature.

With this we can extract how the field behaves close to the transition, just by minimizing the bulk free energy density f, such that $\mathcal{F} = \int d^d r f$ for uniform states. We have that the free energy is minimized at mean field

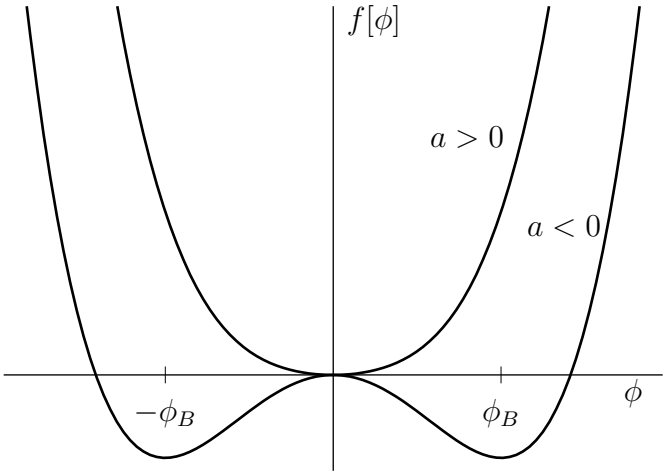

Figure 1.7: Typical double well potential describing continuous phase transitions according to the Landau-Ginzburg free energy.

level when $a\phi + u\phi^3 = 0$, from here we immediately get that close to the transition,

$$\phi \sim (T - T_c)^{1/2}. \tag{1.5}$$

Two more important quantities can be calculating by coupling the field linearly to an external field B, i.e. adding a term $-\int d^d r B\phi$ to the free energy. This allows us to get, from the same minimization principle that, close to the transition,

$$\phi \sim B^{1/3}. \tag{1.6}$$

And lastly we can calculate the susceptibility, defined as $\chi = \partial\phi/\partial B$, by just derivating the minimization condition with respect to B, we obtain that,

$$\chi \sim (T - T_c)^{-1}, \tag{1.7}$$

which gives the divergence of the susceptibility as we approach the transition point. This, of course, defines the mean field critical exponents of the ϕ^4 theory. In the next chapter we will introduce these more formally in the context of renormalization, and our aim is to calculate these for MIPS.

One last thing to introduce before building our MIPS field theory is the concept of a dynamical action. For this we follow the work done in [25].

The reason the free energy description is not enough is merely due to the fact that we look at the dynamics of the system, so that any dynamic effect

will be lost in we just look at the free energy. This is of course OK if we look at an equilibrium system at the steady state, since we will observe exactly the behaviour predicted by the free energy, but it will not be enough if we want to look at time-dependent phenomena and, once the system is out of equilibrium, studying a free energy will be just not possible.

A dynamical action is simply another kind of action that gives the distribution of dynamical paths instead of single-time states, so a dynamical action $\mathcal{G}[\phi]$ is such that the probability of observing a path for ϕ, or the probability that the path takes a certain value $\phi(r,t)$ for some volume and time interval is $P[\phi] = \exp(-\mathcal{G}[\phi])$.

This can be done through the Onsager functional as first step, which is built by creating a distribution that has the same noise strength as the equation of motion, equation 1.1. This functional is trivially

$$\mathcal{W}[\eta] = \exp\left(-\frac{1}{4}\int d^d r dt\ \eta(2D\nabla)^{-2}\eta\right), \tag{1.8}$$

where ∇^{-2} just represents the inverse Laplacian, so that $\nabla^{-2} f = g$ if $\nabla^2 g = f$, and that makes sure that we recover the noise correlations of the equation of motion. The definition of ∇^{-2} used here involves in practice a simple q^{-2} prefactor in Fourier space, although more formally the relation above implies that

$$g(r) = \int d^d r G(r-r') f(r'), \tag{1.9}$$

where $G(r)$ is the Green's function of the Laplacian that makes the above a Coulombian integral.

We have conveniently defined a new noise $\eta = \nabla \cdot \Lambda$, that by its definition has the following noise correlation

$$\langle \eta(r,t)\eta(r',t')\rangle = 2D(i\nabla)^2\delta(r-r')\delta(t-t'). \tag{1.10}$$

If we now consider the noise in equation 1.8 to be a functional of the fields defined by the equation of motion itself, then we immediately arrived as the Onsager-Machlup functional:

$$\begin{aligned}\mathcal{G}[\phi] = \exp\Bigg[-\frac{1}{4}\int d^d r dt \Big(\dot{\phi} + \nabla \cdot J_D\Big) \times \\ \times \frac{\nabla^{-2}}{2D}\Big(\dot{\phi} + \nabla \cdot J_D\Big)\Bigg],\end{aligned} \tag{1.11}$$

where J_D is the deterministic current, such that the equation of motion is written as $\dot{\phi} = -\nabla \cdot J_D + \eta$.

This is in principle already a complete description of dynamical paths of this system. It is, however, a bit inconvenient due to a couple of reasons. The first is that, because of mass conservation, we have a ∇^{-2} which creates low wavenumber divergences in Fourier space, since it involves a q^{-2} prefactor. The second reason is that, because this functional comes from the *square of the dynamics*, it has nonlinearities that are of higher order and more uncomfortable to work with than those we found in the equation of motion or the free energy.

For this reason, we go a step forward and use the standard trick, known as Martin-Siggia-Rose formalism of introducing an auxiliary field, $\tilde{\phi}$, to uncomplete the square [25]. This allows us to write the Martin-Siggia-Rose action

$$\mathcal{A}[\tilde{\phi},\phi] = \int d^d r dt \Big[\tilde{\phi}(r,t) \left(\dot{\phi}(r,t) + \nabla \cdot J_D \right) + \tilde{\phi}(r,t) D \nabla^2 \tilde{\phi}(r,t) \Big], \tag{1.12}$$

which is our final result for the dynamical action we will use.

This allows for the usual calculation of the expected value of any arbitrary observable $\mathcal{O}$:

$$\langle \mathcal{O} \rangle = Z^{-1} \int D[i\tilde{\phi}] D[\phi] \mathcal{O} e^{-\mathcal{A}[\tilde{\phi},\phi]}, \tag{1.13}$$

where Z is the dynamical partition function.

We are now in a position to build a field theory for MIPS, which will be built on Model B.

1.2.1 *Active Model B+*

As mentioned above in this section, the fact that Model B's dynamics from equation 1.1 comes from a free energy means that the steady state distribution of the system is an equilibrium, Boltzmann distribution. Since this system describes passive phase separation, it seems like a good starting point for an active counterpart, and the way we can build it is by breaking this free energy structure. So by adding terms to the dynamics that cannot be written as the functional derivative of a free energy, we break the Boltzmann' description of the system, and drive the system out of equilibrium, breaking time reversal symmetry (TRS).

The choice of what terms we include follows the Landau-Ginzburg expansion of the free energy as a series in the field and its gradients, i.e. we

consider the dynamics as this series and add the lowest order terms that break time reversal symmetry. The only thing we require of these terms is that they are local and that they preserve mass conservation. Doing that, to lowest order, we obtain Active Model B+ (AMB+):

$$\begin{aligned}\dot{\phi} =&\nabla^2\left[a\phi + u\phi^3 - \kappa\nabla^2\phi\right] + \eta \\ &+ \lambda\nabla^2(\nabla\phi)^2 + \zeta\nabla\cdot\left[\nabla\phi\nabla^2\phi\right] + \frac{\nu}{2}\nabla^4(\phi^2).\end{aligned} \tag{1.14}$$

The first line is Model B, and the second line are the three terms that we can write to lowest order that break TRS and respect mass conservation. Some comments about each of them are due. The λ term is a change to the chemical potential, since it has ∇^2 in front of it; this term therefore represents activity since $(\nabla\phi)^2$ cannot be written as a functional derivative.

The second term (ζ) is somewhat different in that it cannot be written as a Laplacian of a local function, so that it is a non-equilibrium contribution to the current, and not the chemical potential. This is fundamentally different because it means we now have dynamics that may show a nonzero rotational, or circulating currents. As we may see, this term is also responsible for many interesting phenomena about AMB+.

The last term is there only for completeness, since the three of them make all independent terms at this order in fields and gradients. If we expand the derivatives it produces $\nabla^2(\nabla\phi)^2 + \nabla^2(\phi\nabla^2\phi)$. The first of this is a contribution to λ and the second is actually an equilibrium term, coming from the functional derivative of $\int \phi(\nabla\phi)^2$, which could be understood as a higher order term in an expansion of the interface tension κ, which would now be $\kappa(\phi) = \kappa + \kappa_1\phi + \mathcal{O}(\phi^2)$.

In other words, we could write AMB+ without the ν term by writing the following free energy

$$\mathcal{F}_{\text{B+}} = \int d^d r \frac{a}{2}\phi^2 + \frac{u}{4}\phi^4 + \frac{\kappa + 2\kappa_1\phi}{2}(\nabla\phi)^2, \tag{1.15}$$

where $\kappa_1\phi$ has been added as a higher order in the field correction to κ. The reason we are going to use ν instead of κ_1 is that the mathematical analysis is rendered a bit simpler this way.

One last thing to mention about this terms is that one of the basic symmetries of Model B, that of $\phi \to -\phi$ is now broken and substituted with the symmetry $(\phi, \lambda, \zeta, \nu) \to -(\phi, \lambda, \zeta, \nu)$.

This model has been introduced in the literature in a staged manner. The first version studied is known as Active Model B [18], obtained by setting $\zeta = \nu = 0$. Full AMB+ was proposed and studied numerically in [26], and has an interesting phase diagram.

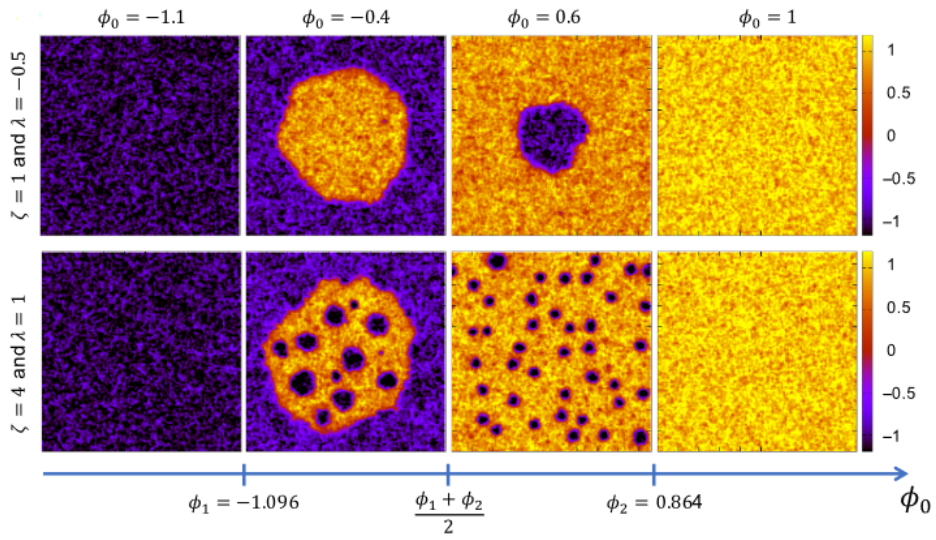

Figure 1.8: Different phases of AMB+, including the new phases where Ostwald ripening is reversed. In this new phases, the steady state involves the presence of the small droplets that cease to grow with time. Taken from [26].

If we set $\zeta = 0$, we obtained a steady state that looks qualitatively similar to that of Model B with a quench; quantitatively, it produced a phase separation with a pressure difference at each side of the interface, with the pressure $p = \phi\mu - f$, as defined in reference [18]. The coexistence region can be obtained by an *uncommon* tangent construction [18] that comes from that pressure change.

If we increase ζ, however, we obtain completely different dynamics. This was done in [26], and it was observed that while for some regions of parameter space the system phase separates similarly to Model B, for some other regions it creates incomplete phase separation, where Ostwald ripening is reversed. This phase can be seen in figure 1.8.

Notice that, in the region of parameter space where there is phase separation and reversed Ostwald ripening, the steady state dynamics of the system strongly resemble the MIPS we find in ABPs. This bubbles of phase A coalesce in the bulk of phase B until they reach a certain size and then they move until they are expelled in the bulk of phase A. The reverse is, like with ABPs, never observed, and so this is a macroscopic realization of broken TRS.

Our aim is therefore to describe and understand the critical properties of this system in the transition between its different phases. Before intro-

ducing the method of RG as we will apply it to AMB+, we will introduce a second model we will study, mathematically related to AMB+.

1.2.2 *Conserved KPZ+ equation*

This second model is mathematically obtained from AMB+ by simply cancelling out the cubic nonlinearity of the equation of motion ($u = 0$), as well as the ν nonlinearity, and sending the free energy to critically at $a = 0$. The resulting equation is

$$\dot{\phi} = -\kappa\nabla^4\phi + \lambda\nabla^2(\nabla\phi)^2 + \zeta\nabla\cdot[\nabla\phi\nabla^2\phi] + \eta. \tag{1.16}$$

Notice that by doing this we have lost the physical description of a density field, since the polynomial part of the free energy is necessary to bound the values of the field. The free energy is now unbounded below and depends only on gradients of the fields, which means that we cannot interpret our field as a concentration field anymore. The model can, however, be reinterpreted as a description of interfacial growth.

For now, we only present this model mathematically. It will be studied in its own right due to its physical interest, and also as a simplification of the results and techniques used for AMB+. All the reasoning behind this model is presented alongside its analysis in Chapter 3.

1.3 PLAN

The objective of this thesis is to study the critical properties of these models. The next Chapter will introduce the main technique used for this (Renormalization Group), before jumping into the study of the simpler cKPZ+ in Chapter 3, and then the full study and analysis of AMB+ and its entropy production in Chapters 4 and 5.

2

RENORMALIZATION GROUP

As explained in the first chapter, the object of this thesis is the study of the critical properties of AMB+ (and similarly cKPZ+) in its phase transition between the different phases it displays, which are from standard uniform to phase separated states, and from these to phase separated with reversed Ostwald ripening. The main tool to study critical properties is Renormalization Group, which this chapter describes in the particular way in which it is going to be applied throughout this thesis.

The main idea is that the mean field theory described in section 1.2 for the ϕ^4 theory may produce wrong results for the phase transition. The reason is that MFT neglects fluctuations in the system, but still gives back results that point to strong fluctuations. In particular, equation 1.7 tells us the susceptibility diverges as we approach the critical temperature. This could not be possible without fluctuations and so a more detailed study of the system should take into account the effect of fluctuations in the phase transition.

Some information can be extracted from calculating explicitly the susceptibility (related to the propagator of the system). This can be calculated from equation 1.1 in a direct way, by transforming to Fourier space with a source term in the free energy, as described after equation 1.5, and calculating $\delta\phi/\delta B$. We get

$$\chi(q) = \frac{1}{a + u\phi^2 + \kappa q^2} = \frac{1/\kappa}{\xi^{-2} + q^2}, \tag{2.1}$$

where we have defined the correlation length $\xi = \sqrt{\kappa}(a+u\phi^2)^{-1/2}$. Using the value of ϕ that minimizes $\mathcal{F}$, we get that the correlation length behaves as

$$\xi = (T - T_c)^{-1/2}. \tag{2.2}$$

Notice that this is indeed the only length scale of our system. If we calculate the two point correlation function, for $a > 0$, we will find that it equals

$$\langle \phi(q)\phi(q') \rangle = (2\pi)^d \delta^{(d)}(q + q') \frac{2D/\kappa}{\xi^{-2} + q^2}, \tag{2.3}$$

where a zeroth order correlator $C_0(q)$ is usually defined through the right hand side, $C_0(q) = 2D\kappa^{-1}(\xi^{-2} + q^2)^{-1}$. Correlations then decay exponentially and ξ is the length at which they become negligible. This particular form of correlation is known as Ornstein-Zernicke correlation [27].

By taking a look at the susceptibility of the system at small q (i.e. the susceptibility at large scales), we find that the susceptibility behaves as $\chi \sim (T - T_c)^{-1}$, so it diverges at the critical temperature.

These power laws are part of a more general hypothesis, known as the scaling hypothesis, that consists of assuming that the singular part of the free energy (which produced nontrivial behaviour), close to criticality, is homogeneous under scaling transformations. This is directly related to the scale invariance of systems at criticality, since this homogeneity comes into correlation functions, meaning a given correlation function of separation $A(r)$ will be homogeneous in r

$$A(r) = |r|^{\gamma_A} f(r/\xi), \tag{2.4}$$

where f is a scaling function. Observe that the ratio between A measured at two different scales $A(\lambda r)/A(r)$ does not depend on r if the correlation length $\xi \to \infty$, but only of the ratio of the two scales, with some critical exponent γ_A. Notice that this can only be achieved continuously for power laws, and these exponents for different observables are the critical exponents we are interested in finding.

In the case of dynamic systems, the scaling hypothesis is the same, except now the time dependence of correlation functions close to criticality has a new exponent, z, called the dynamic exponent, that relates the typical time of correlation t_c to the correlation length ξ, via $t_c \sim \xi^z$.

For instance, if $G(\tau, q, \omega)$ is the response function of a system, when τ is the parameter that sets the transition (typically a reduced temperature), and q and ω are wavevectors and time frequencies, then close to the transition, it must behave as follows

$$G(\tau, q, \omega) = |q|^{\eta-2} f_G(q\xi, \omega\xi^z/(\Omega K^z)), \tag{2.5}$$

where η is the critical exponent of the field (related to χ), and f_G is a scaling function, where Ω and K would be parameters with dimensions of frequency and length respectively.

This scale invariance is also at the heart of the Renormalization Group technique, since, for a system to display scale invariance, its action must also have this invariance. In other words, if the action $\mathcal{A}[\phi, g_i]$ depends on a field ϕ and other parameters g_i, after doing a scale transformation on the

system at the critical point, which includes transformations for the field and parameters $\phi \mapsto \phi'$ and $g_i \mapsto g_i'$, it must be true that $\mathcal{A}'(\phi', g_i') = \mathcal{A}(\phi, g_i)$.

Renormalization is based around this idea. We will find how the different parameters change under scale transformations, and by finding the fixed points of this transformation we find points in parameter space at which the system is scale invariant. This scale invariance can be either trivial, in the sense of a vanishing correlation length (like the very high temperature state of an Ising system), or nontrivial, with a diverging correlation length. The second case is usually the more interesting one, since these fixed points point to continuous phase transitions. In these phase transitions a diverging correlation length together with scale invariance imply certain fractal structure in the states of the system, as they are usually seen in, for instance, the Ising model. This fractality is also observed in a different way when we measure correlations in the systems, since these start to behave, close to criticality, as objects with anomalous dimensions (typically found as corrections to the natural dimension of the correlation function) that we will calculate below.

The particular methodology is based heavily on Kadanoff's view of the Renormalization Group, which is one particular way of finding how these parameters change under scale transformations. This involves two steps.

The first step is usually called *blocking*, and it consists of reducing the number of degrees of freedom of our system, by building blocks of several degrees of freedom that we will reduce to only one. The simplest example is, again, the Ising model, with which we can make blocks of $n \times n$ spins that we consider as a single spin in the new, reduced system, and giving it the value of, for example, the majority of the spins that form the block.

In continuous systems this step is usually carried out by having a theory defined up to some upper cutoff in wavelength, say Λ, and by integrating out of the partition function the degrees of freedom in a thin shell between Λ/b and Λ for some $b > 1$. This integration will influence the degrees of freedom of lower wavelengths via some new interactions or contributions to the present interactions. This step can be technically complicated and will have to be done perturbatively, as will be exemplified in the next section.

The second step is to rescale back all wavelengths q to restore the original cutoff ($q \mapsto bq$), so that we have a theory defined in the same range of wavelengths. After doing so we will obtain a number of terms as a product of both steps that must be reabsorbed by the parameters of the system to obtain the *rescaled* parameters.

These rescalings define what is known as the RG flow of the parameters, and by finding fixed points of this flow we find parameter values of the system for which it is scale invariant. The main idea is that by performing succesive RG steps, we remove the microscopic details of the model, thus if the system lies in a scale invariant point of diverging correlation length (to be further explained below), succesive RG steps will neglect all contributions to observables that do not diverge as the system is taken to the point of diverging correlation length, so all nonuniversal quantities that depend on short scales or the short cutoff are lost, even if they are large. This will we important in Chapter 5 when discussing the sign of the diverging part of the entropy production rate of the models presented in the previous Chapter.

2.1 PERTURBATIVE APPROACH

The step in which we integrate out degrees of freedom described in the previous section can hardly ever be done exactly, and some approximation is necessary.

The one performed here is completely standard, and we will, at different stages, use two slightly different but completely equivalent formalisms.

The first is the most direct one, that can be done in the equation of motion directly, and it follows the steps of other past works [28, 29].

Consider an arbitrary first order (in time) stochastic PDE

$$\dot{\phi} = -L\phi + F[\phi] + B + \eta, \tag{2.6}$$

where we have split the deterministic dynamics into linear (L) and nonlinear (F) parts, and where the noise η can in principle be conserved or nonconserved. We also allow for an external field, B, coupled linearly to ϕ in the free energy, that appears then as a constant in the equation of motion.

Our aim is to be able to give an expression for any arbitrary correlation function of the field ϕ. The procedure is as follows. First we work with our equation in Fourier space. After transforming the fields to Fourier space $\phi(r,t) \rightarrow \tilde{\phi}(q,\omega)$ (although we will just write ϕ instead of $\tilde{\phi}$), we can rewrite equation 2.6 as

$$\phi = \phi_0 + G_0 B + G_0 F[\phi], \tag{2.7}$$

where a few new definitions have been introduced, like the linear propagator G_0

$$G_0(q,\omega) = \frac{1}{-i\omega + L}, \tag{2.8}$$

where L is now just a function of the system parameters and the wavevector q. We have also introduced the linear, or zeroth order field $\phi_0 = G_0\eta$. Notice that ϕ_0 is actually the solution of the linearised equation, and that it is just a Gaussian noise, so we immediately know all correlation functions of the linear theory. Lastly, $F[\phi]$ in equation 2.7 will be a sum of convolutions of ϕ.

The perturbative approach can now be carried on the parameters of $F[\phi]$. This is done by iterating equation 2.7, by introducing the left hand side of the equation into each field of $F[\phi]$, and truncating the series after reaching the desired order. The most simple example is the correlator, related to the susceptibility, and can easily be illustrated with an example. Since AMB+ is built around equilibrium Model B, we will use that as an example. The equivalent of equation 2.7 is then

$$\begin{aligned}\phi = \phi_0 &+ G_0 B \\ &+ uG_0 \int_{q',q''} \phi(q',\omega')\phi(q'',\omega'') \\ &\qquad \times \phi(q-q'-q'', \omega-\omega'-\omega''),\end{aligned} \tag{2.9}$$

with

$$\begin{aligned}G_0 &= \frac{q^2}{-i\omega + q^2(a+\kappa q^2)}, \\ C_0 &= \frac{2Dq^2}{\omega^2 + q^4(a+\kappa q^2)^2}, \\ \phi_0 &= G_0\eta/q^2,\end{aligned} \tag{2.10}$$

and where we shorten the notation of the integral as follows

$$\int_{q',\ldots,q^{(n)}} = \int \frac{d^dq' \ldots d^dq^{(n)} d\omega' \ldots d\omega^{(n)}}{(2\pi)^{(d+1)}}. \tag{2.11}$$

The linear correlator C_0 is defined with respect to the two-point correlation functions, as follows

$$(2\pi)^{d+1}\delta^{(d)}(q+q')\delta(\omega'+\omega')C_0(q,\omega) = \langle\phi_0(q,\omega)\phi_0(q',\omega')\rangle. \tag{2.12}$$

Notice the factors of q^2 due to conservation of ϕ. Now we just have to iterate this equation to get an approximation of the correlator as a series in u. Suppose we want to calculate the correlator to order u. To this order we

just need to iterate once and ignore all terms of order u^2. Doing this, the dependence on ϕ disappears from the left hand side

$$\begin{aligned}\phi = \phi_0 &+ G_0 B \\ &+ uG_0 \int_{q',q''} (\phi_0(q') + G_0(q')B) \\ &\qquad \times (\phi_0(q'') + G_0(q'')B) \\ &\qquad \times (\phi_0(q-q'-q'') + G_0(q-q'-q'')B) \\ &+ \mathcal{O}(u^2),\end{aligned} \tag{2.13}$$

where the subindex in the integral is the variables in which the terms in the parenthesis are evaluated, and the time frequency argument has been removed from the integrand to lighten the notation, but it must be included in the computation.

To calculate G we just need to calculate $\partial\langle\phi\rangle/\partial B|_{B=0}$. This is now trivial since the left hand side only depends on ϕ_0, and this is a Gaussian noise. Averaging the previous equation gives

$$\langle\phi\rangle = G_0 B + 3uG_0^2 B \int_{q'} C_0(q'), \tag{2.14}$$

where $C_0(q,\omega)(2\pi)^{d+1}\delta(q+q')\delta(\omega+\omega') = \langle\phi_0(q,\omega)\phi_0(q',\omega')\rangle$, and so

$$G(q,\omega) = G_0(q,\omega) - 3uG_0(q,\omega)^2 \int_{q'} C_0(q',\omega') + \mathcal{O}(u^2). \tag{2.15}$$

This iteration has a natural Feynman expansion structure in terms of Feynman diagrams. This can be done by rewriting equation 2.7 in terms of these diagrams. The example of Model B is quite straightforward. We describe the propagator as a directed line. The zeroth order fields are just lines, while complete fields ϕ are thicker lines. Each convolution, or interaction, as usual, will be described by a vertex with in incoming line representing the propagator and as many outgoing lines as fields there are in the convolution. Lastly, two averaged zeroth order fields are represented by two incoming lines with a circle between them. These are all in figure 2.1 for model B.

Using this notation, equation 2.14 can be written in the following form:

$\langle\phi\rangle =$ 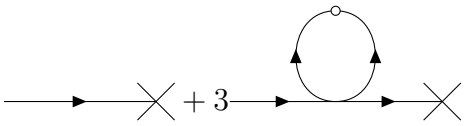 $+ \mathcal{O}(u^2).$ (2.16)

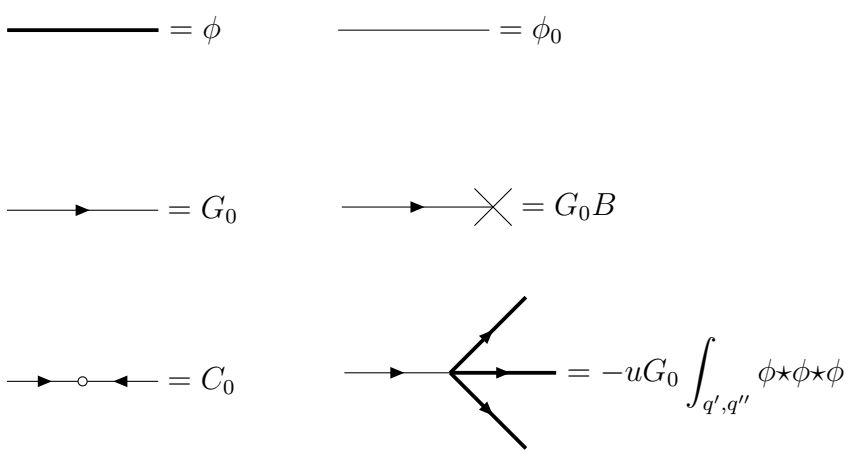

Figure 2.1: Feynman diagram definitions in the formalism of the iterated equation of motion.

Notice that this last equation, before averaging, just lets formally solve the equation of motion in an iterative way, as a series in u. This of course allows us already to approximate any correlation function by just multiplying expansions of the field ϕ together and collecting terms. For example, the two point correlation function up to order u would be calculated as follows:

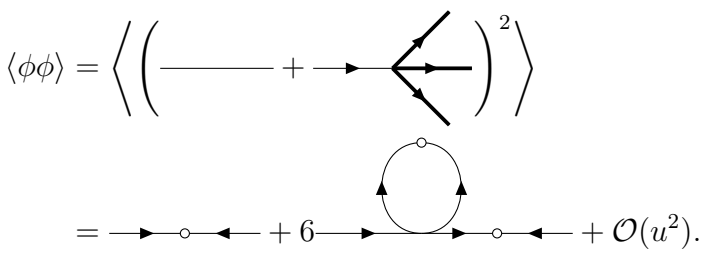

(2.17)

Equations 2.16 and 2.17 show a nice check of the fluctuation dissipation theorem. This theorem reads as follows for an equilibrium system

$$\omega C(q,\omega) = 2D \operatorname{Im} G(q,\omega). \tag{2.18}$$

Since this must be true for Model B for all values of u, then it must also be true at any separate order in the expansion in u. To first order in u, this

is equations 2.16 and 2.17. It is a simple exercise to show that the imaginary part of the first order correction to G is

$6D\,\mathrm{Im}$ 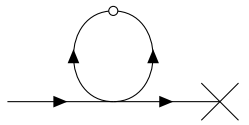 $=$

$$\frac{-12D\omega q^6(a+\kappa q^2)}{[\omega^2+q^4(a+\kappa q^2)^2]^2}\int_{k,\Omega} C_0(k,\Omega). \tag{2.19}$$

The first order correction to C, when symmetrized on the external frequency q, is

6ω 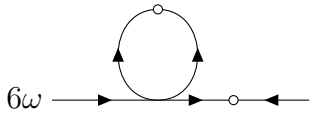 $=$

$$-3u\omega\left(G_0(q,\omega)+G_0(-q,-\omega)\right)C_0(q,\omega)\int_{k,\Omega} C_0(k,\Omega) = \tag{2.20}$$

$$\frac{-12D\omega q^6(a+\kappa q^2)}{[\omega^2+q^4(a+\kappa q^2)^2]^2}\int_{k,\Omega} C_0(k,\Omega).$$

Both corrections to order u are equal as expected, satisfying the fluctuation dissipation theorem. This method becomes more inconvenient to use for correlation functions of many fields since it still depends on a rather uncomfortable sorting of terms after explicitly calculating the product of the field expansions. For this purpose it is more useful to use the standard formalism, used in quantum field theory, that calculates correlation functions from the action 1.12, as done, for example, in [25]. This is what we will do in Chapter 5 in addressing the entropy production, which is written as a composite operator of four fields.

In the rest of the cases of Chapters 3 and 4, though, we will use the iterative approach, since it is slightly more intuitive and easy to apply to 1 loop order.

2.2 PERTURBATIVE RENORMALIZATION GROUP

As explained at the beginning of this chapter, the renormalization group procedure, as will be applied here, consists of formally solving the equation of motion for a shell of high momenta in Fourier space, and then rescaling back the equation of motion for the low momenta to recover the original dynamics.

This involves first splitting the field ϕ into two fields, $\phi = \phi^> + \phi^<$, that are the high and low modes fields respectively with respect to a cutoff Λ and a scaling factor $b > 1$, such that

$$\begin{aligned}\phi^>(q,\omega) &= \begin{cases}\phi(q,\omega) & \text{if } |q| \in (\Lambda/b, \Lambda)\\ 0 & \text{otherwise}\end{cases}\\ \phi^<(q,\omega) &= \begin{cases}\phi(q,\omega) & \text{if } |q| \in (0, \Lambda/b)\\ 0 & \text{otherwise}\end{cases}\end{aligned} \tag{2.21}$$

The way in which the high momenta equation is solved will be perturbatively in the nonlinearities, in a loop expansion.

The process is as follows, illustrated with Model B. In practice the first step is to identify the relevance of all nonlinearities of the system. In this case we only have one, u, and trivial dimensional analysis shows that it is irrelevant above 4 dimensions and relevant below 4 dimensions, so our calculation will be done around 4 dimensions.

Starting from the equation of motion for high modes:

$$\phi^> = \phi_0^> - uG_0 \int_{q',q''} (\phi^> + \phi^<)^{\star 3}, \tag{2.22}$$

where ^{*3} indicates the convolution of the parenthesis cubed (as it comes from the Fourier transform of ϕ^3). The first step is then to iteratively solve the equation to the desired order in the high modes.

Then we take averages over the high modes, this is effectively integrating them out of the equation of motion, and will form the loops of the loop expansion. Because of the δ correlations of $\langle \phi_0 \phi_0 \rangle$, when averaging, only averages of high modes with high modes will produce non-zero results. In the case of Model B, to one loop, we only get two diagrams that contribute to the existing terms, shown in figure 2.2. All other one loop diagrams correspond to higher order nonlinearities that are irrelevant at 4 dimensions. For instance, the diagram in Figure 2.3 could be obtained from a one loop contribution after iterating two of the fields, however, this contributes a term proportional to 6 fields, and a term like ϕ^6 would be irrelevant over 3 dimensions, and so can be ignored. Terms with more fields would also be irrelevant, and so can be ignored as well.

Of the remaining diagrams, the integrand have to be expanded in the external wavenumbers and frequencies, and different configurations of the external wavevectors will give contributions to different terms in the equation of motion. Since we would like to keep the same dynamical structure of the equation of motion, the term $\dot{\phi}$ is always required to be constant under the flow. This means that we can evaluate loop integrals at $\omega = 0$, since

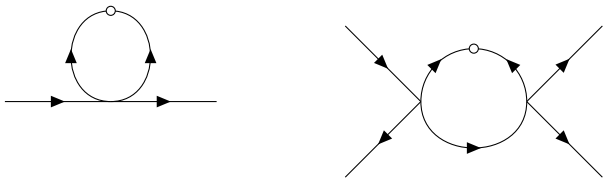

Figure 2.2: One loop diagrams of Model B. The first represents a contribution to the mass term a, and the second a contribution to the coupling u.

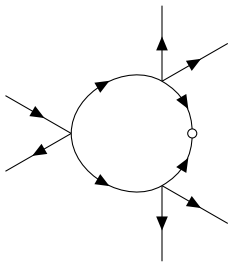

Figure 2.3: Example of a one loop diagram that generates an irrelevant (in the RG sense) coupling.

allowing for higher order terms would mean having terms with multiple time derivatives or time derivatives of gradients that are irrelevant.

The first of the two diagrams in Figure 2.2 is a term proportional to $\phi^<$, while the second is proportional to $(\phi^<)^3$. The first diagram represents the integral

$$-3u \int_{q',\omega'} C_0(q',\omega'), \tag{2.23}$$

where the 3 in front is the symmetry factor, since we are averaging two zeroth order field out of three terms and there are three ways to do so. The second term represents the integral

$$18u^2 \int_{q',\omega'} G_0(q'-q,\omega'-\omega) C_0(q',\omega'). \tag{2.24}$$

After substituting this in the equation of motion for $\phi^<$, we get the original equation, only now with the fields being $\phi^<$, and the couplings a and u modified by absorbing both one loop diagrams:

$$-i\omega q^{-2}\phi^< = -a_I\phi^< - \kappa q^2\phi^< + q^{-2}\eta - u_I \int_{q',q''} \phi^< \star \phi^< \star \phi^<, \tag{2.25}$$

where the intermediate values are

$$\begin{aligned} a_I &= a + 3\kappa\bar{u}\Omega_d \int_{\Lambda/b}^{\Lambda} q^{d-3} dq - 3\kappa\bar{a}\bar{u} \int_{\Lambda/b}^{\Lambda} q^{d-5} dq, \\ u_I &= u\left(1 - 9\bar{u}\Omega_d \int_{\Lambda/b}^{\Lambda} q^{d-5} dq\right), \end{aligned} \tag{2.26}$$

where we have introduced the reduced couplings $\bar{a} = a/\kappa, \bar{u} = uD/\kappa^2$, and $\Omega_d = S_d(2\pi)^{-d}$, with S_d being the surface area of a d dimensional sphere $S_d = 2\pi^{d/2}/\Gamma(d/2)$. In the first integral we have expanded C_0 to first order in a.

The integrals are done using what is known as dimensional regularization, a method by which Feynman loop integrals can be calculated as a function of a continuous parameter d (thus the factor Ω_d). This is the standard method by which poles are extracted from these integrals or, in this case, by which we can write them for any value of d in a general way. This is further explained in Appendix A where some formulae are given for different integrals.

Notice that the angular part of the loop integrals is trivial here since there is no mixing between wavevector of different field (i.e. there are no gradients of different fields contracted). In the following chapters this will not be the case and these angular integrals can get more complicated, so there is an explanation of how to do them in general in Appendix A.

The last step is to rescale all momenta back to their original scale $q \to bq$. This will introduce scales for both the field ϕ and time t. Since we at first do not know these scalings, we leave them in terms of unknown exponents z and χ, such that $\omega \to b^z\omega$ and $\phi \to b^{-\chi}\phi$. The rescaling allows to define rescaled parameters $g_i = b^{\gamma_i} g_{i,I}$, where each g_i is just each of the original parameters. In order to get a continuous flow we just have to take the shell of high momenta that we integrate out to be infinitesimally thin, that is, send $b \to 1 + db$. We then get

$$\begin{aligned} \frac{da}{db} &= a(z-2) + 3\kappa\bar{u}\Omega_d\Lambda^{d-2} - 3\kappa\bar{a}\bar{u}\Omega_d\Lambda^{d-4}, \\ \frac{dD}{db} &= D(z-2-d-2\chi), \\ \frac{d\kappa}{db} &= \kappa(z-4), \\ \frac{du}{db} &= u(z-2+2\chi - 9\bar{u}\Omega_d\Lambda^{d-4}). \end{aligned} \tag{2.27}$$

Notice we have not calculated intermediate values for κ or D. The reason there is not one for κ is because the first diagram of Figure 2.2 is the

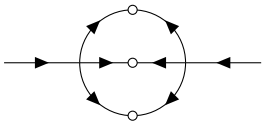

Figure 2.4: Two loop diagram that generates the correction to the scaling of the noise.

only diagram to one loop that might contribute to κ, however it cannot do so because the external frequency does not run through the loop, so it cannot generate a term proportional to q^2. The case for D is the same, there is no one loop contribution to the noise strength, and the first nonvanishing one would come from a two loop diagram as in Figure 2.4. However, this is generally zero for mass conserving systems, as will be discussed in Chapter 3 [25].

Equation 2.27 is the full flow of the system, and there is some freedom in choosing the exponents. Different choices give different fixed points which give information about different scale invariant configurations of the system.

If we choose a to be fixed, then $z = 2$ and the only flow of the system is κ, $d\kappa/db = -2\kappa$, so that κ goes to 0 in the fixed point. This is the infinite temperature fixed point, as $\kappa = 0$ means there are no correlations in the system.

If we choose κ to be fixed, then $z = 4$, and the only flow is the one of a, $da/db = 2a$. The parameter a diverges and the fixed point we find for the system is $a = 0$. Since the flow takes the parameter away from this value, this fixed point describes a transition with nontrivial scale invariance (this transition is of course the phase transition found with MFT when $a = 0$). This is then the choice that allows us to study the critical point of the system.

For Model B, it is a bit simpler to work with the results by writing the flow for the reduced parameters $\bar{a} = a/\kappa$ and $\bar{u}$, defined above, which are the parameters that result from measuring the system in units in which $\kappa = D = 1$. This is perfectly reasonable to do since we are going to require that the flow leaves these two parameters unchanged. Doing so, we obtain

$$\begin{aligned} \frac{d\bar{a}}{db} &= 2\bar{a} + 3\bar{u}\Omega_d\Lambda^{d-2} - 3\bar{a}\bar{u}\Omega_d\Lambda^{d-4} \\ \frac{d\bar{u}}{db} &= \bar{u}\left(\epsilon - 9\bar{u}\Omega_d\Lambda^{d-4}\right). \end{aligned} \tag{2.28}$$

This is the RG flow to one loop of the equilibrium ϕ^4 theory, and is depicted in Figure 2.5. We have introduced $\epsilon = 4 - d$, the small parameter

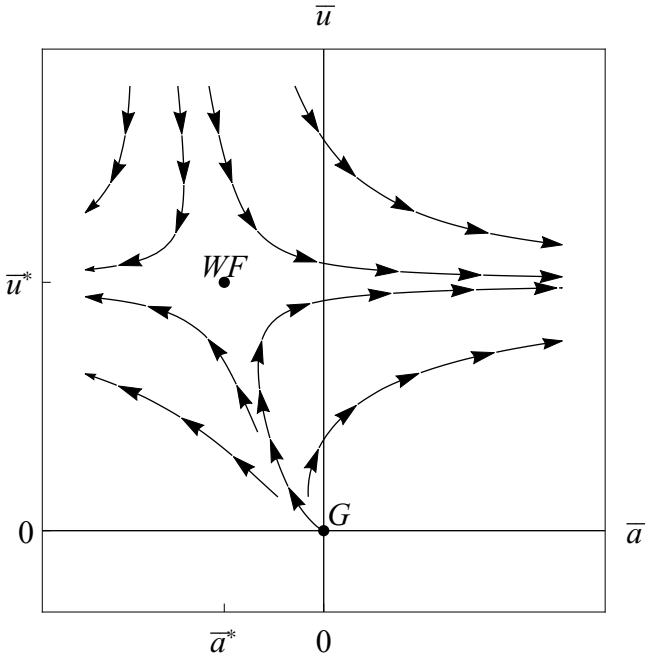

Figure 2.5: Flow of the ϕ^4 theory parameters below 4 dimensions showing the Gaussian and Wilson-Fisher fixed points.

of our expansion for the fixed points, since each loop order gives higher powers of ϵ.

This flow has different solutions depending on the dimension. Above 4 dimensions, the only fixed point is $\bar{a} = \bar{u} = 0$, so $\bar{u}$ flows to 0, and so the system flows back to the Gaussian model and will have Gaussian behaviour. Below 4 dimensions, there is a new fixed point $\bar{u}^* = \epsilon\Lambda^{4-d}/(9\Omega_d)$, and $\bar{a}^* = -\epsilon\Lambda^2/6$, which is the Wilson-Fisher fixed point. The particular values of the parameters at the fixed point is not universal since it depends on the particular definition of the parameters and on the cutoff. Only universal results will be of interest.

The point ruling the phase transition can be found by linearising the flow around each fixed point. The flow is repulsive in the $\bar{a}$ direction in both fixed points. On the other hand, the Gaussian fixed point is repulsive in the second eigenvector of the linearised flow, while the Wilson Fisher point is attractive. This means that $\bar{u}$ flows to the value of the WF point, while $\bar{a}$ diverges, so that, below 4 dimensions, the WF point rules the behaviour of the phase transition.

Linearising the flow around the WF fixed point gives us information about the critical exponents. First, fixing the flow for κ and D already gives $z = 4$ and $\chi = (2 - d)/2$. Notice these are already the Gaussian values at

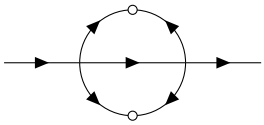

Figure 2.6: Two loop diagram that generates the first correction to the scaling of the field, χ.

$d = 4$, and the reason is that D was not renormalized, and that χ obtains its first correction at order ϵ^2. This correction would come at two loops from the diagram of Figure 2.6 [25].

We find, however, a correction to the exponent ν, by linearising the flow of $\bar{a}$, since the dimension of $\bar{a}$ is the inverse of the dimension of the correlation length. This linearisation gives

$$\nu = \frac{1}{2} + \frac{\epsilon}{12} + \mathcal{O}(\epsilon^2). \tag{2.29}$$

This allows us to calculate the one loop correction to the exponent α of the specific heat through the scaling relation $\alpha = 2 - d\nu = \epsilon/6 + \mathcal{O}(\epsilon^2)$. In Chapter 5 we will see a different method of calculating this anomalous dimensions and apply it to the study of the entropy production.

2.3 RENORMALIZATION OF COMPOSITE OPERATORS

One last tool that will be used in Chapter 5 is the renormalization of arbitrary composite operators. A composite operator $\mathcal{O}$ is defined as any function of the field ϕ with at least two fields, in which all fields are evaluated at the same point. Calculating the scaling of this kind of operators is what was done in the last sections for the operators ϕ^2, $(\nabla\phi)^2$, and ϕ^4 that were part of the free energy. However, if we want to find the scaling of an arbitrary operator that is not part of the dynamics of the system, we cannot follow the iterative procedure used so far. We have to turn to the use of dynamical actions, in particular the Martin-Siggia-Rose (MSR) action, that allows to formulate the statistics of dynamic paths in a way that is analogous to the Boltzmann description of state probabilities in equilibrium systems.

There are two main dynamical actions, the Onsager-Machlup, and the MSR action. Consider a dynamical equation of the type we have been using so far, of the form

$$\dot{\phi} = F[\phi] + \eta, \tag{2.30}$$

where ϕ is a scalar field, $F[\phi]$ is an arbitrary functional of ϕ, and η is a noise with the following correlations

$$\langle \eta(r,t)\eta(r',t')\rangle = 2L\delta^{(d)}(r-r')\delta(t-t'). \tag{2.31}$$

The correlations of the noise allow for an arbitrary operator L to define the noise strength. For instance, mass conserving systems will have $L = -D\nabla^2$, while for systems that do not conserve mass, $L = D$.

For this equation of motion, an action can be built by just requiring that the probability distribution produces the noise correlations, i.e. we must have that $\mathcal{W}[\eta] \propto \exp(-\int \eta L^{-1}\eta)/4$. By using the equation of motion, we obtain the Onsager-Machlup functional

$$G[\phi] = \frac{1}{4}\int d^d x dt \left(\dot{\phi} - F[\phi]\right) L^{-1} \left(\dot{\phi} - F[\phi]\right). \tag{2.32}$$

This is already enough to have a path integral framework for the equation of motion. Averages of fields can be obtained by adding a term of the form $h\phi$ to the integrand of the action, where h is an external field, and then applying functional integrals with respect to this field on the path integral, as follows

$$\langle \phi(x,\tau)\rangle = C\frac{\delta}{\delta h(x,\tau)}\int D[\phi] e^{-\frac{1}{4}\int d^d r dt G[\phi] - 4h(x,t)\phi(x,t)}\Big|_{h\to 0}, \tag{2.33}$$

where C is a normalization constant, and the $D[\phi]$ indicates the path integral on paths of ϕ.

The Onsager-Machlup functional is slightly inconvenient to use for a couple of reasons. Firstly, for mass conserving systems, L^{-1} will show a divergence at large distances. Secondly, having the square of the equation of motion means having nonlinearities of a very high order.

For this reason, a more usable action, the MSR, can be built from this one. The way to do it is including an auxiliary field $\tilde{\phi}$ through a rather complicated unity [25], to obtain

$$\mathcal{A}[\phi,\tilde{\phi}] = \int d^d r dt \tilde{\phi}\left(\dot{\phi} - F[\phi]\right) - \tilde{\phi} L \tilde{\phi}. \tag{2.34}$$

The order of the nonlinearities is now of the same order as in the free energy, and the operator L appears as a factor, so there is no divergence at large distances. The field $\tilde{\phi}$ is called the response field because the propagator G can be found through the correlations between ϕ and $\tilde{\phi}$. In Fourier space, this is [25]

$$(2\pi)^{d+1}\delta^{(d)}(q+q')\delta(\omega+\omega')G(q,\omega) = \langle \phi(q,\omega)\tilde{\phi}(q',\omega')\rangle. \tag{2.35}$$

This comes from the fact that a coupling to a linear field h in the free energy would be a term of the form $\dot{\phi} = \ldots + h$ in the equation of motion, which would make the MSR action to take the following form

$$\mathcal{A}[\phi, \tilde{\phi}] = \int d^d r dt \tilde{\phi} \left(\dot{\phi} - F[\phi] \right) - \tilde{\phi} L(\tilde{\phi} + h). \tag{2.36}$$

The MSR action now allows for an RG analysis that follows the exact same lines as how it would be done on a free energy in the standard literature of equilibrium statistical mechanics [30, 31, 25]. The Feynman rules are the same explained in the previous section, and in Figure 2.1, except an incoming line must be understood as a response field $\tilde{\phi}$. Notice that when building diagrams, the iteration step by which we introduced a propagator G_0 in the loop is now the step in which a ϕ_0 is correlated with a $\tilde{\phi}_0$, which give the same propagator G_0.

We are then in a position to calculate the average of an arbitrary operator $\mathcal{O}$, by adding it to the MSR action coupled to its auxiliary field a, $\mathcal{A} \to \mathcal{A} + \int a\mathcal{O}$. Doing so, we can write

$$\langle \mathcal{O}(x, \tau) \rangle = C \frac{\delta}{\delta a(x, \tau)} \int D[\phi, \tilde{\phi}] e^{-\int d^d r dt \mathcal{A} + a\mathcal{O}} \Big|_{a \to 0}, \tag{2.37}$$

where C is a normalization constant. The scaling of the operator $\mathcal{O}$ can then be calculated as the RG flow of its auxiliary field a, in a completely analogous way to how the scaling of the terms in $\mathcal{A}$ is calculated [30]. For this we only need to introduce one new Feynman rule, by which an insertion of an operator $\mathcal{O}$ of order n (with n fields) is denoted by a wiggly line with n outcoming fields.

We can easily exemplify the calculation of an anomalous scaling of an operator with the simplest example, which is inserting a mass term $m\phi^2$ into Model B, for which the RG flow was already calculated in the last section. Notice that this term allows to calculate averages and correlations of ϕ^2 terms, which is the mass term of the free energy. Its anomalous scaling must therefore be the same as the one of the a term of the equation of motion, that appears in the MSR action as $a\tilde{\phi}\phi$. This mass term has the Feynman vertex function on the left of Figure 2.7.

The anomalous dimension of m close to the Wilson-Fisher can be calculated to one loop by considering the one loop diagram correction to the vertex on the left of Figure 2.7, which is the one diagram on the right of the Figure, where the propagator comes from the average of one of the two fields of the insertion with the $\tilde{\phi}$ field of the u vertex, while the correlator comes from the average of two ϕ fields.

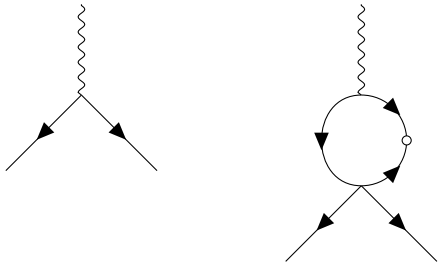

Figure 2.7: Feynman vertex diagram for a mass insertion (left), and one loop correction to it of order ϵ (right).

This loop diagram is quite simple to calculate, it just represents the intermediate value of m

$$m \to m\left(1 - 6u\int_q C_0(q)G_0(-q)\right) = m\left(1 - 3\bar{u}\Omega_d\Lambda^{d-4}\right). \quad (2.38)$$

In the previous section we found the fixed point of $\bar{u}$ in Model B to be $\bar{u}^* = \epsilon/(9\Omega_d\Lambda^{d-4})$, so the above equation reduces to $m \to m(1-\epsilon/3)$.

We thus identify this is the anomalous dimension to a mass term, usually denoted as $\gamma_{\phi^2} = -\epsilon/3$, and can use the fact that a (the prefactor of $\tilde{\phi}\nabla^2\phi$)) is the reduced temperature parameter to find the exponent ν of the correlation length ξ, $\xi \sim a^{-\nu}$. The natural dimension of a is 2, so this anomalous dimension means that $a' = b^{2-\epsilon/3}a$, so $a \sim \xi^{2-\epsilon/3}$. Inverting this relation we obtain

$$\nu = \frac{1}{2} + \frac{\epsilon}{12} + \mathcal{O}(\epsilon^2), \quad (2.39)$$

which is the usual one loop correction to ν, calculated here through the insertion of an extra mass term m. This can be combined with the hyperscaling relation to obtain the one loop value of the critical exponent α of the divergence of the specific heat $\alpha = 2 - d\nu$, obtained from the scaling of the free energy density $f \to b^d f$, and the definition of the specific heat at constant volume $c_V = -d^2 f/da^2$, giving

$$\alpha = \frac{\epsilon}{6} + \mathcal{O}(\epsilon^2). \quad (2.40)$$

Notice that the same result could be obtained from the flow of $\bar{a}$ in equation 2.28, by expanding the value of the of integral of the first diagram of Figure 2.2 to linear order in a, since that diagram and the one on the right of Figure 2.7 represent the same kind of correction.

This technique will be used in Chapter 5, albeit with more complicated insertions, which deserve a further introduction here. Considering systems only close to the Wilson-Fisher fixed point (since scalings around the Gaussian fixed point are trivial), the naive dimension of an operator with n gradients and m fields in 4 dimensions is just $m + n$. This means most high order operators we can consider (and certainly the ones studied in Chapter 5) are irrelevant in the RG sense if $m + n > 4$.

Since the u vertex is dimensionless in 4 dimensions, one loop ϵ corrections to a given insertion will come from other operators that have the same dimension as the insertion itself in 4 dimensions [30]. Assume for example we wan to study operators of dimension $m + n = 6$. We can build seven independent operators that satisfy this

$$\begin{aligned}
\mathcal{O}_1 &= \phi^6, \\
\mathcal{O}_2 &= \phi^3 \nabla^2 \phi, \\
\mathcal{O}_3 &= \phi^2 (\nabla \phi)^2, \\
\mathcal{O}_4 &= \phi \nabla^4 \phi, \\
\mathcal{O}_5 &= \nabla \phi \cdot (\nabla \nabla^2 \phi), \\
\mathcal{O}_6 &= (\nabla^2 \phi)^2, \\
\mathcal{O}_7 &= (\nabla_\alpha \nabla_\beta \phi)^2.
\end{aligned} \tag{2.41}$$

Notice that the first has $m = 6, n = 0$, the next two have $m = 4, n = 2$ and the last four have $m = 2, n = 4$. This is the example that can be found in [30], in addressing the question of whether or not these irrelevant operators might become relevant for large enough ϵ. The technical aspects of the calculation can be found in that reference, and since Chapter 5 applies this technique to a more complicated case, the example will not be reproduced here, only the outline of how to get the results.

In principle, all these seven operators have to be added to the action with new auxiliary fields $\mathcal{A} \to \mathcal{A} + \int \sum_a a_i \mathcal{O}_i$, and their loop corrections calculated. All seven operators will contribute to each other, producing a coupled flow between all seven auxiliary fields when taken as the flowing parameters. To one loop, though, and if we restrict the calculation to only order ϵ, the seven operators can be separated into three groups with the three different values of m, and operators in one group will not contribute to others. This is because if we only allow for one loop and one u vertex, a given insertion will produce a one loop term with the same number of legs.

Moreover, if an insertion has m legs, to one loop, terms with fewer legs cannot be produced. This means that if we only insert one group of these operators, this group will not receive contributions from terms with higher

values of m, and they will not generate terms with lower values of m, so each group can be studied separately. This is what can be seen in [30] when dealing with these operators to one loop, where the corrections of order ϵ make the matrix M_{ij} quite simple. This simplification is true only to one loop and order ϵ, since mixed contributions will appear at higher orders. Nonetheless, this simplification will be very useful in Chapter 5.

In the spirit of RG as we have applied it here, these one loop contributions are reabsorbed by the action as intermediate values to each a_i. The flow of these a_i's can now be conveniently written in terms of a matrix of contributions M_{ij}, such that

$$\frac{da_i}{db} = \tilde{d}a_i + M_{ij}a_j, \tag{2.42}$$

where $\tilde{d}$ is the natural dimension of a_i. The matrix M_{ij}, to one loop, will be then proportional to ϵ.

This flow can be rewritten in terms of the left eigenvector of M_{ij}. This matrix is calculated considering each a_i as the unitary basis of the space of these parameters, we can then write these eigenvectors as follows

$$v^\alpha = \sum v_i^\alpha a_i, \tag{2.43}$$

where α just indexes different eigenvectors. They must satisfy

$$v_i^\alpha M_{ij} = \delta^\alpha v_j^\alpha, \tag{2.44}$$

where δ^α is the corresponding eigenvalue. It is then a simple exercise of linear algebra to find the flow of v^α

$$\frac{dv^\alpha}{db} = \tilde{d}v_i^\alpha a_i + v_i^\alpha M_{ij}a_j = \left(\tilde{d} + \delta^\alpha\right) v^\alpha. \tag{2.45}$$

It is in terms of these eigenvectors that we will talk about the scaling of an arbitrary operator. The anomalous scaling of a given $\mathcal{O}$ will then be calculated by decomposing its response field into the v^α basis, and its leading scaling will be the largest δ^α of the eigenvectors in which it has a nonzero projection. In the particular case of operators of dimension 6 in 4 dimensions, the matrix M_{ij} has a very simple structure, making results simple at one loop, but this will not be the case in the operators in Chapter 5, and we will have to make use of these decompositions.

One last detail to remember here is that the scalings of a given operator $\mathcal{O}$ and its auxiliary field a_i are related by the fact that the action $\mathcal{A}$ must be dimensionless, they are thus the negative of each other plus the term

coming from the differentials $d^d r dt$. The leading scaling is the one of the largest eigenvalue, which makes the flow of v^α more divergent. If $v^\alpha \sim b^{\tilde{d}+\delta^\alpha}$, then the average of $\mathcal{O}$ will behave

$$\langle \mathcal{O} \rangle \sim b^{-d_\mathcal{O}-\delta^\alpha} \sim \xi^{d_\mathcal{O}+\delta^\alpha}, \tag{2.46}$$

where $d_\mathcal{O}$ is the natural dimension of $\mathcal{O}$. It can be seen here that a higher δ^α produces a faster divergence (or slower convergence to 0 in the case of an irrelevant operator, which will usually be the case) as the correlation length diverges, and so it will dictate the behaviour of $\mathcal{O}$.

3

CONSERVED KPZ+

Before jumping into the main analysis of Active Model B+, this chapter will study a simpler model[1]. The reason is two-fold. First, this model has a lot of physical interest in itself, since it has not been studied before and changes certain aspects that were previously believed about the behaviour of conserved surface growth. The second reason is that it shares a lot of mathematical structure and results with AMB+, and so will serve as a mathematically simpler introduction to what will be described in the next chapter.

The model we study is the conserved KPZ+ model (cKPZ+), briefly described in the introduction. As was mentioned there, cKPZ+ can be mathematically obtained from AMB+ by simply setting $a = u = 0$, obtaining the equation of motion

$$\dot{\phi} = -\kappa\nabla^4\phi + \lambda\nabla^2(\nabla\phi)^2 + \zeta\nabla\cdot[\nabla^2\phi\nabla\phi] + \eta, \tag{3.1}$$

where, as before, η represents a conserved Gaussian white noise, with the variance

$$\langle\eta(r,t)\eta(r',t')\rangle = 2D(i\nabla)^2\delta^{(d)}(r-r')\delta(t-t'). \tag{3.2}$$

As mentioned in the introduction, the description of ϕ as a concentration field defined in a bounded interval disappears, since the polynomial part of the free energy is what kept that bound.

The model has now, however, a different symmetry not present before, symmetry under a global shift, $\phi \to \phi + h$, for a constant h. These models are usually used to describe interface or surface dynamics if we now interpret ϕ as a height variable instead of concentration. The simplest example of this kind of model would be plain noisy diffusion, or what is known as the Edwards-Wilkinson (EW) equation [33]:

$$\dot{\phi} = \nabla^2\phi + \xi, \tag{3.3}$$

where ξ is a white Gaussian noise with strength D. Notice that if the noise is not conserved, then the average height of the system is not conserved at each instant, even though the noiseless dynamics is a continuity equation.

1 The model and results of this chapter are reported in reference [32]. This chapter serves as an expansion of that paper.

The average ensemble of the height at long timescales, though, is indeed conserved, since the noise is Gaussian, and what we have is a simple interplay between diffusion, that tends to smooth out the surface, and noise, that tends to roughen it.

Notice that EW is an equilibrium system, since it comes from a simple free energy with only a square gradient term $\mathcal{F} = \int (\nabla\phi)^2$.

The most famous nonequilibrium version of this is the Kardar-Parisi-Zhang (KPZ) equation [34], that expands the dynamics of equation 3.3 to include nonlinear terms as a gradient expansion of the total area S, which can be written as $S = \int \sqrt{1 + (\nabla\phi)^2}$, to get, to first order:

$$\dot{\phi} = \nabla^2\phi + \lambda(\nabla\phi)^2 + \xi. \tag{3.4}$$

Notice that now the deterministic part of the equation is no longer a continuity equation, and so the surface now grows. Unlike the equation analysed in this Chapter, the KPZ equation has a Galilean invariance that has deep consequences for its behaviour and the exact calculation of its critical exponents [33].

This equation has proven to be extremely useful and universal, and many different physical processes that can be described as evolving surfaces seem to fall in the universality class of this equation, making it a very important model in nonequilibrium statistical physics. In particular, many processes in which a surface or interface evolve due to nonconserved fluctuations are described at large scales by the KPZ equation, examples being the Eden model for cell colonies growth, or ballistic deposition models [33, 35, 36].

The surprising generality of this model, together with some also surprising mathematical properties regarding its RG behaviour that will be discussed below, have motivated a lot of theoretical and experimental work regarding this model. However, there are still some physics regarding surface growth that are not captured by the KPZ equation, and other universality classes have been found, typically depending on mass conservation or the nature of the source of the noise [25]. Another main class of processes are those in which the dynamics at the surface are dictated by surface diffusion, and new matter is added to it by means of random deposition. Examples are vapour deposition or molecular beam epitaxy [37], and the fact their deterministic dynamics cannot create new matter means that the noiseless equation of motion of their continuum description must be a continuity equation $\dot{\phi} = -\nabla \cdot J$, for a current J. This gives rise to models that do not belong to the KPZ universality class.

A different case, proposed first to study non-KPZ universality classes and the role of surface diffusion on surface growth, is the case of a determin-

istic equation that conserves mass together with a conserved noise. These are believed to be possibly modelled by particles that jump in the surface (thus conserving total mass) with no correlation (at least to leading order) between the direction of movement and the local slope, and have a physical interpretation proposed by Villain [33]. This allows to cancel the diffusion of the height itself, while keeping the diffusion of matter within the surface. This, together with the fact that our equation has to be now a continuity equation, means we can write an equation of motion for this model as

$$\dot{\phi} = -\nabla \cdot J + \eta, \tag{3.5}$$

where η is now a conserved noise.

A particular example that was initially proposed in [38], has the following current:

$$J = \kappa \nabla \nabla^2 \phi - \lambda \nabla (\nabla \phi)^2. \tag{3.6}$$

As mentioned above, the deterministic part of this equation of motion generates two universality classes, one that we describe below in some detail, coming from the previous equation, and a second one obtained by studying the same deterministic current but with a nonconserved noise, known as the Wolf-Villain model [39]. Following the first publication of these models, extensive analytical and numerical work has been done to study them, and the RG procedure has proved to be a very good tool at determining the scaling of these systems, at least below 2 dimensions [40, 41, 42, 43].

Notice that taking the chemical potential, μ, to be such that $J = -\nabla \mu$, this chemical potential is the same as the one for the KPZ equation upon writing it as $\dot{\phi} = -\mu + \xi$. Only now there is an extra Laplacian, transforming the equation into a continuity equation, and the noise has become conserved. Thus, equations 3.5 and 3.6 were originally called conserved KPZ (cKPZ). Notice that cKPZ results from equation 1.16, setting $\zeta = 0$.

This is why we identify our equation of motion 3.1, as a surface growth model, and we call it conserved KPZ+ (cKPZ+). The equation of motion is rewritten here for convenience

$$\dot{\phi} = -\kappa \nabla^4 \phi + \lambda \nabla^2 (\nabla \phi)^2 + \zeta \nabla \cdot [\nabla^2 \phi \nabla \phi] + \eta. \tag{3.7}$$

The only difference with cKPZ is the ζ term. If the cKPZ+ equation of motion is understood as an expansion in fields and gradients, then the ζ term should be added for consistency, since, as the λ term, it is made of four gradients and two fields. This term has been previously ignored in the literature [33], that considered gradient expansions of conserved surface growth

dynamics to be expansions of the current in single gradients of a field, thus producing a current of the following form, as reported in [33],

$$J = -\left[\sum_i \nu_i (\nabla\phi)^{2i}\right] \nabla\phi. \tag{3.8}$$

This kind of expansion is self consistent in the RG sense, as nonlinear current terms with Laplacians of the field cannot be produced if they are not present at first in the theory, so the critical properties of theories of conserved surface growth are not missing any results for not considering this new ζ term.

However, we next prove that this term should indeed be present in coarse grained, continuous versions of the microscopic theories that are usually used to define these models. These microscopic theories are, as described above, theories in which particles jump with no correlation between their direction and the local slope of the surface [33]. A possible microscopic model for this would be one in which a random particle is chosen at the surface and made to jump a fixed distance in a random direction (independently of the slope in that direction), again, in line with examples described in [33]. These microscopic dynamics are related to the restricted solid on solid rules for conserved surfaces [43, 44], in which particles jump to neighbouring sites irrespectively of the slope as long as the height difference is kept below some threshold, thus avoiding very high gradients. Our claim is that the universality class of these systems in two or more dimensions should be described by our cKPZ+ equation in the continuum limit.

We can therefore show that the ζ term should be present by considering a two-dimensional surface with a global slope in one direction and a corrugated profile in the perpendicular direction, as in figure 3.1, for example, $\phi = by + a\cos(\omega x)$. Consider that a particle jumps a fixed geodesic distance represented by the blue circle, with the particle starting at the middle, with position (x_0, y_0). Now consider the section of the surface cut by the vertical plane $y = y_0$, this is the red line in figure 3.1. The fraction of sites of the possible landing circle with a higher y, $y > y_0$ is, as shown in the figure, greater than $1/2$ in a ridge and less than $1/2$ in a valley. This bias vanishes if either ω or b are equal to 0, however, in the presence of both, it follows from this argument that the deterministic flux in the y direction (plotted for this surface also in figure 3.1) must have a term proportional to $\phi_y\phi_{xx}$, which is exactly the structure of the ζ term, and could not be captured by the λ term.

Notice that, taking the dynamics of the cKPZ+ model as an expansion in fields and gradients, the model is now complete to the order of four gra-

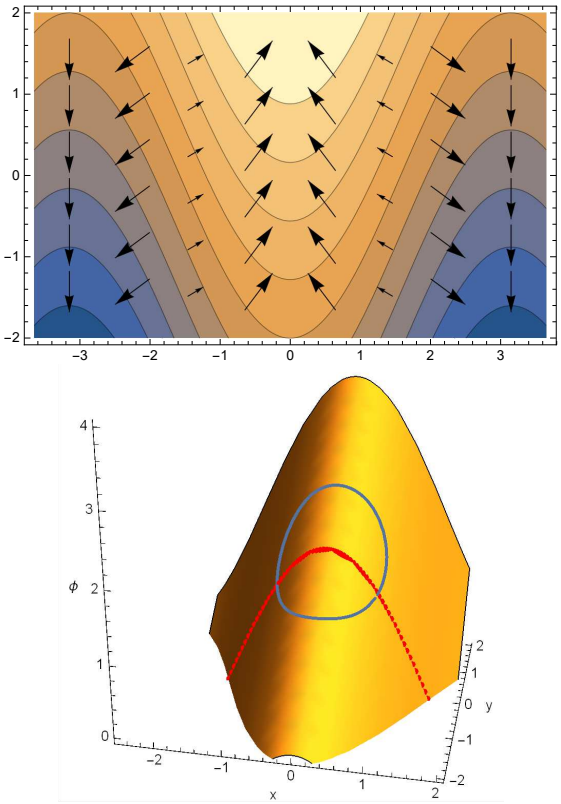

Figure 3.1: On the top deterministic flow due to the ζ term in the cKPZ+ model, showing a shear-like flow due to a combination of slope and curvature. On the bottom, the ridged surface showing the geodesic circle around a particle's initial position and the section of constant y. Adapted from [32].

dients and two fields. To this order, only three independent terms can be written that respect conservation of mass (that can be written as the gradient of a current). Two of them are the λ and ζ terms, and the third term would be a term like $\nabla^2(\phi\nabla^2\phi)$. Notice that this term, however, breaks the symmetry $\phi \mapsto \phi +$ const. and so it cannot be part of a surface growth model.

We will study this model first and show that it has interesting large scale properties that are lost in the case of the cKPZ model. In Chapter 4, the results of cKPZ+ will expand in a more complex form to those for AMB+ making a clear connection between them in terms of their mathematical behaviour at large scales, and making the more complex results of AMB+ easier to understand and interpret, even though they describe different physics from cKPZ+ as interpreted and analysed in this Chapter.

One last point to make about surface growth models is the way we measure their behaviour. The main observable of these systems is their width, defined as

$$W(L,t)^2 = \frac{1}{Ld}\int d^d r[\phi - \langle\phi\rangle]^2, \tag{3.9}$$

defined as a function of time t, for a given system size L.

From the point of view of scaling, remember the field scales with the critical exponent χ, known as roughness exponent in the context of surface growth physics, and that z is associated to time. The roughness exponent χ gives the scaling form of the two-point correlation function, that behaves as follows in the critical point

$$C(x,t) = |x|^{2\chi}\tilde{f}(t/|x|^z), \tag{3.10}$$

for some scaling function $\tilde{f}$. For two different points at the same time and for two different times at the same point in space, the height fluctuations will be

$$\begin{aligned} \langle[\phi(x,t) - \phi(0,t)]^2\rangle &\sim |x|^{2\chi}, \\ \langle[\phi(x,t) - \phi(x,0)]^2\rangle &\sim t^{2\chi/z}. \end{aligned} \tag{3.11}$$

For negative values of χ, the height fluctuations die out with distance and time, and the surface becomes smooth. For χ between 0 and 1, the height fluctuations grow with the distance, and the surface is called rough. The value $\chi = 1$ is usually taken as a signal that one of the main assumptions of these models (that the height is a single-valued functions so that the surface orientation is remains constant) breaks, since the fluctuations stop obeying

$$\lim_{x\to\infty} \langle[\phi(x,t) - \phi(0,t)]^2\rangle/|x| = 0. \tag{3.12}$$

A value of $\chi = 1$ is therefore not taken as a physically meaningful result in the context of surface growth [33, 25]. Lastly, the marginal value $\chi = 0$ typically signals a logarithmic growth of the surface.

The scaling for the height fluctuations described above can be applied to calculate the scaling behaviour of finite size systems [25], so that for a given L,

$$W(L,t) \sim t^{2\chi/z}. \tag{3.13}$$

Notice that if $\chi = 0$, which happens in 2 dimensions, the previous power law becomes a logarithmic law, so that in 2 dimensions we expect the width to grow logarithmically.

The interpretation of the roughness exponent is more intuitive in the context of finite systems, since negative values of χ means decreasing width as a function of the system size, so that as the size is sent to infinity, we obtain a flat surface. A rough surface, with positive χ does the opposite, and surface fluctuations cause the width to increase with the system size.

In finite systems, the width cannot grow infinitely and typically saturates at some value $W(L, \infty)$. The saturation value grows then with the size of the system as

$$W(L, \infty) \sim L^{2\chi}. \tag{3.14}$$

This comes from a standard finite size scaling argument for surface growth models [25, 33].

3.1 RENORMALIZATION GROUP ANALYSIS

We therefore apply the techniques of Chapter 2 to this model. First, it is worth studying the linear model, which will be rather trivial from the RG point of view. The linearised cKPZ+ equation is known as Mullins' equation

$$\dot{\phi} = -\kappa \nabla^4 \phi + \eta, \tag{3.15}$$

where η is a conserved noise with the correlations of equation 1.10. Since it is linear, integrating out high modes is trivial and we can rescale the equation of motion trivially. This rescaling is $\phi \mapsto b^{-\chi}\phi$, $t \mapsto b^{-z}t$ and $x' \mapsto b^{-1}x$. All rescalings can be absorbed by κ and D, obtaining

$$\begin{aligned} \kappa' &= b^{z-4}\kappa \\ D' &= b^{z-d-2-2\chi}D. \end{aligned} \tag{3.16}$$

These rescalings give the Gaussian behaviour of the system straight away by fixing both parameters, which gives the usual exponents $z = 4$ and $\chi = (2-d)/2$. We then expect our results to give corrections to these exponents. The next step is to find the dimensions of the new nonlinearities, which can be done by dimensional analysis, assuming again that κ and D are fixed. Doing so, rescaling the equation of motion with the nonlinearities, we obtain

$$(\lambda', \zeta') = b^{(2-d)/2}(\lambda, \zeta). \tag{3.17}$$

This seemingly gives a critical dimension of $d_c = 2$, such that below 2 dimensions, fluctuations due to the new nonlinearities will dominate the

behaviour of the system, and that above 2 dimensions, the system behaves as its mean field version (we will find that this is only true for small enough starting values of λ and ζ).

The RG technique will thus give us approximations, as a series in $\epsilon = 2 - d$, of the real scalings of the nonlinearities and critical exponents z and χ of the system.

First, we write the equation of motion as such. From now on all expressions are in Fourier space, so, as in Chapter 2, ϕ will represent the field in Fourier space as well. The equation of motion is therefore

$$\phi(q,\omega) = \phi_0(q,\omega) + \frac{G_0(q,\omega)}{2} \int_{q',\omega'} g(q,q')\phi(q',\omega')\phi(q-q',\omega-\omega'). \tag{3.18}$$

The linear solution, correlator and propagator are

$$\begin{aligned} \phi_0(q,\omega) &= \frac{G_0(q,\omega)}{q^2}\eta, \\ G_0(q,\omega) &= \frac{q^2}{-i\omega + \kappa q^4}, \\ C_0(q,\omega) &= \frac{2Dq^2}{\omega^2 + \kappa^2 q^8}, \end{aligned} \tag{3.19}$$

where η is the noise in Fourier space, so that it has variance

$$\langle \eta(q,\omega)\eta(q',\omega')\rangle = 2Dq^2(2\pi)^{d+1}\delta^d(q+q')\delta(\omega+\omega'). \tag{3.20}$$

Lastly, we have defined the vertex function $g(q,q')$, that comes from the Fourier transform of the λ and ζ terms, and that has the following form when symmetrized

$$g(q,q') = -2\lambda q'\cdot(q-q') + \frac{\zeta}{q^2}\left(q'^2 q\cdot(q-q') + (q-q')^2 q\cdot q'\right). \tag{3.21}$$

Notice that equation 3.18 has a relatively simple structure, with only one nonlinearity, quadratic in the fields, which makes the RG treatment rather simple. The first step consists of integrating out wavevectors on a thin shell close to the cutoff $(\Lambda/(1+db), \Lambda)$. This is done perturbatively, to one loop, following the steps of Chapter 2. So we need to consider one loop diagrams that contribute to the parameters of our equation of motion: $(\kappa, D, \lambda, \zeta)$.

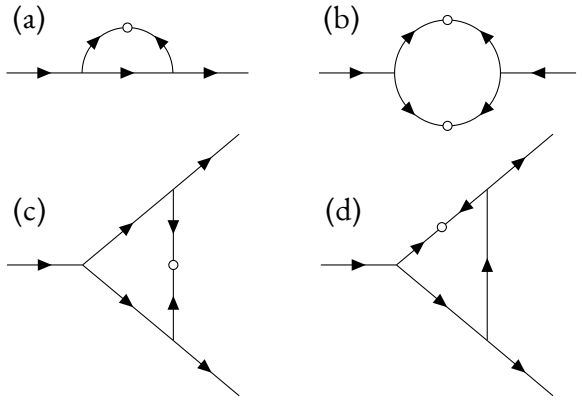

Figure 3.2: One loop diagrams that contribute to the different terms of cKPZ+. The first contributes to κ, the second contributes to the noise D, and the triangle diagrams contribute to the nonlinearities.

Consider first the diagram that would contribute to the noise via its q^2 term. This term actually vanishes, and it is easy to see how. By manipulating the equation of motion, we can write

$$(-i\omega + q^2(a + \kappa q^2))\phi = \eta + \frac{q^2}{2}\int_{q',\omega'} g(q,q')\phi(q',\omega')\phi(q-q',\omega-\omega'). \tag{3.22}$$

Notice that we have just rewritten equation 3.18. It is easier to see here, though, that the q^2 in front of the integral comes from conservation of ϕ. The diagram will therefore have a $2Dq^2$ term coming from the average value of the noises, and the contribution to D will come from the q^2 term of the diagram. The diagram integrates $q^4 g(q', q-q')^2 C_0(q',\omega')C_0(q-q',\omega-\omega')$, so we have to extract the q^2 term of this.

By doing a Taylor expansion of this expression, we immediately see that the q^2 term vanishes, and the first nonvanishing term is of order q^4. This means that we do not generate corrections to D to this order, and the first noise we generate has a variance of higher order in q, making it irrelevant in the RG sense.

This also allows us to deduce a more general property for conserved surface models, which is that the noise is not corrected by this step of the RG procedure at any order, since any term that might contribute will have a q^4 on the front multiplying terms that are going to be regular at $q = 0$ [33].

The triangular diagrams of Figure 3.2 might contribute to λ and ζ, since they are quadratic in the outcoming fields. However, a not very enlightening calculation (and thus left to Appendix B) shows that they cancel each

other, meaning that this model does not create corrections, at least to 1 loop, to the nonlinearities that break time reversal symmetry.

We are therefore left with only one diagram to calculate. Observe that it is linear in the outcoming field, and so it can only produce a correction to κ.

The fact that λ and ζ do not have any corrections may lead to wrongly assume that their flow is trivial. However, notice that we require our flow to preserve κ, and since the correction to κ is quadratic in λ and ζ, this can produce a nontrivial flow for the nonlinearities.

The loop of the remaining diagram represents the following integral

$$G_0(q,\omega)\int_{q',\omega'} g(q,q')g(q-q',q)C_0(q',\omega')G_0(q-q',\omega-\omega'). \quad (3.23)$$

The integral in the time frequency domain can be computed exactly via a contour integral, the result being

$$\int_{-\infty}^{\infty}\frac{d\omega'}{2\pi}C_0(q',\omega')G_0(q-q',\omega-\omega') = \frac{D}{\kappa^2}\frac{(q-q')^2}{q'^2[(q-q')^4+q'^4]}. \quad (3.24)$$

The loop integral becomes

$$\begin{aligned}\frac{D}{\kappa^2(2\pi)^d}\int_{q'}&\left[-2\lambda q'\cdot(q-q')+\zeta\frac{q'^2 q\cdot(q-q')}{q^2}+\zeta\frac{(q-q')^2 q\cdot q'}{q^2}\right]\\ &\times\left[2\lambda q\cdot q'+\zeta\frac{q'^2 q\cdot(q-q')}{(q-q')^2}+\zeta\frac{q^2(-q')\cdot(q-q')}{(q-q')^2}\right]\\ &\times\frac{(q-q')^2}{q'^2[(q-q')^4+q'^4]}.\end{aligned} \quad (3.25)$$

The next step is to expand the integrand as a power series of q. Notice that, there are no divergences at small q and that the q^0 term vanishes, so that the first contribution, as expected is the q^2 term that is to be reabsorbed by κ. The angular integrals can be calculated with the techniques presented in Appendix A. Equation 3.25 thus equals

$$\kappa\Omega_d M(\bar\lambda,\bar\zeta,d)\int_{\Lambda/b}^{\Lambda}x^{d-3}dx, \quad (3.26)$$

where $M(\bar\lambda,\bar\zeta,d)$ is defined as follows

$$\begin{aligned}&M(\bar\lambda,\bar\zeta,d) =\\ &\quad\frac{1}{2d(d+2)}\left[(2d^2-3d-2)\bar\zeta^2+4d(d+2)\bar\lambda\bar\zeta-4(d+2)\bar\lambda^2\right]\end{aligned} \quad (3.27)$$

In the previous expression we have defined the reduced couplings $\bar{\lambda}$ and $\bar{\zeta}$, defined as $(\bar{\lambda}^2, \bar{\zeta}^2) = D\kappa^{-3}(\lambda^2, \zeta^2)$, equivalent to setting $D = \kappa = 1$ in the equation of motion. This is fine since our flow will keep these two parameters fixed.

Now that the only nonvanishing diagram has been calculated, the intermediate value for κ can be written

$$\kappa_I = \kappa \left(1 - M(\bar{\lambda}, \bar{\zeta}, d)\Omega_d \int_{\Lambda/b}^{\Lambda} x^{d-3} dx \right). \tag{3.28}$$

The remaining step to get the RG flow is to rescale the equation of motion, with this intermediate value for κ, back to the original cutoff. Each quantity is then rescaled as follows

$$\begin{aligned} q &\mapsto bq, \\ \omega &\mapsto b^z \omega, \\ \phi &\mapsto b^{-\chi} \phi. \end{aligned} \tag{3.29}$$

Since we fixed the units of the $\dot{\phi}$ term by setting its coefficient to 1, there is only one way to absorb this rescalings. After doing so and sending b to be infinitesimally above 1, $b \mapsto 1 + db$, we get the flow equations

$$\begin{aligned} \frac{d\kappa}{db} &= \kappa \left(z - 4 - M(\bar{\lambda}, \bar{\zeta}, d)\Omega_d \right), \\ \frac{dD}{db} &= D(z - 2 - d - 2\chi), \\ \frac{d(\lambda, \zeta)}{db} &= (\lambda, \zeta)(z + \chi - 4), \end{aligned} \tag{3.30}$$

where, without loss of generality, we have set $\Lambda = 1$, to make the analysis simpler.

The only nontrivial flow is the one of κ, however, for consistency with the approach to the Gaussian fixed point, we impose κ and D to be fixed under the RG flow. This requirement for D sets a relation between exponents, $z - 2 - d - 2\chi = 0$. Therefore, it is more useful to write the flow of the reduced parameters $(\bar{\lambda}, \bar{\zeta})$. Using equations 3.30, we obtain

$$\frac{d(\bar{\lambda}, \bar{\zeta})}{db} = (\bar{\lambda}, \bar{\zeta}) \left(\frac{2 - d}{2} + \frac{3}{2} M(\bar{\lambda}, \bar{\zeta}, d)\Omega_d \right). \tag{3.31}$$

This is the main technical result for cKPZ+. The fixed points can be obtained by setting this last equation to 0. The solutions, at a given dimension d, are given by the conics in the $(\bar{\lambda}, \bar{\zeta})$ plane, defined by

$$\Omega_d M(\bar{\lambda}, \bar{\zeta}, d) = \frac{d - 2}{3}. \tag{3.32}$$

This allows us to calculate approximations for the critical exponents in nontrivial fixed points, by substituting this last equation in the equation for the flow of κ, equation 3.30. By, again, fixing κ and D, we obtain

$$\begin{aligned} z &= 4 - \frac{\epsilon}{3} + \mathcal{O}(\epsilon^2), \\ \chi &= \frac{\epsilon}{3} + \mathcal{O}(\epsilon^2), \end{aligned} \tag{3.33}$$

where we have finally substituted the dimension d with our small parameter $\epsilon = 2 - d$. Notice that these exponents are the ones of the cKPZ model [38], and indeed they should match in 1 dimension, at which both cKPZ and cKPZ+ are the same model.

It is best to analyse the RG flow separately for each dimension interval in which the behaviour is different. This is, for $d = 1$, $d < 2$, for $d = 2$, and for $d > 2$. These four cases are depicted in Figure 3.3.

Below 2 dimensions, the Gaussian fixed point becomes unstable, and the nontrivial fixed points are the conics depicted in Figure 3.3, top right. The flow thus leads the system to these lines of fixed points unless the starting set of parameters is outside the dotted lines defined by the asymptotes of the conic lines. In that case the flow runs away to infinity. This problem can be avoided by observing that the only physical dimension below 2 is $d = 1$, dimension at which the λ and ζ parameters are mathematically equivalent, and we recover the usual conserved KPZ. This is represented in Figure 3.3, top left, which depicts the unstable Gaussian fixed point and how the flow takes the system to a finite value of $\bar{\lambda}$.

This means that in 1 dimension, cKPZ+ has the same behaviour as cKPZ, as it must. The stability of this new point means that, at large scales in space and time, the surface will grow according to equations 3.14 and 3.13 with the critical exponents of this fixed point.

In 2 dimensions, we observe that the lines of fixed points collapse into two straight lines, and the flow becomes marginal, but unlike the case of cKPZ, now we have two different regions of marginality. In part of the plane (where the arrows in Figure 3.3, bottom left, point inwards), the system flows back to equilibrium, i.e. to the behaviour of the Mullins' equation, as cKPZ, so λ and ζ are marginally irrelevant. However, in the rest of space the system flows away, making them marginally relevant. This is new behaviour not observed before that hints to the existence of a strong coupling regime, not accessible by our perturbative method, that would drive the behaviour of the system. This new behaviour is present due to ζ (observe that the axis $\zeta = 0$ has the usual cKPZ behaviour of a marginally stable Gaussian fixed point).

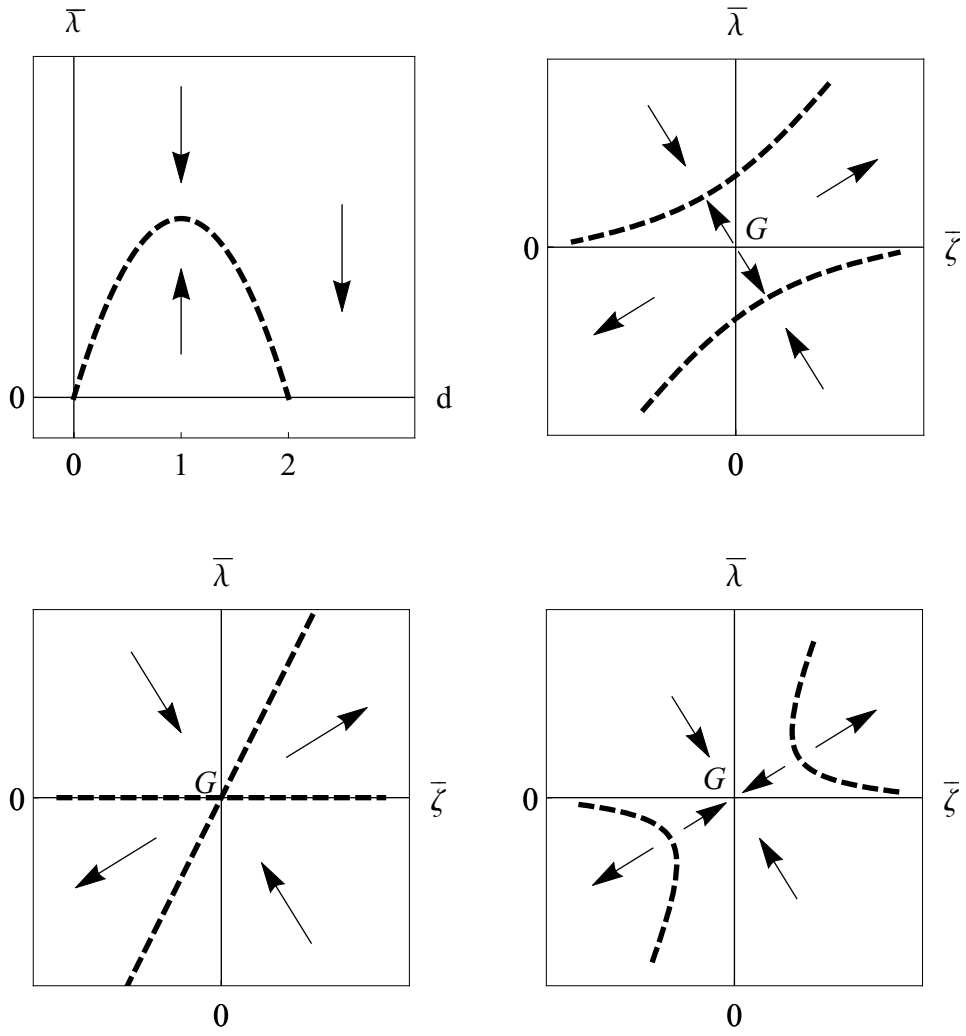

Figure 3.3: RG flow of the cKPZ+ equation, with the dashed lines representing the lines of fixed points. Top left is the flow with $\bar{\zeta} = 0$ as a function of d, so it must be taken as the flow of cKPZ+ in 1 dimension at which ζ and 2λ are mathematically equivalent terms; observe that in 1 dimension, the fixed point is attractive. Top right is the flow between 1 and 2 dimensions; in this case the Gaussian fixed point (marked by G in all diagrams), is repulsive, and the lines of fixed points are attractive, thus ruling the behaviour of the system at large scales in space and time. Bottom left is the marginal case in 2 dimensions; the lines of fixed points collapse to two straight lines that cross at the origin, and the Gaussian fixed point is marginally attractive in some directions and marginally repulsive in others. Bottom right is the flow above 2 dimensions, at which the line of fixed points becomes a separatrix between the region of parameter space that flows back to the Gaussian fixed point and the runaway regime that hints to a strong coupling regime, as discussed in the text.

Above 2 dimensions, Figure 3.3 bottom right, the Gaussian fixed point becomes stable, and the lines of nontrivial fixed points becomes unstable. These lines of fixed points now have a different interpretation than the one they have below 2 dimensions. Now, their instability points to a dynamical phase transition into the strong coupling fixed point mentioned above. Notice, again, that the axis $\zeta = 0$ does not cross these lines, so in absence of ζ we recover the result of cKPZ, that behaves like the Mullins' equation above 2 dimensions.

This situation, new in the context of conserved surface growth, deserves more analysis. It resembles the case of the usual KPZ equation, for which we can find a nontrivial fixed point above 2 dimensions, that separates the parameter space in two regions, one with smooth growth and one with rough growth. For the KPZ equation this strong coupling has been investigated through theoretical and numerical methods and its existence is not doubted, although its nature is far from clear.

The fact that the strong coupling fixed point appears above 2 dimensions is surprising since dimensional analysis makes the KPZ nonlinearity IR irrelevant. This seems to mean that the critical dimension of the KPZ equation is not 2 but something higher, since there is still a non mean field behaviour above 2 dimensions. Finding the upper critical dimension of the KPZ equation has proved to be a difficult task [44], even using numerical techniques, with some studies using phenomenological field theories that suggest it is $d_c = 4$ [45], some others based on self-consistent expansions and functional renormalization schemes proposing it is just slightly above 2, at $d_c \approx 2.5$ [46], and some other studies of the width distributions even suggesting that the critical dimension is infinity [42], meaning that the strong coupling regime exists in any dimension.

In principle the same complexity could be present in the cKPZ+ equation, since its strong coupling regime is also found to be the effect of IR irrelevant nonlinearities above 2 dimensions. We will therefore dedicate the rest of the Chapter to an initial investigation of this regime. We cannot say a priori that for cKPZ+ this strong coupling point really exists and is not just an artefact of the perturbative approach, it may indeed disappear if analysed through other methods, such as nonperturbative renormalization group, or going to higher loop order. To rule out this last case, the next section will discuss numerical simulations of the equation of motion of cKPZ+.

3.2 NUMERICAL INTEGRATION OF THE CKPZ+ EQUATION

In order to investigate this strong coupling regime, we will study the equation of motion of cKPZ+ numerically in 2 dimensions, since it is the lowest dimension for which the RG flow points to a strong coupling regime in a region of parameter space.

Notice that, since we would expect the strong coupling regime to show rough growth, integrating numerically equation 1.16 might not be a good idea, since the high gradients will be numerically unstable if the surface is not smooth. We therefore will integrate the equation in Fourier space but real time.

One more optimization we do, purely for computational reasons, is not calculating the convolutions of the nonlinearities directly (since the naive calculation of a convolution is of order $\mathcal{O}(N^2)$ for a space of size N), but to use a pseudospectral method, in which we calculate each gradient in Fourier space, then transform to real space, calculate the nonlinearities in real space through simple multiplication, and then transform back to Fourier space. Fourier transforms can be calculated in $\mathcal{O}(N \log N)$ time, so this saves a lot of computation time. The particular equation we integrate is then

$$\begin{aligned}\dot{\phi} = &- q^4(\kappa + \kappa_6 q^2)\phi \\ &- q^2\lambda\mathcal{F}\left[|\mathcal{F}^{-1}[-iq\phi]|^2\right] \\ &+ i\zeta q \cdot \mathcal{F}\left[\mathcal{F}^{-1}[-q^2\phi]\mathcal{F}^{-1}[-iq\phi]\right] + \eta,\end{aligned} \tag{3.34}$$

where $\mathcal{F}$ is the Fourier transform operator. Observe we have included the κ_6 term, also for stability purposes. This is equivalent to a term of the form $\kappa_6\nabla^6\phi$ in the dynamics, which could come from a higher order term of the free energy. This term is irrelevant in the RG sense, and so should not change the critical properties in 2 dimensions, but will help make the system stable at high q values, where we will likely find stability issues.

The time integration is done using Heun's method, and the pseudospectral calculations are done with a $2/3$ de-aliasing [47]. This means setting part of the lattice in Fourier space to 0 (in particular the two thirds of the lattice with the highest wavevectors), in order to avoid numerical artefacts from appearing as these wavevectors might loop around the lattice when calculating nonlinearities.

As mentioned above, we will measure the width of this system in the numerical simulation, since its behaviour gives information about the critical exponents according to equations 3.14 and 3.13.

The Mullins' equation has logarithmic behaviour in 2 dimensions, since $\chi = 0$. This is what is observed for cKPZ in 2 dimensions and above, since

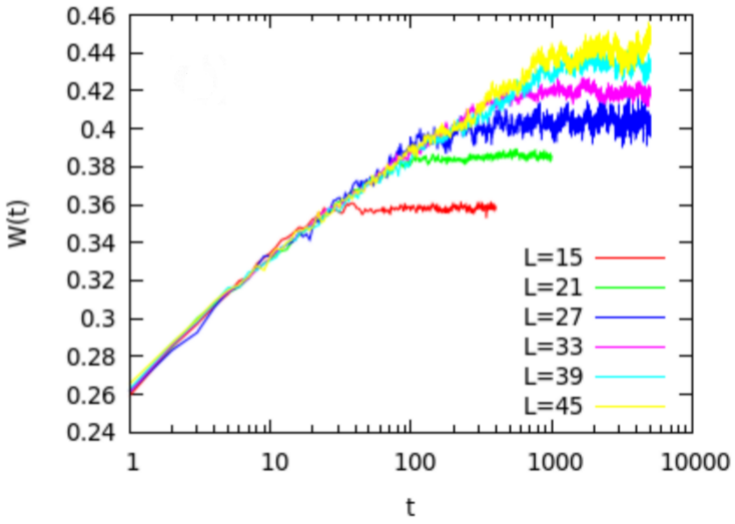

Figure 3.4: Growth of the width for several system sizes in the region of parameter space where the RG flow takes the system to the Gaussian fixed point. The particular values used were $\lambda = -1/2, \zeta = 2.6$.

λ is irrelevant and the system flows back to the Gaussian fixed point. We will therefore study simulations of cKPZ+ in regions of parameter space for which the RG flow predicts weak and strong coupling behaviour. First we simulate the system in the weak coupling regime.

3.2.1 *Weak coupling regime*

What we observe here is logarithmic growth of the width, such as those of Figure 3.4. Observe that as we increase the system size L, both the value of the saturated width and the time it takes to be reached increase. In Figure 3.5 the saturated width is plotted against the size of the system with a logarithmic fit, showing the expected growth, and in Figure 3.6 the time of saturation $t_s(L)$ is plotted as a function of the system size. We would expect the relation between these two to be of the form $t_s \sim L^z$, and the figure shows a fit compatible with the value $z = 4$ of the Mullins' equation, in particular a free fit gives $z = 3.8 \pm 0.2$.

One detail to have in mind about these simulation is that a single time integration of the cKPZ+ is very noisy, so to get smooth growth lines we average growths of many realizations of the noise. How many runs we average for each of them depends on practical issues such as how long it takes to integrate the equation and how many times we have to integrate to ob-

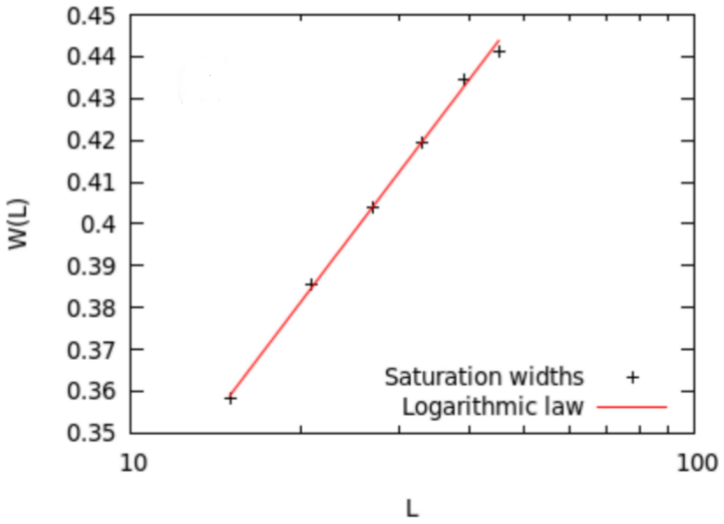

Figure 3.5: Saturation width as a function of the system size in the region of parameter space where the RG flow takes the system to the Gaussian fixed point.

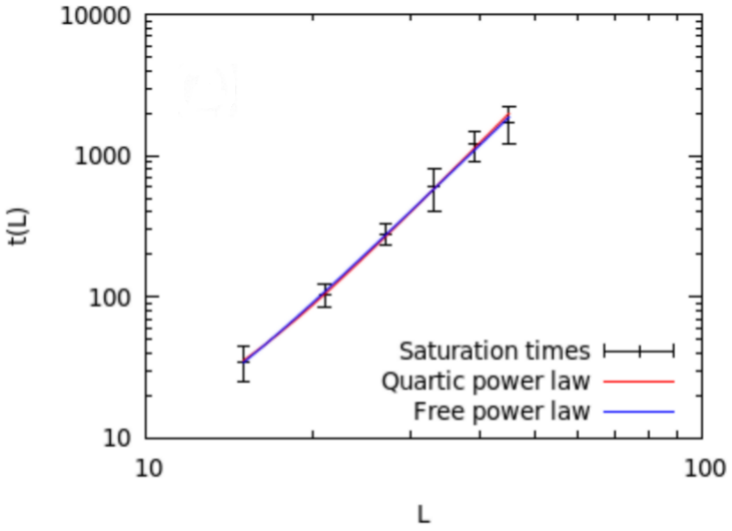

Figure 3.6: Saturation time as a function of the system size in the region of parameter space where the RG flow takes the system to the Gaussian fixed point. The blue line is a power law fit that gives a slope of $z = 3.8 \pm 0.2$. The red line is the analytical result of $z = 4$.

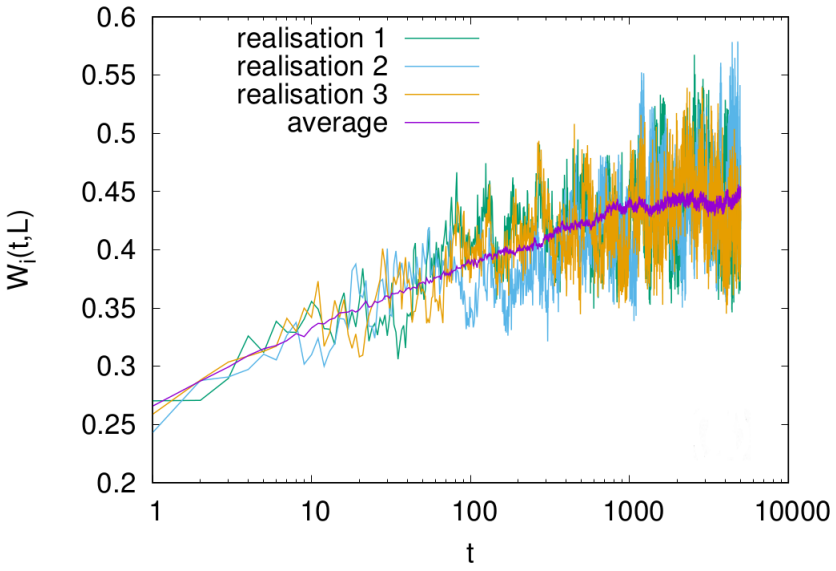

Figure 3.7: Single runs along with an average of a few hundreds to illustrate the typical variance of a single run. The values used here were $\lambda = -1/2, \zeta = 2.6$.

tain a relatively smooth line, and the particular number of averages ranges between 1600 for the smaller system sizes and 80 for the largest. Figure 3.7 shows the typical growth of three single runs and the average of a few hundreds to show the variance of single runs in the weak coupling regime.

The value of the parameter κ_6 is set to 0 in these simulations, and will be more useful in the strong coupling regime, where we find problems with the stability of solutions, however, it was also checked that it changes nothing about the growth laws in this regime.

3.2.2 *Runaway regime*

The situation when we move into the region where the RG flow runs away from the Gaussian fixed point is dramatically different, and we have to include κ_6 to obtain numerically stable results. What we observe is an initial transient power law period that leads into a second regime in which the width grows much faster than logarithmically. At large enough sizes of the system, this second regime seems to be another universal power law, although due to our limitations in time and system size we cannot confirm this precisely its nature. Figure 3.8 shows this growth for several system sizes, where the power law can be seen, as well as a the time at which this new

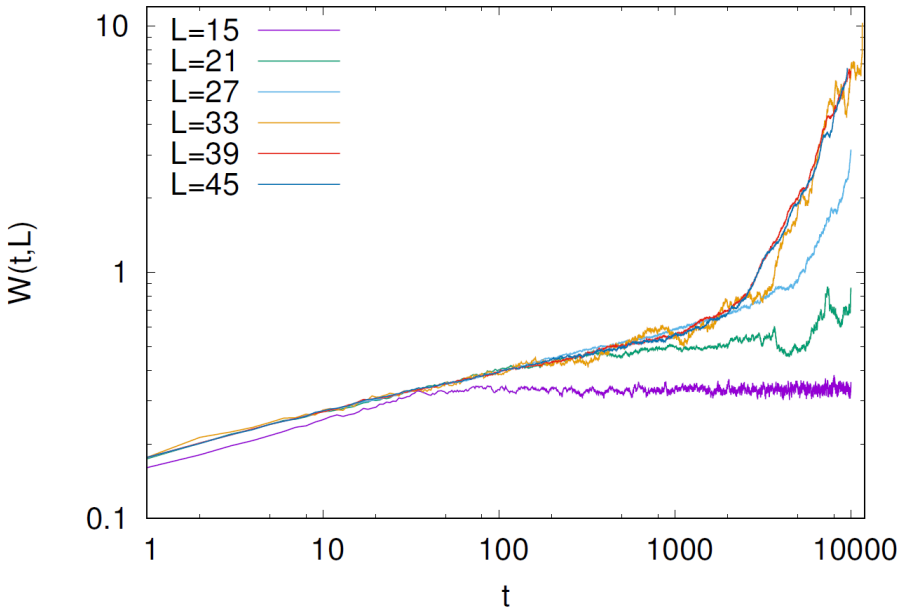

Figure 3.8: Growth of the width in the runaway region of parameter space. For these runs the values used were $2\lambda = \zeta = 1$, $\kappa_6 = 0.6$. The late time growing seems to not depend on the system size for big enough sizes.

growth kicks in, that also seems to become independent of the system size for large enough sizes.

These results are also obtained from averaging many runs with different noise realizations (in this case from 1600 averages for $L = 15$ to 400 averages for $L = 45$), and observe in Figure 3.9 that the variance of single runs is much higher in this case than in the weak coupling regime. One last detail is that κ_6 helps to keep the simulations numerically stable, and the time at which the second growth regime emerges seems to depend on κ_6, but does never disappear (see Figure 3.10).

Unfortunately, due to limitations of computational time and resources, we cannot properly characterize the nature of this phase, and different approaches would be needed to identify with some accuracy, for instance, the power law of the new growth. This is in part due to the small sizes used for the lattice, although, again, due to time limitations and the fact that many simulations have to be run and averaged, we could not perform simulations in much bigger lattices.

We could not however compare any such power law to predictions since the perturbative RG flow predicts a transition to a strong coupling regime but says nothing about the behaviour in this regime, equivalent to how the

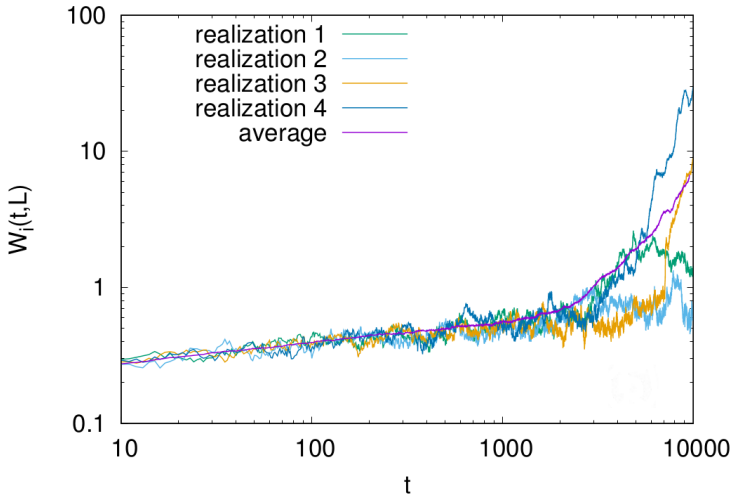

Figure 3.9: Typical single runs with an average of a few hundreds in the runaway region of parameter space. The values used were $2\lambda = \zeta = 1$, $\kappa_6 = 0.6$.

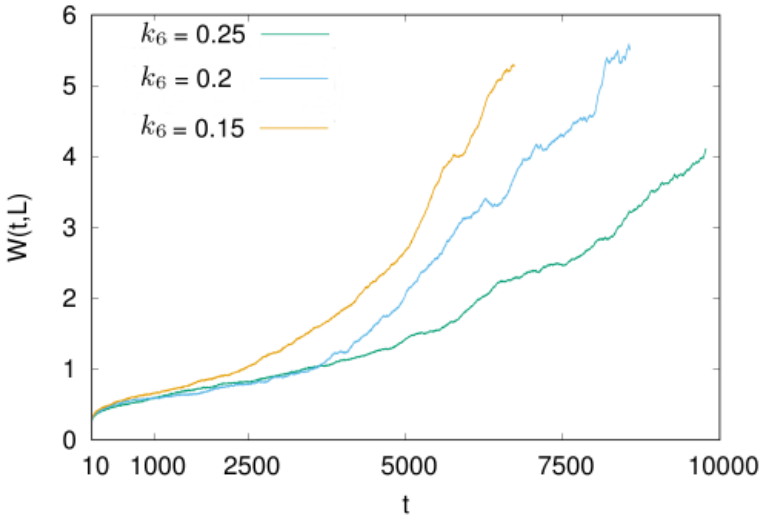

Figure 3.10: Growth of the width for different values of κ_6. Transient time depends on this. The values used were $2\lambda = \zeta = 1$.

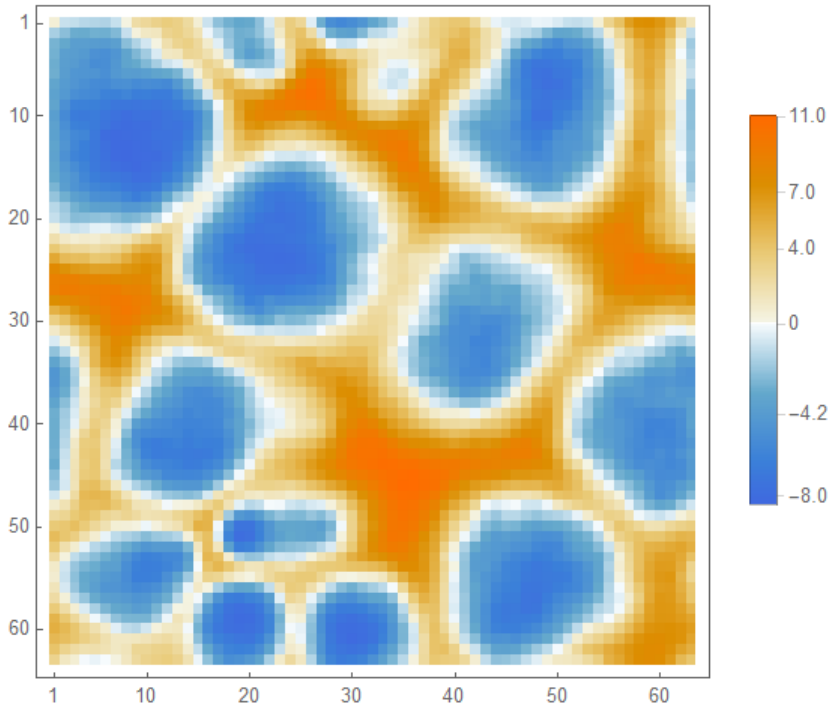

Figure 3.11: Snapshot of the system evolving in the runaway regime. The values used were $2\lambda = \zeta = 1$.

same calculation predicts a strong coupling regime for the KPZ equation, but entirely different methods are needed to study the nature of the strong coupling fixed point, like nonperturbative RG [48, 49] or direct numerical simulations [50, 51].

These simulations give clear evidence that the behaviour of the system is radically different in the runaway region of parameter space, and that it is not just an artefact of the 1-loop calculation. As can be seen in Figure 3.11, which is a snapshot of one of the runs in this regime, there seem to be localized peaks that coarsen, giving the late time growth. This mechanism looks similar to how the same nonlinearities could drive bubble formation in AMB+ [26], or how the same nonlinearities in different growth equations, and for a particular combination of them, favour mound formation [52], see for example the similarity between 20.3 in [44] and Figure 3.11, or references [41, 53, 54]. In fact, one particular combination of the λ and ζ terms has been studied without noise [54], showing that some combination of these nonlinearities can produce blow-up solutions.

Different methods, out of the scope of this thesis, would therefore be necessary to properly study the nature of this new runaway regime, to show

whether it is really a strong coupling regime with infinite correlations, or some other kind of phase, like a trivially scale invariant phase (similar to a high temperature phase), or a phase with a finite correlation length, not described by scale invariance except at the transition threshold between the Gaussian regime and this new phase. However, it is clear from both our analytical results and simulations that the cKPZ equation is incomplete to describe the nonequilibrium evolution of surfaces that grow via slope-unbiased particle jumps, as described by cKPZ+.

The results of this Chapter, in particular the nature of the RG flow we obtain, will transfer to the next chapter, where we analyse the critical properties of AMB+, and they will help understand the results.

4

ACTIVE MODEL B+

This Chapter reports the results of the RG study of the main model of this thesis, AMB+, as defined in section 1.2.1. These results have been published in [55]. We start by just writing again the equation of motion we are studying

$$\begin{aligned}\dot{\phi} =&\nabla^2\left(a\phi + u\phi^3 - \kappa\nabla^2\phi\right) + \\ &\nabla^2\left(\lambda(\nabla\phi)^2 + \frac{\nu}{2}\nabla^2\phi^2\right) - \zeta\nabla\cdot[\nabla^2\phi\nabla\phi] + \eta,\end{aligned} \tag{4.1}$$

where the correlations of the noise η are

$$\langle\eta(r,t)\eta(r',t')\rangle = 2D(i\nabla)^2\delta^{(d)}(r-r')\delta(t-t'). \tag{4.2}$$

Notice that we recover Model B by setting $\lambda = \nu = \zeta = 0$, and, as shown in Chapter 2, Model B lies in the conserved Ising universality class with a dynamic exponent $z = 4$ at Gaussian level.

We therefore might expect the results of this model to be corrections to this passive universality class. In terms of the new nonlinearities, observe that they are, mathematically, the same as for cKPZ+, except for ν. This third nonlinearity makes now the model complete if regarded as an expansion in gradients and fields, up to the order of four gradients and two fields. As explained in the previous Chapter, this new term was not there before because it breaks the $\phi \mapsto \phi + h$ symmetry of a surface model. This symmetry is not present now, though, so this term must be included.

The first step is to calculate the natural dimension of the new terms. This can be done by simply rescaling the equation of motion and making, for consistency with the expansion around the Gaussian model, κ and D be fixed under this rescaling. This is however the same that was done for cKPZ+, since both fixed terms are on an equal footing here as they were in the cKPZ+, and so λ, ζ and ν change relevance at dimension 2.

This already allows to conclude how the system will behave at a qualitative level assuming the system lies close enough to the Gaussian or Wilson Fisher fixed points around which we will study the behaviour of the more complete AMB+. Above 2 dimensions, the new nonlinearities are irrelevant in the RG sense, so, if they are small enough, the system must flow back to the Gaussian fixed point (above 4 dimensions) or to the Wilson

Fisher fixed point (below 4 dimensions). AMB+ must then lie in the conserved Ising universality class if the new nonlinearities are small enough.

It may seem like this renders the critical behaviour of AMB+ uninteresting. However, we found for cKPZ+ that the nonlinearities have a threshold, above 2 dimension, that introduced a runaway regime for the system, pointing to a new phase. We will find, indeed, that this behaviour is present in AMB+ as well above 2 dimensions.

4.1 RENORMALIZATION GROUP RESULTS FOR AMB+

To find out, then, whether this strong coupling regime exists in AMB+ we will find the anomalous dimensions of the new nonlinearities. Following the steps of Chapter 2, we will perform the one-loop calculation of AMB+. As a first step, it is useful to write the equation of motion in Fourier space

$$\begin{aligned}\phi(q,\omega) = \phi_0(q,\omega) + \frac{1}{2}G_0(q,\omega)\int_{q'} g(q,q')\phi(q',\omega')\phi(q-q',\omega-\omega') \\ - uG_0\int_{q',q''}\phi(q',\omega')\phi(q'',\omega'')\phi(q-q'-q'',\omega-\omega'-\omega'').\end{aligned} \tag{4.3}$$

The bare correlator G_0 and the vertex function g differ from the cKPZ+ in that now there is a mass a and the vertex function must contain the term ν:

$$\begin{aligned}\phi_0(q,\omega) &= \frac{G_0(q,\omega)}{q^2}\eta, \\ G_0(q,\omega) &= \frac{q^2}{-i\omega + q^2(a+\kappa q^2)}, \\ C_0(q,\omega) &= \frac{2Dq^2}{\omega^2 + q^4(a+\kappa q^2)^2}, \\ g(q,q') &= 2\lambda q'\cdot(q-q') + \nu q^2 \\ &\quad - \frac{\zeta}{q^2}\left[q'^2 q\cdot(q-q') + (q-q')^2 q\cdot q'\right].\end{aligned} \tag{4.4}$$

The next step is to integrate out high wavevectors in a thin shell $q \in (\Lambda/b, \Lambda)$. To one loop, this enters in the equation of motion as the diagrams in Figure 4.1.

Notice that diagrams (d) and (e) are the ones of Model B, so they are calculated in Chapter 2. Diagram (b), which would renormalize the noise strength, vanishes for the same reason it did in the case of cKPZ+.

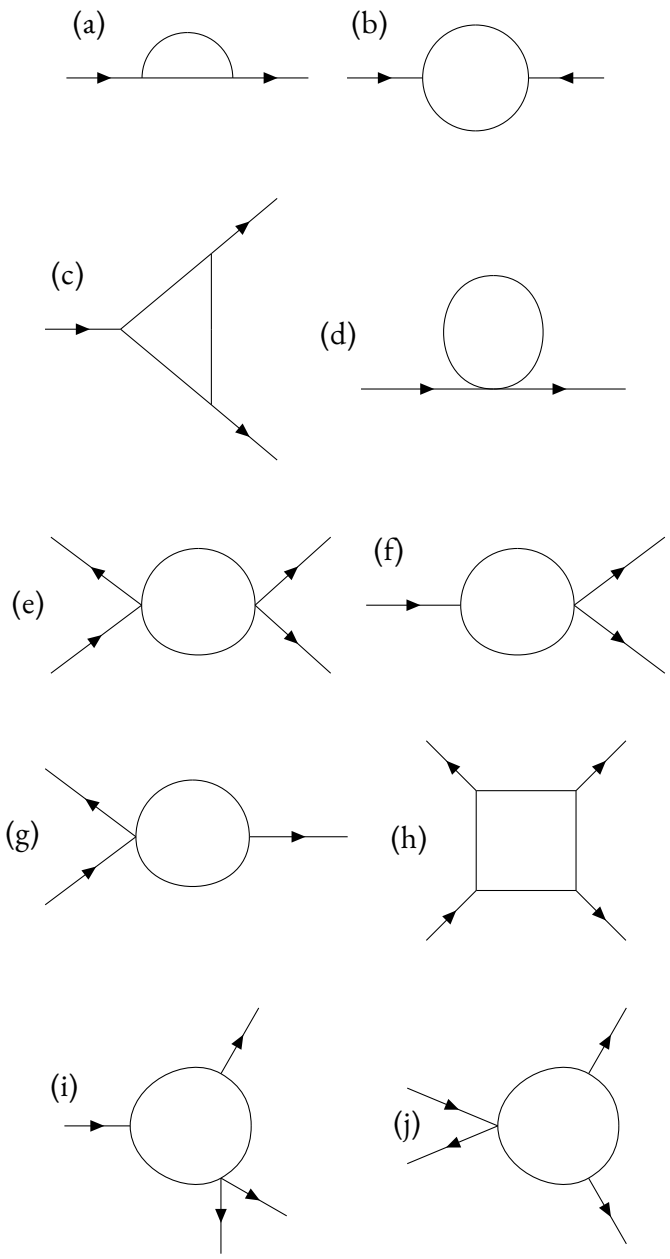

Figure 4.1: One-loop diagrams of AMB+. The first three are topologically the same as the ones we found in the case of cKPZ+, the next two are the ones of standard Model B, (f) and (g) produce new contributions to the active nonlinearities, and the last three renormalize u due to the active nonlinearities. The distribution of the propagators and correlators in the loop has been omitted here for convenience, since some diagrams represent more than one contribution depending on where the correlator is located (i.e. which particular iteration of the equation of motion produces it). These different contributions are written out explicitly in Appendix C.

Diagrams (f) and (g) might produce (and they indeed do), a term of the form $\nabla^2\phi^2$ in the dynamics, not present before. This is equivalent to a cubic term ϕ^3 in the free energy of the system. The reason this happens is that λ, ζ and ν break the $\phi \mapsto -\phi$ symmetry of the system, and so this term should be generated if not present from start.

Notice that in a conserved Ising system the phase transition is first order in general in the presence of a term of the form $c\phi^3$ in the free energy, which comes in the phase diagram as a tilted bell of phase coexistence. A second order transition can be found, though, by a shift of the field (that induces a shift in a) to recover the $\phi \to -\phi$ symmetry. For this kind of standard field redefinition see, for example, Chapter 10 of [56]. This means that cubic terms change the parameters at which the critical point is found, and the second order transition can be found by the appropriate fine-tuning of parameters. In the language of the liquid-vapour transition, the second order transition can be found at the end of the first order transition line.

The cubic term induces the same kind of first transition that will be present in general in AMB+. This term can be dealt with through an additive shift to the field that ensures that the critical density remains zero, or equivalently, that ϕ is always defined with respect to the critical density of the continuous phase transition. This has to be done at each step of the Renormalization Group (although will be done implicitly), and it is equivalent to what is done to study the liquid-vapour critical point, where there is no symmetry between positive and negative order parameters, but where we can find the second order transition by tuning our parameters to a specific value.

The explicit calculations of each of these diagrams are in Appendix C, and they produce the following intermediate values

$$\begin{aligned}
a_I &= a + 3K\bar{u}\Omega_d\Lambda^{d-2}db + \frac{K\bar{\nu}}{2d}\left[(d-2)\bar{\zeta} + 2d\bar{\lambda}\right]\Omega_d\Lambda^d db,\\
D_I &= D,\\
K_I &= K\left(1 - M\Omega_d\Lambda^{d-2}db\right),\\
u_I &= u\left(1 - 9\bar{u}\Omega_d\Lambda^{d-4}db\right) + \frac{\kappa^2}{D}C_1\Omega_d\Lambda^d db + \frac{\kappa^2}{D}C_2\Omega_d\Lambda^{d-2}db,\\
\nu_I &= \nu + \frac{K^{3/2}}{D^{1/2}}\left(T_{\bar{\nu}}\Lambda^{d-2} + B_{2,\bar{\nu}}\Lambda^{d-4} + B_1\Lambda^{d-4}\right)\Omega_d db,\\
\lambda_I &= \lambda + \frac{K^{3/2}}{2D^{1/2}}\left(T_{\bar{\lambda}}\Lambda^{d-2} + B_{2,\bar{\lambda}}\Lambda^{d-4}\right)\Omega_d db,\\
\zeta_I &= \zeta - \frac{K^{3/2}}{D^{1/2}}T_{\bar{\zeta}}\Lambda^{d-2}\Omega_d db,
\end{aligned} \tag{4.5}$$

where, as in the previous cases, we have written all contributions in terms of the reduced couplings $\bar{\lambda}^2 = \lambda^2 D\kappa^{-3/2}$, $\bar{\zeta}^2 = \zeta^2 D\kappa^{-3/2}$, $\bar{\nu} = \nu^2 D\kappa^{-3/2}$, $\bar{u} = uD\kappa^{-2}$, $\bar{a} = a/\kappa$. We have also introduced, for convenience, the following definitions

$$
\begin{aligned}
M =& \frac{1}{2d(d+2)}\Big[d\bar{\zeta}((4-d)\bar{\nu}+4(d+2)\bar{\lambda}) \\
&+ (d-2)(2d+1)\bar{\zeta}^2 - (d+2)\left(2d\bar{\lambda}\nu - d\bar{\nu}^2 + 4\bar{\lambda}^2\right)\Big], \\
T_{\bar{\nu}} =& \frac{\bar{\nu}}{d(d+2)}\Big[(d-2)(2d+1)\bar{\zeta}^2 + d\bar{\zeta}((4-d)\bar{\nu}+4(d+2)\bar{\lambda}) \\
&- (d+2)\left(2d\bar{\lambda}\bar{\nu} - d\bar{\nu}^2 + 4\bar{\lambda}^2\right)\Big], \\
T_{\bar{\lambda}} =& \frac{\bar{\nu}}{4d(d+2)}\Big[-4\bar{\zeta}(2(d(4d+5)-10)\bar{\lambda} - (d-2)d\bar{\nu}) \\
&- 2(d-2)(7d+4)\bar{\zeta}^2 - 4(d+2)\bar{\lambda}(2(d-2)\bar{\lambda} - 3d\bar{\nu})\Big], \\
T_{\bar{\zeta}} =& \frac{2\bar{\nu}\bar{\zeta}\left[4(d-3)\bar{\zeta} - 8(1+d)\bar{\lambda} - d(6+d)\bar{\nu}\right]}{4d(d+2)}, \\
B_1 =& \frac{3u\left[2(4-d)\bar{\zeta} - (2+d)(4\bar{\lambda}+d\bar{\nu})\right]}{d(d+2)}, \\
B_{2,\bar{\nu}} =& \frac{3u\left[2(d-1)\bar{\zeta} - (d-2)\bar{\nu}\right]}{d}, \\
B_{2,\bar{\lambda}} =& -\frac{6u\left[2(d-1)\bar{\zeta} - (d-2)\bar{\nu}\right]}{d}, \\
C_1 =& \left(\bar{\lambda} + \frac{d-2}{2d}\bar{\zeta}\right)\bar{\nu}^3, \\
C_2 =& -\frac{1}{2}\bar{u}\bar{\nu}\left(12\bar{\lambda} - 9\bar{\nu} + \frac{6(d-2)}{d}\bar{\zeta}\right).
\end{aligned}
\tag{4.6}
$$

The T_i terms come from the triangular diagrams (c), the B_i terms come from the diagrams (f) and (g), and the C_i terms come from diagrams (h), (i) and (j). Notice that M now has all the terms that include ν, and that by setting $\nu = 0$ we recover the results of cKPZ+.

The last step is to rescale the equation of motion with the previous intermediate values to its original cutoff

$$
\begin{aligned}
q &\mapsto bq, \\
\omega &\mapsto b^z\omega, \\
\phi &\mapsto b^{-\chi}\phi.
\end{aligned}
\tag{4.7}
$$

After doing so, taking the limit $b \mapsto 1 + db$, setting the cutoff $\Lambda = 1$ for simplicity, and writing the flow in terms of the reduced parameters, we obtain

$$\begin{aligned}
\frac{d\bar{a}}{db} &= 2\bar{a} + 3\bar{u}\Omega_d + \frac{\bar{\nu}}{2d}\left[(d-2)\bar{\zeta} + 2d\bar{\lambda}\right]\Omega_d + \bar{a}M\Omega_d, \\
\frac{d\bar{u}}{db} &= \bar{u}(4-d) - 9\bar{u}^2\Omega_d + 2\bar{u}M\Omega_d + (C_1 + C_2)\Omega_d, \\
\frac{d\bar{\nu}}{db} &= \bar{\nu}\left(\frac{2-d}{2} + \frac{3}{2}M\Omega_d\right) + \left(T_{\bar{\nu}} + B_{2,\bar{\nu}} + B_1\right)\Omega_d, \\
\frac{d\bar{\lambda}}{db} &= \bar{\lambda}\left(\frac{2-d}{2} + \frac{3}{2}M\Omega_d\right) + \frac{1}{2}\left(T_{\bar{\lambda}} + B_{2,\bar{\lambda}}\right)\Omega_d, \\
\frac{d\bar{\zeta}}{db} &= \bar{\zeta}\left(\frac{2-d}{2} + \frac{3}{2}M\Omega_d\right) - T_{\bar{\zeta}}\Omega_d.
\end{aligned} \tag{4.8}$$

This is the main technical result of this section, and it will be analysed in the next section. Before doing so, it is worth making one last point about how ignoring the cubic term produced by diagrams (g) and (h) does not change the flow. The generated term is of the form $q^2 c\phi^2$ in the equation of motion, for some constant c that comes from the loop integral. Importantly, this constant c is proportional to $c \propto db$ when we take the limit $b \mapsto 1 + db$. If we have a term of this form in the dynamics, the shift to the field that must be made is $\phi \mapsto \phi + c/(3u)$, and this requires a further shift in a of the form $a \mapsto a - 5c^2/(3u)$. This shift is quadratic in db and therefore does not contribute to the flow. It is true, however, that the RG procedure to access this critical point includes an implicit constant shift to the field, equivalent to that of the liquid-vapour transition, and it must be noted that we are accessing a critical point of divergent correlation length in a system that will also display, in general, a first order transition for all noncritical values of the conserved order parameter $\int \phi dr$.

4.2 RESULTS AND ANALYSIS

The resulting flow is quite complex, given that it involves the flow of five coupled quantities, so it will be analysed from several points of view. We will look at different projections close the known fixed points (Gaussian and Wilson-Fisher), as well as at numerical solutions and integrations.

There is another detail that makes our results nonstandard in the RG sense, and that has to do with the fact that we are looking for a threshold to a runaway regime of irrelevant parameters in a system in which the leading nonlinearity is relevant below 4 dimensions. By looking at the flow of

$\bar{u}$, in the region in which the system behaves according to the Gaussian or Wilson-Fisher fixed points, the fixed point in $\bar{u}$ is obtained as an expansion in $\epsilon_4 = 4 - d$, the standard result for Model B as shown in Chapter 2. The fixed points for $\bar{\lambda}, \bar{\zeta}$ and $\bar{\nu}$, though, are found above 2 dimensions as expansions of $\epsilon_2 = d - 2$. This means that whatever fixed points are found between 2 and 4 dimensions, their position will be calculated as the result of two simultaneous expansions in two parameters that cannot be very small at the same time: $4 - d$ and $d - 2$. This is the aspect of this RG calculation that is not completely standard and has to be taken into account when analysing the flow. As these ϕ^4 systems approach 2 dimensions, more and more nonlinearities become relevant, until in 2 dimensions all polynomial expressions of the field are relevant and conformal techniques must be used to access the fixed point.

The results presented in this section should then be regarded as an expansion around the Wilson-Fisher fixed point in the small parameter $\epsilon = d - 2$, with the caveat that we are using the value of the Wilson-Fisher fixed point as the one found by another expansion in $4 - d$. This double ended expansion is though the only approach to the phase diagram of the system through perturbative RG, and we shall see below it manages to capture some of the complexity of the phase diagram analysed numerically in [26]. It would be interesting, however to have systematic method of expanding around the Wilson-Fisher fixed point directly (although this cannot be done through perturbative RG), since this would allow for a classic and completely self-consistent single expansion in $d - 2$.

4.2.1 *Slices of the flow*

A first analysis of the RG flow can be done by looking at slices of the flow, since visualizing a four-dimensional flow can be quite complicated.

By taking a slice of the flow, we understand choosing a two-dimensional plane in the space of parameters, and looking at the flow only on that plane. If the flow in that plane is not contained within it, and there are orthogonal components (as will be the case), we then project the flow onto that plane. If we choose the planes to be those defined by setting some of our parameters to be constants, then taking slices of the flow is equivalent to artifically fixing some of the parameters and looking at how the rest flow. The next section will study complete integrations of the RG flow to compare with these slices.

Firstly, it is specially useful to look at two slices of the flow close to the Gaussian and Wilson-Fisher fixed points. The first is onto the $(\bar{\lambda}, \bar{\zeta})$ plane,

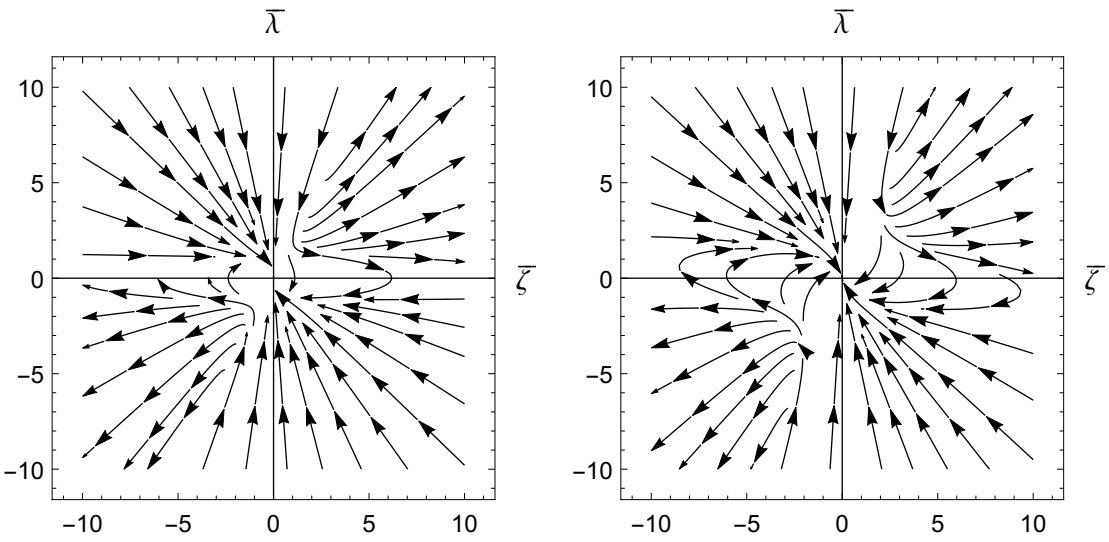

Figure 4.2: Slice of the flow of AMB+ projected on the $(\bar{\zeta}, \bar{\lambda})$ plane in 2 (left) and 3 (right) dimensions.

which will help us compare to the results of the cKPZ+ for which we have a clear concept of what a runaway regime looks like.

We have to choose for which values of $\bar{u}$ and $\bar{\nu}$ to project the flow ($\bar{a}$ does not come in the flow of the rest of the parameters so can be ignored for now). The obvious choices are the fixed points around which we expand. For $d > 4$ dimensions, this is $\bar{u} = 0$ (the Gaussian fixed point), and $\bar{\nu} = 0$. In this case, though, observe that we recover the flow of cKPZ+ and so the situation will be the one of Figure 3.3(bottom right), so we know the strong coupling regime remain in this model when expanding close to the Gaussian fixed point. Below four dimensions, we must expand close to the Wilson-Fisher fixed point. For $\nu = 0$, this means the flow of $\bar{\lambda}$ has an extra term proportional to $\bar{u}$, which is $\Omega_d B_{2,\bar{\lambda}}/2$.

Notice, though, that since this term is linear in ζ, for big values of λ and ζ, we recover the asymptotic regions of cKPZ+ in which the flow either takes the system to the origin of runs away from it. In more than 2 dimensions, the same structure remains, see Figure 4.2, where the threshold changes and moves away from the origin (since it is given by an expansion in $d - 2$), as in the case of the cKPZ+. For high values of $\bar{\lambda}$ and $\bar{\zeta}$, the flow of these is $d(\bar{\lambda}, \bar{\zeta})/db \sim (\bar{\lambda}, \bar{\zeta})M$, so it becomes radial again, and so the asymptotic converging and runaway regions in this projection are the same as in the cKPZ+ model. This radiality is not present close to the origin, though.

The second main insight into this flow comes from looking at slices on the $(\bar{\zeta}, \bar{u})$ plane. Between 2 and 4 dimensions, we know that in the $\bar{\zeta} = 0$

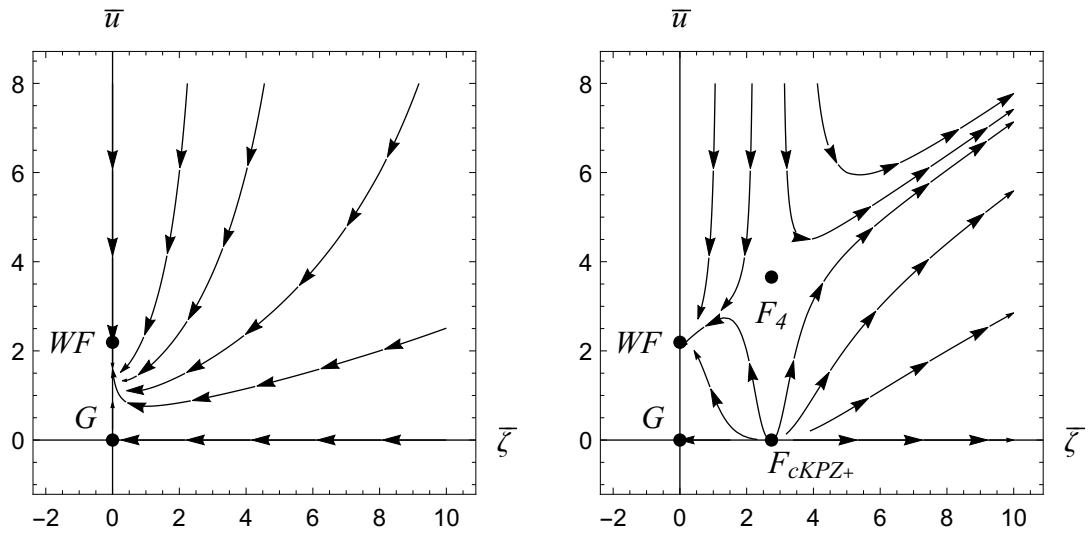

Figure 4.3: Slice of the flow of AMB+ in the $(\bar{\zeta}, \bar{u})$ plane in 3 dimensions, and close to the Wilson-Fisher fixed point, for a value of $\bar{\lambda}$ in the region of Figure 4.2 where any initial set of parameters flows back to the Wilson-Fisher (left), and for a value of $\bar{\lambda}$ in the region of Figure 4.2 where this threshold is present (right). Left and right represent roughly the quadrants of $\bar{\zeta}, \bar{\lambda}$ with different sign and equal sign respectively.

axis, there are two fixed points, the Gaussian and Wilson-Fisher, and we know they are stable in the $\bar{\zeta}$ direction for small enough $\bar{\zeta}$. We also know the flow must take the system to the Wilson-Fisher fixed point if the initial parameters are in the region of Figure 4.2 in which the flow does so for $\bar{\lambda}, \bar{\zeta}$ and $\bar{\nu}$. If we are in the region in which there is a threshold to strong coupling, this threshold should be present in this slice as well. A particular couple of slices in 3 dimensions for both of these cases is in Figure 4.3.

In this slice a new fixed point, that we called F_4, can be seen as the one driving the transition from weak coupling (where the system flows back to the Wilson Fisher), to strong coupling. Another fixed point is observed on the $\bar{u} = 0$ axis. This is related to the cKPZ+ fixed point, since it is obtained by setting all other parameters to 0, but it is not physical in this scenario because $\bar{u}$ cannot be 0 below 4 dimensions.

4.2.2 *Numerical integrations of the flow*

It is important to note that all parameters of the system are flowing in the Figures of the last section, and that the previous images are just slices in which we artificially keep some parameters constant to get an idea of what

the flow is doing, so F_4 is found as a fixed point in these particular slice. It is useful then to numerically confirm the existence of this strong coupling regime. We can do so by numerically integrating the flow for different sets of initial parameters.

The RG flow equations can be solved numerically to find all fixed points. This was done in this section using *Mathematica*. In particular, the fixed points can be found numerically with the function `NSolve` on the flow equations, while trajectories can be integrated numerically with `NDSolve`, which uses a Runge-Kutta method for integrating them numerically.

This section shows two particular numerical integrations of the full RG flow. In the first one, a random value of λ is chosen in 3 dimension, in the region in which the slices of the previous section indicate the presence of a strong coupling regime. Then, with that value of λ as the initial value, the full flow is integrated numerically for different initial values of $\bar{u}$ and $\bar{\zeta}$. This is precisely what is shown in Figure 4.4, in which we find there is a surface (technically complicated to calculate given the complexity of the flow equations) such that at each side of this surface the flow either takes the system back to equilibrium, or flows to infinity, pointing to a possible new phase. We thus obtain paths that take the system to the Wilson-Fisher fixed point or to infinity at each side of the critical surface.

The second integration is done by first finding the particular value of F_4, and choosing initial points close to it, at each side of the critical surface. Again, this integration, shown in Figure 4.5 in the $\bar{\lambda}, \bar{u}$ and $\bar{\zeta}, \bar{u}$ planes, shows the strong coupling regime when the initial conditions are further from the origin than F_4. These integrations should be qualitatively compared to the behaviour obtained from the slices of the flow, for example Figure 4.3.

Some of the fixed points found are likely to be artefacts of the one-loop calculation, while others approach the WF fixed point as $d \to 2^+$. Given the fact that the expansion due to the λ, ζ and ν terms is done as a power series in $d-2$, these are the points that have physical significance. There are two of these points, one we identify with F_4, that behaves in the way described using the projections of the flow, and another one that we call F_{eq}, that satisfies the condition $\zeta = 0, 2\lambda = -\nu$. Notice that this is the equilibrium condition, since this choice of parameters restores detailed balance in the equation of motion, as λ and ζ can be integrated into a term $\phi(\nabla\phi)^2$ in the free energy. This means that the system displays a new equilibrium fixed point not present before. Numerically, it is also found that F_4 is unstable in one direction in parameter space without $\bar{a}$ (describing the critical surface at each side of which the system flows to either equilibrium

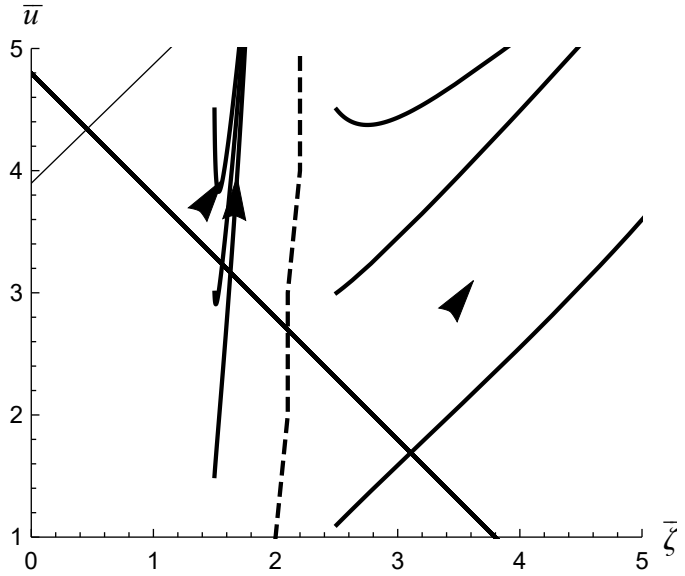

Figure 4.4: Full flow of AMB+ integrated numerically in 3 dimensions, for initial values $\lambda_0 = 3, \nu_0 = 0$, showing the regions where the flow takes the system to the Wilson-Fisher fixed point or into the strong coupling regime. The dashed line represents the threshold, for these initial conditions, that separates the runaway regime from the Wilson-Fisher regime. In the first case we checked that $\bar{\lambda}$ and $\bar{\nu}$ also flow to 0. The flow does not intersect itself, it only appears to do so in this Figure because it is projected on the $(\bar{\zeta}, \bar{u})$ plane.

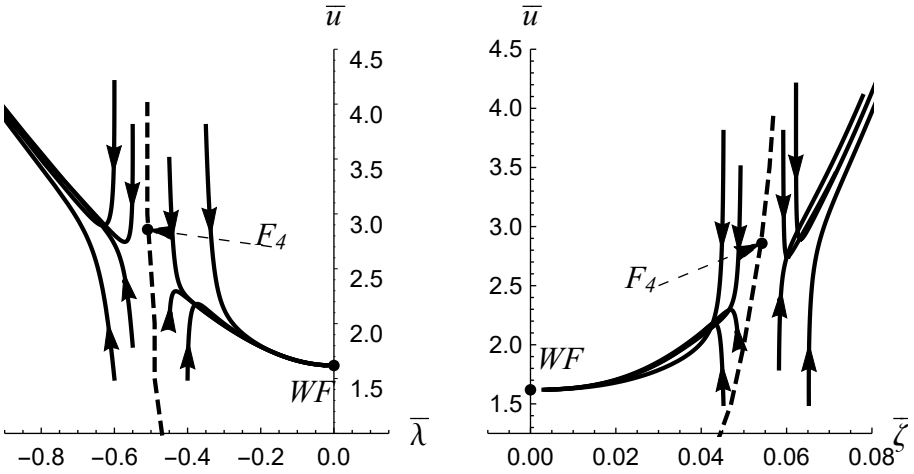

Figure 4.5: Full flow of AMB+ integrated numerically in $d = 2.3$ for initial conditions close to the fixed point F_4. The position of F_4 has been found numerically as explained in the text, as well as the threshold lines (the dashed lines), which have been found for the particular initial conditions used.

or into the strong coupling regime), thus confirming the view indicated by the projections of the flow.

In the full flow, the parameter $\bar{a}$ represented the temperature of the passive Model B. In AMB+, $\bar{a}$ also flows to $\pm\infty$ at each side of of a critical point given by equation 4.8. This means that F_4 is a multicritical point that separates standard phase separation from bubbly phase separation, with the presence of phase separation itself being dictated by the flow of $\bar{a}$, and the nature of phase separation being dictated by at which side of the critical surface of F_4 the system is.

The stability of F_{eq} can be studied numerically, obtaining that it is unstable in one direction. This fixed point could be studied with Model B by adding only one parameter, the correction to the square gradient in the free energy κ_1. Its instability above two dimensions can be intuitively understood as a transition to where the total prefactor of the square gradient, $\kappa + \kappa_1\phi$, becomes negative for some values of the field, making interfaces unstable. This allows for an interpretation in terms of what is known as a Lifshitz fixed point, a type of equilibrium fixed point that drives microphase separation, since a term in the free energy of the form $(\kappa + 2\kappa_1\phi)(\nabla\phi)^2/2$ will produce finite wavelength ordering and microphase separated states if the prefactor becomes negative [57]. Proper study of a system with this kind of instability would require the introduction of higher order gradient terms in the free energy to make the system stable, in the same way we need to introduce the ϕ^4 term if the coefficient of ϕ^2 becomes negative. On the other hand, the nonequilibrium microphase separated states of AMB+ are numerically stable, as shown in [26], so there is no need for higher order terms. This, combined with the fact the flow takes the system away from F_{eq} and into F_4 before going to either Wilson-Fisher or strong coupling, allows us to put F_4 forward as a nonequilibrium equivalent of the Lifshitz fixed point.

One last comment about the nature of this fixed point is due. Typically, when an equilibrium system lies beyond the Lifshitz point, fluctuations make the transition to microphase separation first order, so that it is not properly captured by RG [58, 59]. It is therefore not clear whether the strong coupling regime found here is a signature of a first order transition, and this should be addressed by different methods (for instance a careful numerical study of the order parameter across the transition). Unfortunately, apart from hinting at this new phase, the RG approach cannot rule whether this is a first or second order transition.

This fixed point could then represent an instability that leads to a different kind of microphase separation or mesophase. It would indeed provide a nice connection between the active phase separation of AMB+ and active

systems, and the passive phase separation that an instability in the square gradient of the free energy would produce. Given the qualitative similarities between the active phase and a passive phase separation dictated by a Lifshitz like point, the picture provided by the flow in this Chapter could offer a scenario in which both the active and the passive transitions belong to the same active parameter space, with the equilibrium phase transition being in a special subspace in which an equilibrium condition holds.

A main objective of this study was to see whether an RG calculation could produce the new phases of AMB+ that are found numerically, mainly those that show microphase separation and reverse Ostwald ripening. What we found is that the same kind of thresholds that we found in cKPZ+ exist here, in particular, when looking at the $(\bar{\zeta}, \bar{\lambda})$ plane, this regions of divergence roughly match the regions in which these new phases appear numerically in AMB+.

Going back to the phase diagram obtained numerically, and shown in Figure 1.8, the picture that the RG flow offers is one in which the point F_4 rules the transition between the top and bottom rows of possible phases, and where the $\bar{a}$ parameter would drive all this phases into a uniform phase when crossing its critical point.

As was the case in the last Chapter, given the perturbative nature of these calculations, we cannot answer the question of what this strong coupling regime represents physically or whether it is an artefact of the one-loop calculation or not. However, it is natural to assume this is pointing to microphase separation. The reason is that numerical work done on the system in [26] proves that these nonlinearities create new phases in regions of parameter space that roughly match those we identify with strong coupling. Also, the numerical work in last Chapter helps prove that these term indeed generate new physics at large scales despite their irrelevance in the RG sense. This calculation is then enough to conclude, together with the numerical results of [26], that, even to one-loop, RG captures some of the complexity of AMB+ that is not present in its equilibrium counterpart.

5

ENTROPY PRODUCTION CLOSE TO CRITICALITY

This Chapter takes a different approach to the field theories described so far, and centres the attention on the main observable that quantifies how much a system is breaking time reversibility, the entropy production rate (EPR). This Chapter will review the concept and definition of the entropy production for the types of field theories analysed so far, as well as some of its properties in the case of AMB and AMB+, with the final objective of studying its scaling properties close to the equilibrium (Gaussian and Wilson-Fisher) fixed points.

Notice that our findings in Chapter 4 show that, at and above 2 dimensions, there are values of the nonlinearities that break detailed balance such that the system flows to its equilibrium counterpart (i.e. to the Gaussian or Wilson-Fisher fixed points), so that the system belongs, in that parameter region, to the conserved Ising universality class.

This might lead us to conclude that the critical properties of the system are, effectively, equilibrium. Indeed, the fact that the system flows back to the equilibrium points makes the transition and the states at each side of it resemble the ones of the equilibrium phase separation [18]. However, we will find that the scaling of the EPR indicates the opposite, and that irreversibility is present at all scales close to criticality.

The observable of interest is, more specifically, the noise-averaged, global entropy production rate measured in steady state. It has a standard definition in the field of stochastic thermodynamics [60, 61], which reads as follows for a scalar field ϕ

$$\mathcal{S} = \lim_{\tau\to\infty} \frac{1}{\tau} \left\langle \ln \frac{\mathcal{P}[\phi]}{\mathcal{P}^R[\phi]} \right\rangle , \tag{5.1}$$

where $\mathcal{P}$ is the probability of finding a given path for ϕ in the time interval $(0, \tau)$, and $\mathcal{P}^R$ is the probability of finding the reverse path, and where the average is done over noise realizations. This average is equivalent, assuming ergodicity, to an average over one infinite time trajectory and a single noise realization.

The probability weight of a path can be derived using the standard results of field theory methods for dynamic equations of section 1.2, and is

$$\mathcal{P}[\phi] = \exp(-\mathcal{A}), \tag{5.2}$$

where $\mathcal{A}$ is the dynamical action, that can be either the Onsager-Machlup functional in equation 1.11, or the Martin-Siggia-Rose of equation 1.12. We will use the Onsager-Machlup functional, so that we can write the EPR without the need of an auxiliary field. We can find an expression for the EPR as a function of the field by just substituting the OM functional into the definition of the EPR.

To calculate the reversed path probability, observe that the reversed path must obey $\dot{\phi}^R = -\dot{\phi}$, and since the deterministic part of the dynamics is a functional of the field, it is invariant under time reversal. This means that the noise realization of a path and its reverse must be extremely different to produce reversed dynamics for the same configuration of the field.

It will be useful to write the entropy production for a slightly more general equation of motion than the one we have been using. We are going to assume that the equation of motion may or may not conserve the field ϕ. We can write this general dynamics for a scalar field ϕ as follows

$$\dot{\phi} = -(i\nabla)^c \mu + \eta, \tag{5.3}$$

where μ is a chemical potential, $c = 0$ represents nonconserved dynamics, and $c = 2$ represents conserved dynamics. The variance of the noise η is

$$\langle \eta(r,t)\eta(r',t')\rangle = 2D(i\nabla)^c \delta^{(d)}(r-r')\delta(t-t'). \tag{5.4}$$

We then have the following action and reversed action

$$\begin{aligned} \mathcal{A} &= -\frac{1}{4D}\int d^d r dt \left(\dot{\phi} + (i\nabla)^c\mu\right) \nabla^{-c} \left(\dot{\phi} + (i\nabla)^c\mu\right), \\ \mathcal{A}^R &= -\frac{1}{4D}\int d^d r dt \left(\dot{\phi} - (i\nabla)^c\mu\right) \nabla^{-c} \left(\dot{\phi} - (i\nabla)^c\mu\right), \end{aligned} \tag{5.5}$$

Substituting this into the definition of the EPR, we obtain[1]

$$S = \lim_{\tau\to\infty} \frac{\mathcal{A}^R - \mathcal{A}}{\tau} = -\lim_{\tau\to\infty} \frac{1}{\tau D}\int d^d r dt \mu \dot{\phi}. \tag{5.6}$$

1 There are certain subtleties to be taken into account when calculating the EPR related to whether the stochastic integrals are done as Ito or Stratonovich integrals that become specially important when calculating the EPR numerically, as explained in Appendix C of reference [62]. In this Chapter, it is sufficient to assume the integrals are all Stratonovich.

Notice that if the system is in equilibrium, $\mu = \delta\mathcal{F}/\delta\phi$, then we have

$$\int dt \frac{\delta\mathcal{F}}{\delta\phi}\dot{\phi} = \int dt \dot{\mathcal{F}} = \Delta\mathcal{F}, \tag{5.7}$$

where $\Delta\mathcal{F}$ is the variation of free energy in the time interval of the integral. This would only be nonzero in the initial transient period until the system reaches steady state, and so, in the integral of the entropy production, taken at infinite times in steady state, this contribution vanishes, leaving only the nonequilibrium part of μ:

$$S = \frac{-1}{D}\int d^d r \langle \mu_A \dot{\phi} \rangle, \tag{5.8}$$

where μ_A is that nonequilibrium part. It will be useful to define a local entropy production rate σ such that $S = \int d^d r \sigma$

$$\sigma = \frac{-1}{D}\langle \mu_A \dot{\phi} \rangle. \tag{5.9}$$

It is possible to write down different definitions of the EPR by manipulating derivatives, as explained in [62], and a different one with physical relevance could be obtained by writing the EPR as a function of currents instead of fields. In the rest of this chapter we work with the definition of the EPR that gives the expression of equation 5.9 because it makes our calculations simpler. All definitions are of course equivalent up to contour terms.

5.1 ACTIVE MODEL A

This section introduces a new model that will be useful in this Chapter to illustrate below the concept of stealth entropy production due to its simplicity compared to AMB+.

Active Model A (AMA) is a non-conserved variant of AMB+, built under the same principles. The starting point is Model A [24], defined with equation 5.3, with $c = 0$, and the free energy of Model B:

$$\begin{aligned} \mu =& \frac{\delta\mathcal{F}}{\delta\phi}, \\ \mathcal{F} =& \int d^d r \frac{a}{2}\phi^2 + \frac{u}{4}\phi^4 + \frac{\kappa}{2}(\nabla\phi)^2. \end{aligned} \tag{5.10}$$

To derive a nonequilibrium version that minimally breaks detailed balance, we now introduce terms in the dynamics that cannot be written as the

derivative of a free energy, as a series in gradients and fields. To lowest order, we obtain two terms quadratic in both gradients and fields. The equation of motion of AMA is

$$\dot{\phi} = -a\phi - u\phi^3 + \kappa\nabla^2\phi - \lambda(\nabla\phi)^2 + 2\kappa_1\phi\nabla^2\phi + \eta, \tag{5.11}$$

where η has the variance of equation 5.4 with $c = 0$.

Observe there are two new terms, since with two gradients there is no equivalent of the ζ term of AMB+. The term $\phi\nabla^2\phi$ is part of an equilibrium term, in the same way that ν was, and the equation of motion of AMA can be written as

$$\dot{\phi} = -\mu_E - \mu_A + \eta, \tag{5.12}$$

where μ_E and μ_A are equilibrium and nonequilibrium chemical potentials respectively, with

$$\begin{aligned} \mu_E =& \frac{\delta}{\delta\phi}\int d^d r \frac{a}{2}\phi^2 + \frac{u}{4}\phi^4 + \frac{\kappa + 2\kappa_1\phi}{2}(\nabla\phi)^2, \\ \mu_A =& (\lambda + \kappa_1)(\nabla\phi)^2. \end{aligned} \tag{5.13}$$

The simplicity over AMB+ is obvious from AMA's equation of motion, since now all nonlinearities are of two orders less in gradients. This also means there are fewer nonlinearities, and the nonequilibrium chemical potential consists of only one local term. The particular prefactors are chosen so that a single parameter multiplies each of the nonlinearities in the equation of motion, which means the equilibrium condition is $\lambda + \kappa_1 = 0$.

The EPR of this model will be studied alongside AMB+ in what follows.

5.2 EPR OF AMB+: LOW NOISE EXPANSION

The EPR of Active Model B ($\zeta = \nu = 0$ in equation 4.1) has been studied in detail through numerical simulations and a low noise expansion in [62]. In this section we extend the low-noise calculation (which holds far from criticality) to the case of AMB+. The main results of this latter method is that the EPR has a contribution of order D^0 where there are gradients of the field, for example at the interfaces, and a contribution of order $\sqrt{D}$ in the bulk, produced by the noise. At decreasing noise, then, most of the EPR is concentrated at the gradients. This can be seen, as shown in [62], by expanding the field as a series in $\sqrt{D}$

$$\phi = \phi_0 + \sqrt{D}\phi_1 + D\phi_2 + \mathcal{O}(D^{3/2}), \tag{5.14}$$

and inserting this into equation 5.9. Assuming that the system has reached steady state, so that $\langle\dot{\phi}_1\rangle = 0$, we obtain

$$\sigma = -2\lambda\nabla\phi_0 \cdot \langle\dot{\phi}_1\nabla\phi_1\rangle + \mathcal{O}(\sqrt{D}). \tag{5.15}$$

From this last equation can be deduced that σ is of order D^0 in the places where the deterministic solution ϕ_0 of the steady state has gradients, which happens at the interfaces.

The case of AMB+ is different in that its deterministic current,

$$J_d = -\lambda\nabla\cdot(\nabla\phi)^2 + \zeta\nabla\phi\nabla^2\phi, \tag{5.16}$$

cannot be written as the gradient of a local chemical potential. The chemical potential becomes a non-local function $\mu_A = -\nabla^{-2}J_d$. The inverse Laplacian of the ζ term can be manipulated into a symmetric form

$$\nabla^{-2}\nabla\cdot[\nabla^2\phi\nabla\phi] = \frac{1}{2}(\nabla\phi)^2 + \nabla^{-2}[(\nabla^2\phi)^2 - (\nabla_\alpha\nabla_\beta\phi)^2]. \tag{5.17}$$

The second term can be interpreted as an *electrostatic potential* generated by the charge density

$$Q(r) = (\nabla^2\phi)^2 - (\nabla_\alpha\nabla_\beta\phi)^2, \tag{5.18}$$

which allows us to write the local entropy production as in equation 5.9 with the following nonequilibrium chemical potential

$$\mu_A = \left(\lambda - \frac{\zeta}{2}\right)(\nabla\phi)^2 - \zeta\nabla^{-2}Q(r). \tag{5.19}$$

This way of writing the nonequilibrium chemical potential allows for some insight into the dynamics of bubbles in AMB+, developed in reference [26], only without this charge density interpretation. By assuming spherical symmetry (reasonable given that bubbles tend to be spherical), and rewriting the charge density part, we obtain that in two dimensions

$$\left[(\nabla^2\phi)^2 - (\nabla_\alpha\nabla_\beta\phi)^2\right] = \frac{1}{r}\partial_r(\partial_r\phi)^2. \tag{5.20}$$

This allows to calculate the term as it appears in the equation of motion, $\nabla^{-2}Q(r)$, using Gauss's law. Again, in two dimensions, $\nabla^{-2}Q(r)$ can be interpreted as the potential of the charge density $Q(r)$, which is the same as the potential of a single charge inside a Gauss' surface around which the

electric field is constant (which is a circle in this case). In two dimensions, this can be written as

$$\nabla^{-2}Q(r) = \frac{1}{A_d}\int_0^r Q(y)dy. \tag{5.21}$$

We take as a boundary condition that for a single bubble this potential must vanish at infinity, which allows us to write

$$\nabla^{-2}Q(r) = -\frac{1}{A_d}\int_r^\infty Q(y)dy. \tag{5.22}$$

Finally, this can be rewritten as the term found in [26] representing the jump of the nonequilibrium chemical potential across the interface,

$$\nabla^{-2}Q(r) = -\int_r^\infty \frac{(\partial_y\phi)^2}{y}dy. \tag{5.23}$$

Repeating the low noise expansion of equation 5.15 is an easy exercise that shows the main differences of the EPR between AMB and AMB+. This is done by plugging expansion 5.14 into the equation of motion of AMB+. Doing so, the equilibrium and nonequilibrium parts are as follows

$$\begin{aligned}
\nabla^2\frac{\delta F}{\delta\phi} =&\nabla^2\left(a\phi_0 + u\phi_0^3 - \kappa\nabla^2\phi_0\right)\\
&+\sqrt{D}\nabla^2\left(a\phi_1 + 3u\phi_0^2\phi_1 - \kappa\nabla^2\phi_1\right) + \mathcal{O}(D),\\
\nabla^2\mu_{\text{NE}} =&(\lambda-\zeta/2)\nabla^2(\nabla\phi_0)^2 - \zeta Q_0(r)\\
&+2\sqrt{D}\left[(\lambda-\zeta/2)\nabla^2(\nabla\phi_0\cdot\nabla\phi_1)\right.\\
&\left.-\zeta Q_1(r)\right] + \mathcal{O}(D),
\end{aligned} \tag{5.24}$$

where $Q_0(r)$ is the charge density of the field ϕ_0, and $Q_1(r)$ is the charge density of order $\sqrt{D}$:

$$Q_1(r) = \nabla^2\phi_0\nabla^2\phi_1 - \nabla_{\alpha\beta}\phi_0\nabla_{\alpha\beta}\phi_1. \tag{5.25}$$

The dynamics for each field ϕ_i can be extracted from expanding the action and looking for the terms proportional to each power of D. This expansion gives:

$$\begin{aligned}
\mathcal{A}[\phi] =&\frac{-1}{4D}\int[\dot\phi_0 - \mathcal{F}_0]\nabla^{-2}[\dot\phi_0 - \mathcal{F}_0]d^dr dt\\
&-\frac{1}{2\sqrt{D}}\int[\dot\phi_0 - \mathcal{F}_0]\nabla^{-2}[\dot\phi_1 - \mathcal{F}_1]d^dr dt\\
&-\frac{1}{4}\int[\dot\phi_1 - \mathcal{F}_1]\nabla^{-2}[\dot\phi_1 - \mathcal{F}_1]d^dr dt\\
&+\mathcal{O}(\sqrt{D}),
\end{aligned} \tag{5.26}$$

where we have defined $\mathcal{F}_0$ and $\mathcal{F}_1$ as

$$\begin{aligned}\mathcal{F}_0 =&\nabla^2\left[a\phi_0 + u\phi_0^3 - \kappa\nabla^2\phi_0\right]\\ &+ (\lambda - \zeta/2)\nabla^2(\nabla\phi_0)^2 - \zeta Q_0(r),\\ \mathcal{F}_1 =&\nabla^2\left[a\phi_1 + 3u\phi_0^2\phi_1 - \kappa\nabla^2\phi_1\right]\\ &+ (2\lambda - \zeta)\nabla^2\left(\nabla\phi_0\cdot\nabla\phi_1\right)\\ &- 2\zeta Q_1(r).\end{aligned} \tag{5.27}$$

The first line of equation 5.26 must vanish at vanishing noise strength, giving the zero noise path (the mean field trajectory), which is just $\dot{\phi}_0 = \mathcal{F}_0$. This also means the second line vanishes automatically, and the third line gives the dynamics for ϕ_1

$$\dot{\phi}_1 = \mathcal{F}_1 + \nabla\cdot\Gamma, \tag{5.28}$$

where Γ is a vectorial white Gaussian noise with variance

$$\langle\Lambda_i(r,t)\Lambda_j(r',t')\rangle = 2\delta_{ij}\delta^{(d)}(r-r')\delta(t-t').$$

Now we can substitute this expression for $\dot{\phi}_1$ into the EPR, equation 5.9, assuming that the system has reached a steady state in which ϕ_0 is constant in time, and the system only has fluctuations in the higher order noise terms. Because ϕ is in steady state, $\dot{\phi} = \sqrt{D}\dot{\phi}_1 + \mathcal{O}(D)$, and for the same reason $\langle\dot{\phi}_i\rangle = \delta_t\langle\phi_i\rangle = 0$, so the D^0 term of μ_A will not contribute to the average either. The expression of the EPR to order D^0 is then

$$\begin{aligned}\sigma(r) =& -(2\lambda-\zeta)\left\langle\dot{\phi}_1\nabla\phi_0\cdot\nabla\phi_1\right\rangle\\ &+ 2\zeta\left\langle\dot{\phi}_1\nabla^{-2}Q_1(r)\right\rangle + \mathcal{O}(\sqrt{D}).\end{aligned} \tag{5.29}$$

In the case of a single bubble in two dimensions, as previously discussed in the dynamics of AMB+, this can be rewritten using the Coulombian interpretation of $Q(r)$, using equation 5.23, as follows

$$\begin{aligned}\sigma(r) =& -(2\lambda-\zeta)\partial_r\phi_0\left\langle\dot{\phi}_1\partial_r\phi_1\right\rangle\\ &- 2\zeta\left\langle\dot{\phi}_1\int_r^\infty\frac{1}{y}(\partial_y\phi_0)(\partial_y\phi_1)dy\right\rangle + \mathcal{O}(\sqrt{D}).\end{aligned} \tag{5.30}$$

A first detail to note is that under the change $(\lambda,\zeta)\to(-\lambda,-\zeta)$, the above quantity seems to change sign, which is not possible since entropy production would change sign globally. This means that the correlators must be linear when expanded in low λ,ζ, and so entropy production will

be quadratic in λ, ζ for low values of these parameters. This is also true for Active Model B [62], where the quadratic dependence seems to hold valid for high values of λ as well.

Secondly, we must note as well that there must be interfaces in the system for the D^0 term to contribute. If the system relaxes to a constant profile with fluctuations, $\nabla\phi_0 = 0$, and then we have to choose the $D^{3/2}$ term in μ_A to obtain nonvanishing averages. This means the EPR will be of order D for constant profiles, which is also the case of AMB [62].

The main difference with AMB is that we have a term $\nabla^{-2}Q_1(r)$. The charge density Q_1 vanishes everywhere except at interfaces, however, the inverse Laplacian makes an interface contribute to the EPR at every point of the system. The EPR is then of order D in the case of flat profiles, and of order D^0 in the presence of interfaces.

The particular structure of this nonlocal contribution can be better understood by noticing that the charge density $Q(r)$ of equation 5.18 is related to the Gaussian curvature of the field ϕ. This further reduces the cases in which there is nonlocality in the EPR. For instance, in the case of a single flat interface that separates the system in two equal halves, this nonlocal contribution vanishes, as can be seen from equation 5.18 when derivatives exist only in one direction.

A different insight can be obtained from assuming spherical symmetry in a given interface, as in the case of the bubbles observed in numerics. From equation 5.20 it can be seen that in two dimensions (and the argument in three dimensions is equivalent), the total charge is zero, as it only exists in the interface where there are gradients, and that expression vanishes when integrated in polar coordinates. This means that even though this contribution is inherently nonlocal, in a perfectly symmetric structure, no charge is seen from outside the interface. Indeed, for any point outside the bubble we can draw a Gaussian surface that goes through that point such that the enclosed charge is zero, so that the EPR is still located mostly within the interface, with the caveat that all points in the interface produce entropy at all other points of the interface.

5.3 STEALTH ENTROPY PRODUCTION

In line with the topic of the rest of the thesis, this section will deal with the scaling of the EPR in the critical region. The main result we are going to use here from Chapter 4 is the fact that, above 2 dimensions, the phase transition of AMB+ lies in the Ising universality class, through the flow towards the Gaussian or Wilson-Fisher fixed points for small enough param-

eters. Remember that although this fact came from the RG calculation, it is also a consequence of the active nonlinearities being irrelevant above 2 dimensions.

This must also be true for AMA for small enough values of λ and κ_1, since they are also irrelevant above 2 dimensions. Both systems have, then, equilibrium behaviour at large scales. The question this section tries to answer is whether the fact that activity is irrelevant means that all signs of irreversibility are lost close to the transition.

To answer this question we will compute the RG flow of the steady-state EPR close to the equilibrium fixed points. As far as we know, this is the first RG calculation of its type for EPR in an active model. The Gaussian fixed point is always present in the system and stable above 4 dimensions, whereas the Wilson-Fisher fixed point is present and stable below 4 dimensions.

A first step is to calculate the natural dimension of the EPR, which already gives its RG behaviour close to the Gaussian fixed point, since this point is described by the mean field theory behaviour of the model. This can be done directly from equation 5.9, for both AMA and AMB+, using the already known scalings of D, $\dot{\phi}$ and μ_A. Under a rescaling with a factor b, close to the Gaussian fixed point as done in the previous chapters, these quantities transform as follows

$$\begin{aligned} D &\to b^{z-d-2\chi-c} D = b^0 D, \\ \dot{\phi} &\to b^{z-\chi} \dot{\phi}, \\ \mu_A &\to b^{z-\chi-c}. \end{aligned} \tag{5.31}$$

These scalings come from the basic scalings $r \to b^{-1} r, t \to b^{-z} t$ and $\phi \to b^{-\chi}\phi$. From these, the local EPR scaling dimension can be calculated directly, using that at mean field level $z - 2 = c$, to get

$$\sigma' = b^{d+z}\sigma. \tag{5.32}$$

Notice that an operator (meaning a function of fields) with a positive dimension vanishes when averaged in approach to the fixed point as the critical temperature[2] is taken to 0, so the local EPR, indeed, vanishes as the critical temperature $\mathfrak{t} \to 0$. This is easy to see, for instance, by writing this scaling as a function of the correlation length (which behaves as $\xi \to \xi/b$ under an RG step), or the reduced temperature $\mathfrak{t}$ that drives the transition

2 Notice that the critical temperature here is just the parameter that drives the transition, and not a temperature in the usual sense. It will then be some combination of a with the active parameters.

at $\mathfrak{t} = 0$ (which relates to ξ via the scaling function $\xi \sim \mathfrak{t}^{-\nu}$, for the usual critical exponent ν). Doing so, we can write

$$\sigma \sim \xi^{-(d+z)} \sim \mathfrak{t}^{\nu(d+z)}. \tag{5.33}$$

To understand the meaning of this scaling, it is useful to draw a comparison with the scaling of other, more familiar quantities, like the free energy density f of an equilibrium system. Close to criticality, the singular part of the free energy density of an equilibrium system must scale $f \sim b^d \sim \xi^{-d} \sim \mathfrak{t}^{\nu d}$. This scaling comes from the fact that critical points are found as those points of the free energy parameter space for which the action $\int f[\phi]$ is functionally equal to the rescaled one $\int f'(\phi') = \int f'(\phi)$. Notice that this scaling for the free energy gives the hyperscaling relation that relates the critical exponents ν and α, $\alpha = 2 - d\nu$

$$c_V = \frac{-d^2 f}{d\mathfrak{t}^2} \sim \mathfrak{t}^{-\alpha} \sim \mathfrak{t}^{\nu d - 2}. \tag{5.34}$$

The scaling of the EPR is then similar to that of the free energy density when considering time as well (thus the extra b^z factor), and so the vanishing of the EPR is not enough to say that the system is effectively reversible, in the same way that the free energy has dimension of space^{-1} and vanishes at $\mathfrak{t} \to 0$, but it creates nontrivial behaviour (like the specific heat divergence), due to the fact that the free energy per effective degree of freedom is dimensionless.

We will then define a new quantity, the EPR per spacetime correlation volume (or per effective degree of freedom), ψ, and a critical exponent θ_σ, associated to the behaviour of ψ close to the critical point as a function of the reduced temperature $\mathfrak{t}$, as follows

$$\psi = \xi^{d+z}\sigma \sim \mathfrak{t}^{-\theta_\sigma}, \tag{5.35}$$

and propose that the dynamics of a system is effectively reversible if $\theta_\sigma < 0$, which means that σ should vanish close to criticality faster than its natural dimension indicates, so that the EPR per spacetime correlation volume, ψ, vanishes close to criticality.

Indeed the fact that at mean field level $\theta_\sigma = 0$ is already indicative of the presence of finite entropy production per effective degree of freedom at all length scales. This is quite surprising since the effective large scale behaviour of these models in the region of parameter space where we are considering them to be is governed by the universality class of an equilibrium model (for either AMA or AMB+). Accordingly, we refer to the case of $\theta_\sigma \geq 0$ as *stealth* entropy production.

The scaling above could ideally be captured in a numerical experiment by simulating this system close to the equilibrium fixed points, with small enough activity parameters. The observed EPR should then behave as follows

$$\psi = A(T) + B(T)\mathfrak{t}^{-\theta_\sigma}, \tag{5.36}$$

where T is the temperature, and we have a nonuniversal term $A(T)$ and a universal scaling function $B(T)$. In a finite size system, a finite size scaling can readily be calculated from the scaling above to obtain that, at the critical point,

$$\psi = A(T_c) + L^{\theta_\sigma/\nu}\bar{\psi}(L^{1/\nu}\mathfrak{t}), \tag{5.37}$$

where $\bar{\psi}$ is another scaling function, such that at the critical point ψ diverges with the system size with the dimensions of the correlation length for a positive θ_σ.

Remember that the EPR vanishes exactly in equilibrium ($\mu_A = 0$), as a direct consequence of the definition of entropy production in equation 5.9, so the scaling found here is only applicable in the case in which the EPR is nonzero ($\mu_A \neq 0$), but small enough so that the system lies close to the Gaussian fixed point, in which case the scaling of each quantity will be dictated by this fixed point. This result must then be understood as the scaling behaviour of the EPR close to the Gaussian fixed point, when the nonequilibrium parameters are very small.

The question of whether values $\theta_\sigma \neq 0$ are possible can be answered by calculating the scaling dimension of ψ close to the Wilson-Fisher fixed point. To answer it, first we have to rewrite the expression of the EPR, by taking equation 5.9 and substituting $\dot{\phi}$ with the complete dynamics of each model. This is done and its implications discussed in the next section.

5.3.1 *Stealth EPR in* 3.99 *dimensions [63]*

Notice that if the model is close enough to the Wilson-Fisher fixed point, we can calculate averages directly at the critical point. This is because we will look at scaling behaviours, and if the system is close to this fixed point, the transition will be, at large scales, dictated by it. We will see below how this allow us to calculate RG flows by keeping just the first nonvanishing terms of the *active* nonlinearities, since they flow to 0. The results of this section are reported in [64].

The Wilson-Fisher critical point is the one of the regular Ising-like phase separation, so the model recovers the $\phi \to -\phi$ symmetry. This means that

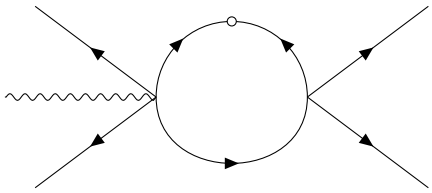

Figure 5.1: One-loop diagram contributing to the coefficients a_i to one loop order (to order ϵ). The wavy line indicates the insertion of a composite operator.

averages of an odd number of fields will vanish. Since μ_A has two fields, terms in the equation of motion of ϕ with an odd number of fields can be ignored, along with the term that multiplies the noise, since when expanded close to the Wilson-Fisher fixed point, it will represent an average of two fields with a symmetric noise, thus three symmetric fields (since the zero-order fields are Gaussian noises). Therefore, close enough to the equilibrium critical points, we can write the following expressions of the local EPR for AMA and AMB+ respectively

$$\begin{aligned}\sigma_{\mathrm{A}} &= \frac{1}{D}\left\langle \mu_A \left(\lambda(\nabla\phi)^2 - 2\kappa_1\phi\nabla^2\phi\right)\right\rangle, \\ \sigma_{\mathrm{B+}} &= \frac{1}{D}\left\langle \mu_A \left[\left(\lambda - \frac{\zeta}{2}\right)\nabla^2(\nabla\phi)^2 + \frac{\nu}{2}\nabla^4\phi^2 - \zeta Q(r)\right]\right\rangle,\end{aligned} \tag{5.38}$$

where the averages are now taken over the stationary measure of the critical equilibrium Models A and B respectively.

To determine the scaling behaviour of these quantities, we must calculate separately the scaling behaviour of the prefactors, and of the composite operators that form part of equations 5.38. Calculating the scaling dimension of these operators close to the Wilson-Fisher fixed point has to be done as explained in Chapter 2.3. This is where the complexity of this step lies, since the operators are of high order in gradients.

If the calculation is done to only one loop, (to order ϵ), then there is only mixing of these operators with the u vertex, and there is only one diagram to calculate, the one of Figure 5.1, as explained in Chapter 2.3.

There is in principle, though, mixing of all operators of the same order of those of the entropy production. In the case of AMB+, these operators have 6 gradients and 4 fields. This means that, in 4 dimensions, they have dimension 10, and it is possible to build 20 independent operators of this order, making the calculation in this case extremely complicated. Therefore it is only done here in the case of AMA, allowing us to find an example of a non-trivial θ_σ.

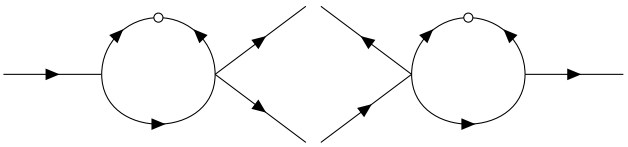

Figure 5.2: One loop diagrams that contribute to λ and κ_1 to order ϵ. Lines are zeroth-order fields and the circle a bare correlator. The three-point vertices carry interactions g_i and the four-point carries u.

In the case of AMA, the operators of the entropy production are of dimension 8 in 4 dimension (4 gradients and 4 fields). For convenience, we will split the local EPR into three terms, such that $\sigma = \sigma_1 + \sigma_2 + \sigma_3$, with

$$\begin{aligned}
\sigma_1 &= D^{-1}\lambda(\lambda+\kappa_1)\langle(\nabla\phi)^4\rangle,\\
\sigma_2 &= -2D^{-1}(\lambda+\kappa_1)^2\langle(\nabla\phi)^2\phi\nabla^2\phi\rangle,\\
\sigma_3 &= 2D^{-1}\lambda(\lambda+\kappa_1)\langle(\nabla\phi)^2\phi\nabla^2\phi\rangle.
\end{aligned} \tag{5.39}$$

Notice that the equilibrium condition for AMA was $\lambda+\kappa_1 = 0$, so that all three terms vanish exactly if this is satisfied, and entropy production is just 0 irrespectively of any scaling we might find.

We have to calculate the RG flow of λ and $\lambda + \kappa_1$, together with the flow of both operators found in the averages of the σ_i's. The flow of λ and $\lambda+\kappa_1$ is quite simple, since we assume that the system lies very close to the Wilson-Fisher fixed point and both of these parameters are irrelevant and therefore small as the fixed point is approached. This means we only need to calculate the ϵ correction to their natural scaling in this regime, which are the diagrams of Figure 5.2 (notice these are diagrams (f) and (g) of Figure 4.1, since with these structure of nonlinearities, only these contribute to the active nonlinearities linearly in λ, κ_1 and linearly in u). This is done in Appendix D to obtain the following intermediate values

$$\begin{aligned}
\lambda_I &= \lambda - \frac{\lambda\epsilon}{3}db,\\
\kappa_{1,I} &= \kappa_1 - \frac{\kappa_1\epsilon}{4}db + \frac{\lambda\epsilon}{12}.
\end{aligned} \tag{5.40}$$

The quantities that the local EPR is written in terms of, λ and $\lambda+\kappa_1$, are the eigenvectors of the flow defined by these last equations close to the Wilson-Fisher fixed point, which can be seen by writing the flow in terms of these two:

$$\begin{aligned}
\frac{d\lambda}{db} &= \left(z+\chi-2-\frac{\epsilon}{3}\right)\lambda,\\
\frac{d(\lambda+\kappa_1)}{db} &= \left(z+\chi-2-\frac{\epsilon}{4}\right)(\lambda+\kappa_1).
\end{aligned} \tag{5.41}$$

Inside the first parenthesis of the flow of each quantity we find the ϵ correction added to the natural scaling dimension $z+\chi-2$. This flow can be written as well in terms of a single RG step with parameter b

$$\begin{aligned} \lambda &\to b^{z+\chi-2-\epsilon/3}\lambda, \\ \lambda+\kappa_1 &\to b^{z+\chi-2-\epsilon/4}(\lambda+\kappa_1). \end{aligned} \tag{5.42}$$

The next step is to calculate the ϵ correction to the scaling of the operators $(\nabla\phi)^4$ and $(\nabla\phi)^2\phi\nabla^2\phi$. Following the field theoretic methods described in Chapter 2.3, we have to find all operators that, when mixed with u to one loop, contribute to the operators of the entropy production to order ϵ. We only need to consider operators of the same order [30], and this means operators with the same number of fields, since when mixed with u to one loop, operators with more or less than 4 fields will not contribute to the operators of the local EPR.

There are seven independent operators made of four gradients and four fields, which are the following, written in real and Fourier space

$$\begin{aligned} A_1 &= \phi^3\nabla^4\phi \to \frac{1}{4}\sum q_i^4, \\ A_2 &= \phi^2\nabla\phi\cdot\nabla(\nabla^2\phi) \to \frac{1}{12}\sum q_i^2 q_i\cdot q_j, \\ A_3 &= \phi^2\nabla^2\phi\nabla^2\phi \to \frac{1}{6}\sum q_i^2 q_j^2, \\ A_4 &= \phi^2(\nabla_\alpha\nabla_\beta\phi)^2 \to \frac{1}{6}\sum (q_i\cdot q_j)^2, \\ A_5 &= \phi\nabla^2\phi(\nabla\phi)^2 \to \frac{1}{12}\sum q_i^2 q_j\cdot q_k, \\ A_6 &= \phi\nabla_\alpha\nabla_\beta\phi\nabla_\alpha\phi\nabla_\beta\phi \to \frac{1}{12}\sum q_i\cdot q_j q_i\cdot q_k, \\ A_7 &= (\nabla\phi)^4 \to \frac{1}{3}\sum q_i\cdot q_j q_k\cdot q_l, \end{aligned} \tag{5.43}$$

where the sums have to be taken over the wavevector indices, with the restriction that different indices cannot take the same value. Notice that the local EPR is made of operators A_5 and A_7.

We have to work with the MSR action of AMA, and add to it these seven operators with an auxiliary field a_i for each of them, $\mathcal{A}\to\mathcal{A}+\int a_i A_i$. The ϵ correction to the intermediate values of each a_i to one loop comes from the diagram of Figure 5.1, which has to be calculated for all seven operators. This diagram will generate a number of intermediate values such that

$$a_{i,I} = a_i + M_{ij}a_j db, \tag{5.44}$$

which gives the RG flow of each field

$$\frac{da_i}{db} = \tilde{d}a_i + M_{ij}a_j, \tag{5.45}$$

where $\tilde{d} = -4 + z$ is the natural dimension of a_i as calculated through dimensional analysis from the MSR action.

Notice that left-eigenvectors of M_{ij}, defined by $v_i^\alpha M_{ij} = \delta^\alpha v_j^\alpha$ (where α indexes different eigenvectors), will flow according to

$$\frac{dv_i^\alpha}{db} = (\tilde{d} + \delta^\alpha)v^\alpha. \tag{5.46}$$

The leading scaling of each operator will then be the scaling of the most relevant eigenoperator into which it is decomposed. The particular M_{ij} matrix we will find will have a complete set of eigenvectors, so that decompositions will exist and be unique for any arbitrary operator.

The calculation of the matrix M_{ij} is quite cumbersome and left to Appendix D. If the operator A_i is chosen for the vertex, then the value of the diagram will be the contribution of a_i to each other a_j, and so will give the row M_{ij}. The calculation is then repeated for each A_i to get all seven rows. Substituting the value of u coming from the second vertex with its value in the Wilson-Fisher fixed point, $u^* = \kappa^2\epsilon\Lambda^{4-d}/(9D\Omega_d)$, we obtain

$$M_{ij} = \frac{\epsilon}{9}\begin{pmatrix} -9 & \frac{3}{2} & 0 & -3 & -\frac{3}{4} & \frac{3}{8} & 0 \\ 0 & -\frac{9}{2} & 0 & -9 & 0 & \frac{3}{2} & -6 \\ 0 & 0 & -3 & 0 & -\frac{3}{4} & -\frac{1}{8} & -1 \\ 0 & 0 & 0 & -12 & 0 & 2 & -5 \\ 0 & 0 & 0 & 1 & -\frac{9}{2} & -\frac{3}{2} & -4 \\ 0 & 0 & 0 & -4 & 0 & -\frac{15}{2} & -2 \\ 0 & 0 & 0 & 0 & 0 & -\frac{3}{4} & -6 \end{pmatrix}. \tag{5.47}$$

It is now an exercise of linear algebra to find the eigenvalues δ^α of this matrix (*Mathematica* was used for this linear algebra calculations)

$$\delta^\alpha = -\epsilon\left(\frac{10}{9}, 1, 1, \frac{13}{18}, \frac{1}{2}, \frac{1}{2}, \frac{1}{3}\right), \tag{5.48}$$

and its left eigenvectors, ordered to correspond to each δ^α

$$\begin{aligned}
v^{(1)} &= (0,0,0,2,0,-1,2),\\
v^{(2)} &= (-54,18,0,-3,-9,0,19),\\
v^{(3)} &= (-84,28,0,-30,-14,19,0),\\
v^{(4)} &= (0,0,0,8,0,-11,36),\\
v^{(5)} &= (0,-11,0,12,-9,0,28),\\
v^{(6)} &= (0,-33,0,36,1,7,0),\\
v^{(7)} &= (0,0,28,-2,-14,1,12).
\end{aligned} \tag{5.49}$$

A simple vector decomposition finds that the vectors corresponding to A_5, $\tilde{A}_5 = (0,0,0,0,1,0,0)$, and to A_7, $\tilde{A}_7 = (0,0,0,0,0,0,1)$, have the following decomposition, where no particular normalization has been chosen

$$\begin{aligned}
\tilde{A}_5 &= \frac{5}{7}v^{(1)} + \frac{-14}{95}v^{(2)} + \frac{9}{95}v^{(3)} + \frac{17}{140}v^{(4)} + \frac{-3}{28}v^{(5)} + \frac{1}{28}v^{(6)},\\
\tilde{A}_7 &= \frac{3}{7}v^{(1)} + \frac{-7}{95}v^{(2)} + \frac{9}{190}v^{(3)} + \frac{3}{70}v^{(4)}.
\end{aligned} \tag{5.50}$$

The most relevant eigenvectors in which A_5 and A_7 are decomposed are then $v^{(6)}$ and $v^{(4)}$ respectively, which have eigenvalues $\delta^{(6)} = -\epsilon/2$ and $\delta^{(4)} = -13\epsilon/18$.

With this, we already have all ingredients needed to calculate the scaling of each σ_i of the local EPR of AMA. Combining these scalings of the operators we just found with the scalings of the prefactors of equation 5.39, we find that

$$\begin{aligned}
\sigma_1 &\to b^{d+z+5\epsilon/36}\sigma_1,\\
\sigma_2 &\to b^{d+z}\sigma_2,\\
\sigma_3 &\to b^{d+z-\epsilon/12}\sigma_3.
\end{aligned} \tag{5.51}$$

Or, written in terms of the local EPR per spacetime correlation volume ψ,

$$\begin{aligned}
\psi_1 &\to b^{5\epsilon/36}\psi_1,\\
\psi_2 &\to b^{0}\psi_2,\\
\psi_3 &\to b^{-\epsilon/12}\psi_3.
\end{aligned} \tag{5.52}$$

Of these three terms, ψ_1 is irrelevant to order ϵ and ψ_2 is marginal (as in the Gaussian fixed point). The leading term close to criticality is then ψ_3,

therefore defining the scaling of ψ, which is the following as a function of the correlation length and reduced temperature

$$\psi \sim \xi^{\epsilon/12} \sim \mathfrak{t}^{-\nu\epsilon/12}, \tag{5.53}$$

and gives an order ϵ value of the critical exponent θ_σ for AMA

$$\theta_\sigma = \frac{\nu\epsilon}{12} + \mathcal{O}(\epsilon^2), \tag{5.54}$$

which is strictly positive below 4 dimensions. The critical local EPR per spacetime correlation volume is thus a diverging quantity as $\mathfrak{t} \to 0$, indicating that entropy is being produced in a cascade of scales close to criticality, even though the critical behaviour lies in the equilibrium, nonconserved Ising universality class.

Although this is a new an interesting result, its interpretations are far from clear, and deserves further study from different points of view. Usually, an anomalous dimension such as a non-zero θ_σ is indicative of a certain fractal structure of that quantity at criticality. This means that entropy production, as mentioned above, is generated at all scales between the short cutoffs and the correlation length and times. The fact that this quantity is intrinsically defined as a function of space and time means it is not clear, however, whether it is created at all time scales, length scales, or both.

Another puzzling feature of this anomalous scaling is that the sign of σ_3 is not clearly set by the model. Since the operator $(\nabla\phi)^2\phi\nabla^2\phi$ is averaged in the equilibrium critical model, it will have a sign defined by the equilibrium critical point. At the same time, the sign of the prefactor, $\lambda(\lambda + \kappa_1)$, is defined by its initial values, since the flow of equation 5.41 keeps its sign constant, so the sign of this prefactor can be chosen from initial conditions. This means that the diverging piece of the local EPR (per spacetime correlation volume, do not forget that the local EPR σ is always vanishing at criticality) might actually be negative.

Since the RG analysis only extracts the critical part of the EPR, this does not mean we are producing a negative EPR, as there may be positive terms that diverge as the short cutoff is taken to zero but with no dependence on $\mathfrak{t}$, and these contributions would be neglected by the RG flow, as explained in Chapter 2. This is comparable to the free energy density f in static equilibrium models, where divergent, $\mathfrak{t}$-independent terms arise but do not contribute to the singular part of the heat capacity. Likewise here, the RG procedure calculates only the singular part of the EPR. However, a negative contribution here would require more study, and there are other examples when a sign reversal of the entropy production are observed when integrating out microscopic degrees of freedom [65].

6

CONCLUSIONS

We have analysed the critical properties of several nonequilibrium systems using Renormalization Group techniques, and some numerical analysis in the case of cKPZ+.

In the case of this latter model, we found that the term making it different from the standard formulations of conserved surface growth (the ζ term), generates a new phase at and above 2 dimensions, that can be captured by a one loop RG calculation. We reasoned that this new term should indeed be there in the coarse grained dynamics of particle level models that are usually used to describe these system.

RG predicts this new phase as a strong coupling regime above the dimension that would be deemed as the critical dimension from naive dimensional analysis. The structure of the nonlinearities make them irrelevant in the RG sense above 2 dimensions, however, the particular structure of the one loop calculation produces an unstable pair of lines of fixed points in the two-dimensional plane of parameters.

At each side of these lines the system either flows back to the linear model (as would be predicted by dimensional analysis above 2 dimensions), or diverges. In 2 dimensions, this pair of lines collapses to straight lines that cross through the origin and the flow becomes marginal. The origin of parameter space becomes then marginally stable in some directions and marginally unstable in others, and this transition to strong coupling comes to depend on the angle at which the system is set in the λ, ζ plane. Since the new phase is predicted in 2 dimensions, unlike in previous models of conserved surface growth like the cKPZ or the Wolf-Villain model, we also performed some numerical simulations to check whether the actual behaviour of cKPZ+ is strongly nonlinear in this new regime, or whether this phase is just an artefact and its behaviour is linear as predicted by dimensional analysis. This numerical work was done using a pseudospectral method to take care of the high gradient terms, and it served to show that this model indeed has a new phase in those regions of parameter space in which the RG flow predicts the strong coupling behaviour. Although a complete analysis of this phase would require an entirely separate project and possibly different methods (like nonperturbative renormalization group and different numerical approaches), it served to show that the strong coupling regime is a feature of

the system and not an artefact, and that as such, strong coupling behaviour can be expected not only of nonconserved surfaces, but also conserved ones.

The next Chapter dealt with the critical properties of AMB+, a model proposed as a continuum description of systems of spherical self-propelled particles. We found that, as in the case of cKPZ+, the one loop RG calculation shows a threshold above which there is a strong coupling regime, that could not be predicted from dimensional analysis. We further confirmed that this threshold roughly matches the one found in its phase diagram as investigated numerically. This model has a new critical fixed point (that we called F_4), that stems from the Wilson-Fisher fixed point above 2 dimensions and dictates the behaviour of the system at the transition between the weak and strong coupling regimes, and that shares similarities to Lifshitz-like fixed points found in equilibrium systems that rule transitions into microphase separated states.

Finally, we studied the scaling properties of the entropy production rate of AMB+ at the Gaussian fixed point, and of its simpler relative AMA at the Wilson-Fisher, finding that there is a new critical exponent θ_σ, that rules whether the scaling of the EPR per spacetime correlation volume vanishes or diverges in approach to the equilibrium critical points. In the particular case of AMA we found that the EPR per spacetime correlation volume surprisingly diverges in approach to the Wilson-Fisher, meaning that, even though the large scale behaviour of the system is that of Model A, if the nonlinear parameters are small enough, there is EPR at macroscopic scales.

This thesis leaves a few questions open which could lead to future work and projects. In the case of cKPZ+, a deeper characterization of the strong coupling phase would be interesting. Although a theoretical study of this phase would have the same difficulties as the same question has regarding the KPZ equation, at least there is a lot of numerical work to be done with cKPZ+. The fact that the strong coupling phase is present in two dimensions, and not strictly above, could make these numerical studies much more approachable. It would be interesting, for instance, to study the relation between mound formation and the nonlinearities of cKPZ+ as described at the end of Chapter 3.

In relation to AMB+, there are still many questions open. Numerically, it would be interested to study the nonequilibrium phase transitions present in the model, although the large number of parameters and fine tuning necessary makes this task very hard. The main result of this thesis that needs further study, however, is the scaling found for the entropy production near the equilibrium fixed points. It could be studied, for instance, how the entropy production behaves, numerically, close to these fixed points. This

would not need as much fine tuning since it has to be done close to the known equilibrium models, with small perturbations of the active nonlinearities. This could probably shed some light of the meaning of having diverging EPR per spacetime correlation volume in systems that lie in equilibrium universality classes. It would also be interesting to find other nonequilibrium models for which this EPR has negative values of θ_σ, since it would allow for some direct comparison between systems that are effectively equilibrium at large scales and systems that, while lying in an equilibrium universality class, have diverging EPR, this comparison could also shed some light on the nature of this diverging EPR.

A

LOOP INTEGRALS

This appendix described the main strategy for calculating the loop integrals in continuous dimensions present throughout this thesis. These integrals are obtained by expanding as Taylor series in the external wavevectors q_i. We have only considered one loop integrals, so there is always only one internal frequency, k.

The first step is always to integrate out the time frequency. This can be done through a standard contour integral, and here are listed all the combinations we find in the loop integrals that are seen in the text. To do so, we will consider integrals of combinations of the following functions, that have the structure of the correlator and propagator

$$\begin{aligned} C_0(A,\Omega) &= \frac{1}{\Omega^2 + A^2}, \\ G_0(A,-\Omega) &= \frac{1}{i\Omega + A}, \end{aligned} \tag{A.1}$$

where A and B are functions of the wavevectors. As a function of these, a list of useful integrals is as follows

$$\begin{aligned} \int_\Omega C_0(A,\Omega)G_0(B,-\Omega) &= \frac{1}{2A(A+B)}, \\ \int_\Omega C_0(A,\Omega)G_0(B,-\Omega)G_0(C,-\Omega) &= \frac{1}{2A(A+B)(A+C)}, \\ \int_\Omega C_0(A,\Omega)G_0(B,-\Omega)G_0(C,\Omega) &= \frac{1}{2A(A+B)(C-A)}. \end{aligned} \tag{A.2}$$

These previous results will then be expanded, along with the vertex functions, as a power series of the external wavevectors. If the external wavevectors do not appear as dot products with the loop wavevector, the integral becomes trivial

$$f(q_i)\int \frac{d^dk}{(2\pi)^d}k^c = f(q_i)\Omega_d \int k^{d-1+c}dk. \tag{A.3}$$

If there are dot products of the external frequencies with the loop frequencies, then the angular integrals have to be done differently. If there is an odd number of external frequencies then, due to the system being isotropic,

the integral will vanish, so we only have to worry about even numbers. If there are two internal frequencies, the integral will be, for instance,

$$\int_k (k \cdot q)^2, \tag{A.4}$$

We can, for example, assume, without loss of generality, that q is in one of the axes z, and q' is in the plane of the z axis with another axis (y). These two choices are just a rotation of space, so do not change the result. In standard spherical coordinates, let's take z to be the first axis and y the second (these match the usual z and y in 3 dimensions). Then the integral is

$$q^2 \int_k k^2 \cos^2\theta, \tag{A.5}$$

and the angular part can be solved by noticing that $\cos\theta$ is the z component of the unit vector in the direction of k, then, due to isotropy, we can sum over all other $d-1$ components

$$\int_{\mathrm{a}} u_z = \int_{\mathrm{a}} \frac{1}{d} \sum_i u_i = \frac{1}{d} \int_{\mathrm{a}} = \frac{\Omega_d}{d}, \tag{A.6}$$

where the a subindex of the integral means we are looking only at the angular part of the integral, and where

$$\Omega_d = \frac{1}{(2\pi)^d} \frac{2\pi^{d/2}}{\Gamma(d/2)} \tag{A.7}$$

is the surface area of a d-dimensional sphere divided by $(2\pi)^d$.

In integrals with more than two frequencies, for instance four, which is the maximum number we find in the calculations here, we are going to find the following kind of object

$$\int_{\mathrm{a}} u_\alpha u_\beta u_\gamma u_\delta = A(\delta_{\alpha\beta}\delta_{\gamma\delta} + \delta_{\alpha\gamma}\delta_{\beta\delta} + \delta_{\alpha\delta}\delta_{\beta\gamma}), \tag{A.8}$$

where the equality can be deduced, again, from the isotropy of the integral. The value of the prefactor A can be calculated by equating indices and summing over all dimensions, analogously to what we did with only two vectors, to obtain that $A = 1/[d(d+1)]$.

This allows to make substitution rules to solve the integrals of Chapter 5, as well as the triangular diagrams of both Chapters 3 and 4. In particular, if we find an integral of two external frequencies q_1 and q_2 with the loop frequency k, the substitution is

$$\int_k k \cdot q_1 k \cdot q_2 \to \frac{\Omega_d}{d} q_1 \cdot q_2 \int dk k^2. \tag{A.9}$$

In the case of four frequencies, we have

$$\int k \cdot q_1 k \cdot q_2 k \cdot q_3 k \cdot q_4 \rightarrow \frac{\Omega_d}{d(d+1)}(q_1 \cdot q_2 q_3 \cdot q_4 + q_1 \cdot q_3 q_2 \cdot q_4 + q_1 \cdot q_4 q_2 \cdot q_3) \int dk k^4. \tag{A.10}$$

The loop integrals in Chapters 3 and 4 are calculated by defining angles between each frequency and then re expressing these angles as components of unit vectors in the direction of each frequency (see for instance Appendix B). The integrals in Chapter 5 are slightly more cumbersome to solve with this method and were calculated with the above substitution rules. Both methods are of course completely equivalent. The first method simplifies some calculations, though, since everything is expressed as products of vectors of an orthogonal basis, which allows to cancel all orthogonal ones before doing any integrals.

B

CKPZ+ TRIANGLE DIAGRAMS

This appendix shows that the couple of triangle diagrams of cKPZ+ cancel each other out, thus not contributing to the renormalization of the couplings λ and ζ. These are diagrams c) and d) of Figure 3.2. The first one is calculated with the following external wavevectors

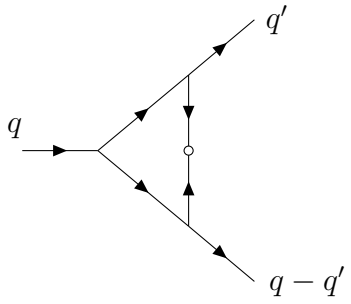

Its value, which we call D_1, is the following integral

$$\begin{aligned} D_1 = \int_{k,\Omega} & g(q, q'+k)g(q'+k, q')g(q-q'-k, -k) \\ & G_0(|q'+k|, \Omega)C_0(k, \Omega) \\ & G_0(|q-q'-k|, -\Omega). \end{aligned} \tag{B.1}$$

The time frequency integral can be calculated with the results of Appendix A, as well as the angular integrals, to obtain

$$\begin{aligned} D_1 = \frac{-1}{2\kappa^3 k^2} [& Dq'(\zeta - 2\lambda)^2 \cos\phi \, (\zeta \cos 2\theta - 2\lambda) \\ & (q' \cos\phi - q\cos\theta)] \, , \end{aligned} \tag{B.2}$$

where the angles are spherical angular coordinates, coming from the angular integrals as described in Appendix A.

The second diagram is calculated following the same procedure. The calculation can be conveniently symmetrized in the external frequencies to get simpler results

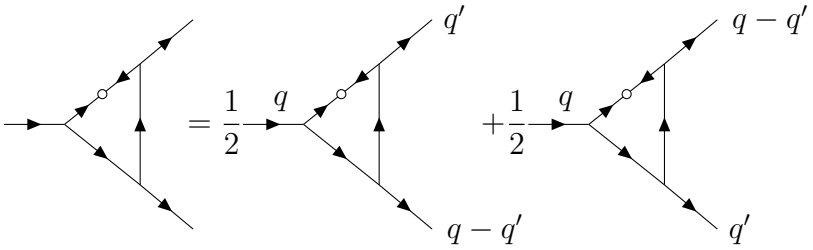

(B.3)

The first diagram of the right hand side represents the integral

$$\begin{aligned} D_2 = \int_{k,\Omega} & g(q,k)g(q-k,q')g(q-q'-k,-k) \\ & C_0(k,\Omega)G_0(q-k,-\Omega) \\ & G_0(q-q'-k,-\Omega). \end{aligned} \tag{B.4}$$

Again, this can be readily calculated with the results of Appendix A, to get the result

$$\begin{aligned} D_2 = \frac{Dq'}{4\kappa^3 k^2} \big[& q'(2\zeta\cos^2\theta - \zeta - 2\lambda)\cos^2\phi(\zeta-2\lambda)^2 \\ & -q(\zeta-2\lambda)^2\cos\phi\cos\theta(2\zeta\cos^2\theta-\zeta-2\lambda)\big]\,. \end{aligned} \tag{B.5}$$

The second term of the right hand side of equation B.3 can be calculated in the same way, and we obtain that it also equals D_2. Doing so it is trivial to check that $D_1 + 2D_2 = 0$.

C

AMB+ DIAGRAMS

This appendix has the explicit calculation of the diagrams of Figure 4.1.

Notice that diagrams (d) and (e) are those of Model B, so they are already calculated in Chapter 2, and diagram (b) vanishes due to conservation of mass, for the same reason that it did in the case of cKPZ+.

Diagrams (a), and (c) are topologically the same as in the cKPZ+ equation, but now the vertex includes ν, so they have to be recalculated. Diagrams (f) and (g) are the corrections to λ, ν and ζ coming from the operator mixing of these nonlinearities with u, while diagrams (i) and (j) are the correction to u coming from the same operator mixing. Diagram (h) is the correction to u coming from the active nonlinearities.

Diagram (a)

Following the diagram rules described in Chapter 2, the diagram reads

$$\begin{aligned} 4G_0(q,\omega)\int_{q,q_I}\frac{1}{2}\Bigg[&2\lambda q_I\cdot(q-q_I)-\zeta\frac{q_I^2 q\cdot(q-q_I)}{q^2}\\ &-\zeta\frac{|q-q_I|^2 q\cdot q_I}{q^2}+\nu q^2\Bigg]\times\\ \frac{1}{2}\Bigg[&-2\lambda q\cdot q_I+\zeta\frac{q^2 q_I\cdot(q-q_I)}{|q-q_I|^2}\\ &-\zeta\frac{q_I^2 q\cdot(q-q_I)}{|q-q_I|^2}+\nu|q-q_I|^2\Bigg]\times\\ &G_0(q-q_I,\omega-\omega_I)C_0(q_I,\omega_I). \end{aligned} \tag{C.1}$$

The time frequency integral is the same found in the case of Model B (see Appendix A for its value), and after doing an expansion for low external wavevector q, we obtain the following integrand

$$\begin{aligned}
&-\frac{D\nu(-\zeta\cos(2\theta)+2\lambda)}{2\kappa^2}+\\
&\frac{qD}{2\kappa^2 q_I}\cos(\theta)(-\zeta\cos(2\theta)(-\zeta+2\lambda+2\nu)\\
&\qquad-\zeta(2\lambda+\nu)+2\lambda(2\lambda+3\nu))+\\
&\frac{q^2D}{2\kappa^2 q_I^2}(-\cos^2(\theta)\left(7\zeta^2-6\zeta\nu+4\lambda^2\right)+2\zeta^2+\\
&\qquad 4\zeta(\zeta-\nu)\cos^4(\theta)-\zeta(\nu-4\lambda)+\nu(\nu-2\lambda))+\mathcal{O}(q^3),
\end{aligned} \tag{C.2}$$

where θ is the angle between q and the loop wavevector q_I.

Observe there are three terms. The middle one, proportional to q (and therefore to $\cos\theta$), vanishes when doing the angular integral, as explained in Chapter 2 and Appendix A, since we can only have even powers of the external wavevector.

The first term is a constant, and therefore contributes to the mass term a. Observe that it is proportional to ν. This must be the case since the ν term breaks the global shift ($\phi \mapsto \phi + c$) symmetry, while the λ and ζ terms have that symmetry and therefore cannot generate a term that breaks it (this is why this constant term was 0 in the case of cKPZ+). The third term is proportional to q^2, so it contributes to κ.

The angular integral can be calculated using the substitution rules of Appendix A. Doing so, we obtain an intermediate contribution to a of the form

$$a_{I,(\mathrm{a})} = \frac{\kappa\bar{\nu}}{2d}\left[(d-2)\bar{\zeta}+2d\bar{\lambda}\right]\Omega_d\Lambda^d db, \tag{C.3}$$

and a contribution to κ of the form

$$\kappa_{I,(\mathrm{a})} = -\kappa M\Omega_d\Lambda^{d-2}db, \tag{C.4}$$

with

$$\begin{aligned}
M =&\frac{1}{2d(d+2)}\Big[d\bar{\zeta}((4-d)\bar{\nu}+4(d+2)\bar{\lambda})\\
&+(d-2)(2d+1)\bar{\zeta}^2-(d+2)\left(2d\bar{\lambda}\nu-d\bar{\nu}^2+4\bar{\lambda}^2\right)\Big].
\end{aligned} \tag{C.5}$$

Diagram (c)

The diagram calculation is the same as in Appendix B, except the vertex includes the ν term as well. This makes it different from zero and it must be analysed separately. The integrals produce an expression that is quadratic in the external wavevectors q and q'. If θ is the angle between them, the expression will have the form

$$f_1 q^2 + f_2 q'^2 + f_3 q q' \cos\theta + f_4 q'^2 \cos^2\theta. \tag{C.6}$$

Notice that the last term is part of the contribution to the ζ term, since $q'^2 \cos^2\theta = (q \cdot q')^2/q^2$.

These terms have to be rearranged into terms of the form of the vertex function, so by manipulating the last equation, we can write it as

$$\begin{aligned} & f_1 q^2 - \frac{1}{2} f_4 \left(q'^2 + q \cdot q' - \frac{(q \cdot q')^2}{q^2} \right) \\ & + \left(f_2 + \frac{1}{2} f_4 \right) q' \cdot (q - q') \\ & + (f_2 + f_3 + f_4) q \cdot q'. \end{aligned} \tag{C.7}$$

This last rearrangement is in the form of the vertex function g of equation 4.4, and we have a consistency condition $f_2 + f_3 + f_4 = 0$, necessary so that the diagram can be completely reabsorbed by all the parameters.

This produces the intermediate values due to diagrams (c,d)

$$\begin{aligned} \nu_{I,(c)} &= \sqrt{\frac{\kappa^3}{D}} T_{\bar{\nu}} \Lambda^{d-2} db, \\ \lambda_{I,(c)} &= \sqrt{\frac{\kappa^3}{D}} T_{\bar{\lambda}} \Lambda^{d-2} db, \\ \zeta_{I,(c)} &= \sqrt{\frac{\kappa^3}{D}} T_{\bar{\zeta}} \Lambda^{d-2} db, \end{aligned} \tag{C.8}$$

where $T_{\bar{\nu}}, T_{\bar{\lambda}}$ and $T_{\bar{\zeta}}$ are those of equation 4.6.

Diagram (f)

Diagram (f) is simpler in the way that the outcoming wavevectors do not run through loop, so the diagram is proportional to q^2, thus being reabsorbed only by ν.

The integral of this diagram is

$$6\int_{q_I} g(q,q_I)C_0(q_I)G_0(q-q_I,\omega-\omega_I). \tag{C.9}$$

And after doing the time frequency integral and expanding to second order we obtain the intermediate value of ν due to diagram (f)

$$\nu_{I,(\mathrm{f})} = \sqrt{\frac{\kappa^3}{D}}\frac{3\bar{u}\left[2(4-d)\bar{\zeta}-(2+d)(4\bar{\lambda}+d\bar{\nu})\right]}{d(d+2)}, \tag{C.10}$$

which gives the quantity B_1 of equation 4.6.

Diagram (g)

Diagram (g) is topologically the same as (f) in terms of outcoming wavevectors, but its result is different, since all external wavevectors run through the loop. It is useful to symmetrize it and calculate it as follows

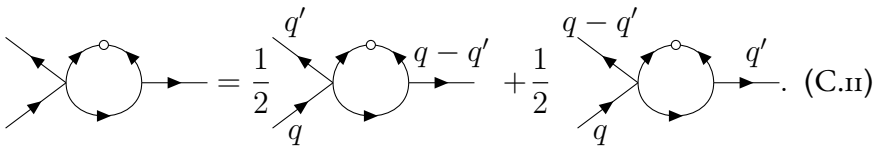

(C.11)

Doing so, we obtain an expression with terms of the form q^2, q'^2 and $q\cdot q'$ (so this diagram does not contribute to ζ). The integral then reads

$$\begin{aligned}6\int_{q_I} &(g(q-q'-q_I,q-q')G_0(q-q'-q_I)+\\ &g(q'-q_I,q')G_0(q'-q_I))C_0(q_I),\end{aligned} \tag{C.12}$$

where the 6 in front comes from the symmetry factor and the $1/2$ of the symmetrization. The result after expanding to second order is

$$\sqrt{\frac{\kappa^3}{D}}\frac{3\bar{u}\left[2(d-1)\bar{\zeta}+(2-d)\bar{\nu}\right]}{d}\Omega_d(q^2+2q'^2-2q\cdot q')db. \tag{C.13}$$

The q^2 term is a contribution to ν, while $q'^2-q\cdot q'$ is a contribution to λ, creating the intermediate values due to diagram (g)

$$\begin{aligned}\nu_{I,(\mathrm{g})} &= \frac{\bar{u}\left[2(d-1)\bar{\zeta}-(d-2)\bar{\nu}\right]}{d},\\ \lambda_{I,(\mathrm{g})} &= -\frac{\bar{u}\left[2(d-1)\bar{\zeta}-(d-2)\bar{\nu}\right]}{d},\end{aligned} \tag{C.14}$$

which give the values of $B_{2,\bar{\nu}}$ and $B_{2,\bar{\lambda}}$ in equation 4.6.

Diagram (h)

Diagram (h) has two contributions depending on where the correlator is located with respect to the incoming wavevector, as follows

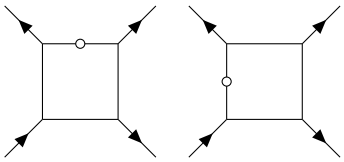

To calculate its contribution to u, we have to look at the q^0 term, making the calculation quite simple, since we can set all external wavevectors to 0. Since the ν part of the vertices only contains the incoming wavevector, this vanishes in the incoming wavevector leg. On the other hand, λ and ζ couple the outcoming wavevectors, so they cancel in the three outcoming legs. This means the diagram has to be $\alpha\lambda\nu^3 + \beta\zeta\nu^3$ for some constants α and β. Since all wavevector dependence of the vertices disappears, the diagram becomes a trivial integral of one correlator and three propagators, and equals the intermediate value of u due to this diagram

$$u_{I,(\mathrm{h})} = \frac{\kappa^2}{D}\left(\bar{\lambda} + \frac{d-2}{2d}\bar{\zeta}\right)\bar{\nu}^3\Omega_d\Lambda^d db, \tag{C.15}$$

from which the value of C_1 in equation 4.6 is deduced.

Diagrams (i) and (j)

These diagrams are also simple to calculate for the same reason that diagram (h) was: we just need the q^0 term that contributes to u, so we can set all external wavevectors to 0. The first diagram has three contributions depending on where the correlator is, as follows

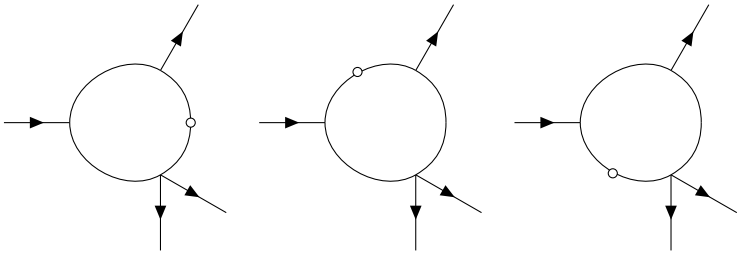

Diagram (j) has the two following contributions depending on where the correlator is

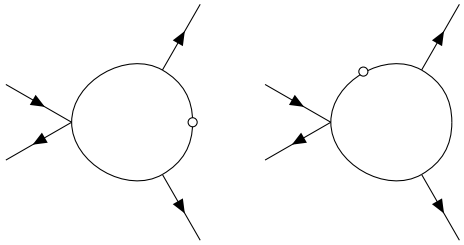

Due to the simplicity of the wavevector expansion, these diagrams can be readily calculated as a simple integral of two propagators and one correlator, giving the result for the intermediate contribution to u due these diagrams

$$u_{I,(\mathrm{h})} = -\frac{\kappa^2}{D}\frac{1}{2}\bar{u}\bar{\nu}\left(12\bar{\lambda} - 9\bar{\nu} + \frac{6(d-2)}{d}\bar{\zeta}\right)\Omega_d\Lambda^{d-2}db, \quad \text{(C.16)}$$

from which the value of C_2 in equation 4.6 is deduced.

D

ENTROPY PRODUCTION RENORMALIZATION MATRIX

This appendix calculates the contributions of the diagrams of Figures 5.1 and 5.2. The ones of the latter are simpler so we do those first, which are topologically the same as diagrams (f) and (g) of Figure 4.1, only with the terms of AMA instead of AMB+.

We begin by writing the equation of motion of AMA:

$$\dot{\phi} = -a\phi - u\phi^3 + \kappa\nabla^2\phi - \lambda(\nabla\phi)^2 + 2\kappa_1\phi\nabla^2\phi + \eta. \tag{D.1}$$

The loop integral will contain the propagator G_0 and correlator C_0 of the linear equation of motion, since we perturb in vanishingly small non-linearities. These are

$$\begin{aligned} G_0(q,\omega) &= \frac{1}{-i\omega + a + \kappa q^2}, \\ C_0(q,\omega) &= \frac{2D}{\omega^2 + (a+\kappa q^2)^2}. \end{aligned} \tag{D.2}$$

The loop integral for the sum of both diagrams can then be written as

$$\begin{aligned} -u\int_{k,\Omega} C_0(k,\Omega)\Big(& g(q,k,q-k)G_0(q-k,-\Omega) \\ &+ \frac{1}{2}g(q'-k,-k,q')G_0(q'-k,-\Omega) \\ &+ \frac{1}{2}g(q-q'-k,-k,q-q')G_0(q-q'-k,-\Omega)\Big), \end{aligned} \tag{D.3}$$

where $g(k_1,k_2,k_3)$ is the vertex function

$$g(k_1,k_2,k_3) = -\kappa_1(k_2^2+k_3^2) + \lambda k_2\cdot k_3, \tag{D.4}$$

that comes from λ and κ_1 terms in the Fourier transform of the equation of motion. The first term of the parenthesis comes from the first diagram, while the remaining two terms in $g(k_1,k_2,k_3)$ come from the second. (Do not confuse the notation g for vertex functions here with the g_i of the main text which are the coupling constants.)

The result of this integral, calculated for the interval of momenta we integrate out $(\Lambda/(1+db),\Lambda)$, and evaluated at zero mass, is

$$\frac{9\bar{u}\kappa_1\Omega_d}{4\Lambda^4}\left(q^2+2q'^2-2q\cdot q'\right)db+\frac{3\bar{u}\lambda\Omega_d}{4\Lambda^4}\left(-q^2+2q'^2-2q\cdot q'\right)db, \tag{D.5}$$

where $\Omega_d = S_d/(2\pi)^d$, with S_d the surface of a d dimensional sphere, and where $\bar{u} = Du\kappa^{-2}$ is the reduced interaction parameter in terms of which we write the flow. The fixed point is found for this parameter as $\bar{u}^* = \epsilon\Lambda^{4-d}/(9\Omega_d)$. The above expression can be rewritten, by manipulating the wavevector terms, as a sum of two terms in the form of the two terms of $g(k_1,k_2,k_3)$, so that we can identify the contributions to λ and κ_1:

$$\frac{3\bar{u}(3\kappa_1-\lambda)\Omega_d}{4\Lambda^4}\left(q'^2+(q-q')^2\right)db-\frac{3\bar{u}\lambda\Omega_d}{\Lambda^4}\left(q'\cdot(q-q')\right)db. \tag{D.6}$$

Integrating over the wavenumber shell gives intermediate values for λ and κ_1. These can be read off the above equation, whose first term contains the Fourier transform of $(\phi\nabla^2\phi)$ and the second that of $(\nabla\phi)^2$. Expanding also to ϵ order (which is a trivial expansion since both terms are proportional to u, whose fixed-point value is $\bar{u}^* = \Lambda^4\epsilon/(9\Omega_d)$) we obtain

$$\begin{aligned}\lambda_I &= \lambda - \frac{\lambda\epsilon}{3}db,\\ \kappa_{1,I} &= \kappa_1 - \frac{\kappa_1\epsilon}{4}db + \frac{\lambda\epsilon}{12}db.\end{aligned} \tag{D.7}$$

Notice that, as usual, the flow does not depend on the cutoff Λ when we work around the Wilson-Fisher fixed point, in the sense that the value of the fixed point itself depends on the cutoff, but not the scaling of operators.

From these intermediate values, the last step is to rescale the equation of motion using the appropriate scaling exponents, as described in the main text, to find the transformation of the parameters. After sending the scale factor $b \to 1+db+O(db^2)$ to obtain differential equations for the flow, we find

$$\begin{aligned}\frac{d\lambda}{db} &= (z+\chi-2)\lambda - \frac{\lambda\epsilon}{3},\\ \frac{d\kappa_1}{db} &= (z+\chi-2)\kappa_1 - \frac{\kappa_1\epsilon}{4} + \frac{\lambda\epsilon}{12},\end{aligned} \tag{D.8}$$

where the terms of order ϵ^0 arise as the differential version of the natural scaling of the couplings, and the terms in ϵ^1 follow directly from the intermediate values given above.

If we now rewrite this flow in terms of λ and $\lambda + \kappa_1$, we obtain the final result, the flow of equation 5.41,

$$\begin{aligned} \frac{d\lambda}{db} &= (z + \chi - 2)\lambda - \frac{\lambda\epsilon}{3}, \\ \frac{d(\lambda + \kappa_1)}{db} &= (z + \chi - 2)(\lambda + \kappa_1) - \frac{\epsilon}{4}(\lambda + \kappa_1). \end{aligned} \tag{D.9}$$

The calculation of the diagram of Figure 5.1 is roughly explained in the main text of Chapter 5 and follows the steps described in [30].

In our case the matrix M_{ij} includes the contribution of the seven independent operators to each of the auxiliary fields a_i. This rather cumbersome to transcribe given the complexity of the diagram, so copied below there is a Mathematica notebook that calculates each diagram and their contributions to each a_i.

The way it works is as follows. First each operator O_i is written in Fourier spaced and symmetrized in each external wavevector q_i. Then some substitution rules $b_{1,2}s \ldots f_{1,2}s$ are defined to take care of the symmetrization of each loop diagram with respect to the four external wavevectors.

The substitution rules ang_i are defined to calculate the angular integrals, and they represent the substitution rules described in Appendix A. In particular, ang_2 takes care of the substitution of equation A.10, and ang_3 takes care of the substitution of equation A.9.

After doing each integral, the results are rewritten as a sum of terms, each of them being of the functional form of each O_j and saved in the matrix terms $M_{i,j}$.

The last few lines calculate the left eigenvectors of the full matrix M_{ij}, and the decomposition of the two vectors of interest for the EPR, which are $(0, 0, 0, 0, 1, 0, 0)$ and $(0, 0, 0, 0, 0, 0, 1)$, in the basis of these eigenvectors.

In[1]:=
```
Clear["Global`*"]
O1 = 1/4 (q1^4 + q2^4 + q3^4 + q4^4); (*ϕ^3 ∇ϕ*)
O2 = 1/12 (q1^2 (q1q2 + q1q3 + q1q4) +
    q2^2 (q1q2 + q2q3 + q2q4) + q3^2 (q1q3 + q2q3 + q3q4) + q4^2 (q1q4 + q2q4 + q3q4));
(*ϕ^2 ∇ϕ . ∇(∇^2 ϕ)*)
O3 = 1/6 (q1^2 q2^2 + q1^2 q3^2 + q1^2 q4^2 + q2^2 q3^2 + q2^2 q4^2 + q3^2 q4^2); (*ϕ^2 ∇^2 ϕ ∇^2 ϕ*)
O4 = 1/6 (q1q2^2 + q1q3^2 + q1q4^2 + q2q3^2 + q2q4^2 + q3q4^2); (*ϕ^2 (∇_α ∇_β ϕ)^2*)
O5 = 1/12 (q1^2 (q2q3 + q2q4 + q3q4) +
    q2^2 (q1q3 + q1q4 + q3q4) + q3^2 (q1q2 + q1q4 + q2q4) + q4^2 (q1q2 + q1q3 + q2q3));
(*ϕ ∇^2 ϕ (∇ϕ)^2*)
O6 = 1/12 (q1q2 q1q3 + q1q2 q1q4 + q1q3 q1q4 + q1q2 q2q3 + q1q2 q2q4 +
    q2q3 q2q4 + q1q3 q2q3 + q1q3 q3q4 + q2q3 q3q4 + q1q4 q2q4 + q1q4 q3q4 + q2q4 q3q4);
(*ϕ (∇_α ∇_β ϕ) ∇_α ϕ ∇_β ϕ*)
O7 = 1/3 (q1q2 q3q4 + q1q3 q2q4 + q1q4 q2q3); (*(∇ϕ)^4*)
A = k^4 κ;
Ba1 = (k^2 + x^2 q1^2 + x^2 q2^2 + x 2 kq1 + x 2 kq2 + x^2 2 q1q2);
Ba2 = (k^2 + x^2 q4^2 + x^2 q3^2 − x 2 kq4 − x 2 kq3 + x^2 2 q3q4);
RCa1 = Ba1 k^2 / (A (A + κ Ba1^2));
RCa2 = Ba2 k^2 / (A (A + κ Ba2^2));
(*Substitution rules*)
b1s = {kq2 → kq3, kq3 → kq2, q1q2 → q1q3,
   q1q3 → q1q2, q2q4 → q3q4, q3q4 → q2q4, q2 → q3, q3 → q2};
b2s = {kq2 → kq3, kq3 → kq2, q1q2 → q1q3, q1q3 → q1q2,
   q2q4 → q3q4, q3q4 → q2q4, q2 → q3, q3 → q2};
c1s = {kq2 → kq4, kq4 → kq2, q1q2 → q1q4, q1q4 → q1q2,
   q2q3 → q3q4, q3q4 → q2q3, q2 → q4, q4 → q2};
```

```
c2s = {kq2 → kq4, kq4 → kq2, q1q2 → q1q4, q1q4 → q1q2,
    q2q3 → q3q4, q3q4 → q2q3, q2 → q4, q4 → q2};
d1s = {kq1 → kq2, kq2 → kq1, q1q3 → q2q3, q2q3 → q1q3,
    q1q4 → q2q4, q2q4 → q1q4, q1 → q2, q2 → q1};
d2s = {kq1 → kq2, kq2 → kq1, q1q3 → q2q3, q2q3 → q1q3,
    q1q4 → q2q4, q2q4 → q1q4, q1 → q2, q2 → q1};
e1s = {kq3 → kq4, kq4 → kq3, q1q3 → q1q4, q1q4 → q1q3,
    q2q3 → q2q4, q2q4 → q2q3, q3 → q4, q4 → q3};
e2s = {kq3 → kq4, kq4 → kq3, q1q3 → q1q4, q1q4 → q1q3,
    q2q3 → q2q4, q2q4 → q2q3, q3 → q4, q4 → q3};
f1s = {kq1 → kq4, kq4 → kq1, q1q2 → q2q4, q2q4 → q1q2,
    q1q3 → q3q4, q3q4 → q1q3, q1 → q4, q4 → q1};
f2s = {kq1 → kq4, kq4 → kq1, q1q2 → q2q4, q2q4 → q1q2,
    q1q3 → q3q4, q3q4 → q1q3, q1 → q4, q4 → q1};
ang1 = {kq1 → kq1, kq2 → kq2, kq3 → kq3, kq4 → kq4};
ang2 = {kq_p_^4 → k^4 q_p^4 3/(d (d + 2)), kq_p_^3 kq_r_ → k^4 q_p^2 Dot[q_p, q_r] 3/(d (d + 2)),
  kq_p_^2 kq_r_^2 → k^4 (q_p^2 q_r^2 + 2 Dot[q_p, q_r]^2) 1/(d (d + 2)),
  kq_p_^2 kq_r_ kq_s_ → k^4 (q_p^2 Dot[q_r, q_s] + 2 Dot[q_p, q_r] × Dot[q_p, q_s]) 1/(d (d + 2)), kq_p_ kq_r_ kq_s_ kq_t_ →
   k^4 (Dot[q_p, q_t] × Dot[q_r, q_s] + Dot[q_p, q_r] × Dot[q_t, q_s] + Dot[q_p, q_s] × Dot[q_t, q_r]) 1/(d (d + 2))};
(*Angular integrals of quartic terms*)
ang3 = {kq_p_^2 → k^2 q_p^2 1/d, kq_r_ kq_s_ → k^2 Dot[q_r, q_s] 1/d};
(*Angular integrals of square terms*)
ang4 = {Dot[q_1, q_2] → q1q2, Dot[q_2, q_1] → q1q2, Dot[q_1, q_3] → q1q3,
  Dot[q_3, q_1] → q1q3, Dot[q_1, q_4] → q1q4, Dot[q_4, q_1] → q1q4, Dot[q_2, q_3] → q2q3,
  Dot[q_3, q_2] → q2q3, Dot[q_2, q_4] → q2q4, Dot[q_4, q_2] → q2q4,
  Dot[q_3, q_4] → q3q4, Dot[q_4, q_3] → q3q4}; (*Back to original notation*)
ang5 = {q_1 → q1, q_2 → q2, q_3 → q3, q_4 → q4}; (*Back to original notation*)
(*Contributions fromA_1*)
a1 = -1/4 (x^4 q1^4 + k^4 + x^4 q2^4 + (k^2 + x^2 q1^2 + x^2 q2^2 + 2 x kq1 + 2 x kq2 + 2 x^2 q1q2)^2) RCa1;
a2 = -1/4 (x^4 q1^4 + k^4 + x^4 q2^4 + (k^2 + x^2 q3^2 + x^2 q4^2 - 2 x kq3 - 2 x kq4 + 2 x^2 q3q4)^2) RCa2;
```

```
b1 = a1 /. b1s;
b2 = a2 /. b2s;
c1 = a1 /. c1s;
c2 = a2 /. c2s;
d1 = b1 /. d1s;
d2 = b2 /. d2s;
e1 = d1 /. e1s;
e2 = d2 /. e2s;
f1 = b1 /. f1s;
f2 = b2 /. f2s;
Fdiag = 36/12 1/Factorial[4]
D[Normal[Series[a1 + a2 + b1 + b2 + c1 + c2 + d1 + d2 + e1 + e2 + f1 + f2, {x, 0, 6}]], {x, 4}] /.
 x → 0; (* 36/12 is the symmetry factor over the
 12 different combinations a1,a2,b1,etc*)
ToMan = Expand[Fdiag /. ang1];
ToMan2 = ToMan /. ang2;
ToMan3 = ToMan2 /. ang3;
ToMan4 = ToMan3 /. ang4;
ToMan5 = Expand[ToMan4 /. ang5] /. d → 4;
SS = Sum[M1,i Oi, {i, 1, 7}];
SSS = k^4 κ^2 ToMan5;
Sols1 = Solve[{D[SS, {q1, 4}] == D[SSS, {q1, 4}],
    D[SS, {q1, 2}, {q1q2, 1}] == D[SSS, {q1, 2}, {q1q2, 1}],
    D[SS, {q1q2, 2}] == D[SSS, {q1q2, 2}],
    D[SS, {q1q2, 1}, {q1q3, 1}] == D[SSS, {q1q2, 1}, {q1q3, 1}],
    D[SS, {q1, 2}, {q2q3, 1}] == D[SSS, {q1, 2}, {q2q3, 1}],
    D[SS, {q1, 2}, {q2, 2}] == D[SSS, {q1, 2}, {q2, 2}],
    D[SS, {q1q2, 1}, {q3q4, 1}] == D[SSS, {q1q2, 1}, {q3q4, 1}]},
   {M1,1, M1,2, M1,3, M1,4, M1,5, M1,6, M1,7}];
Expand[SSS - SS /. {Sols1[[1]]}];
(*Last line checks for symmetry, if it is diff from 0,
the diagram is not properly symmetrized*)
(*Contributions fromA2*)
a1 = -1/12 (x^2 q1^2 (x kq1 + x^2 q1q2 + (-x kq1 - x^2 q1^2 - x^2 q1q2)) +
    x^2 q2^2 (x kq2 + x^2 q1q2 + (-x kq2 - x^2 q1q2 - x^2 q2^2)) +
    k^2 (x kq1 + x kq2 + (-k^2 - x kq1 - x kq2)) + (k^2 + x^2 q1^2 + x^2 q2^2 + 2 x kq1 + 2 x kq2 + 2 x^2 q1q2)
     (-x kq1 - x^2 q1^2 - x^2 q1q2 - x kq2 - x^2 q1q2 - x^2 q2^2 - k^2 - x kq1 - x kq2)) RCa1;
```

```
a2 = -1/12 (x^2 q1^2 (x kq1 + x^2 q1q2 + (-x kq1 + x^2 q1q3 + x^2 q1q4)) +
      x^2 q2^2 (x kq2 + x^2 q1q2 + (-x kq2 + x^2 q2q3 + x^2 q2q4)) +
      k^2 (x kq1 + x kq2 + (-k^2 + x kq3 + x kq4)) + (k^2 + x^2 q3^2 + x^2 q4^2 - 2 x kq3 - 2 x kq4 + 2 x^2 q3q4)
       (-x kq1 + x^2 q1q3 + x^2 q1q4 - x kq2 + x^2 q2q3 + x^2 q2q4 - k^2 + x kq3 + x kq4)) RCa2;
b1 = a1 /. b1s;
b2 = a2 /. b2s;
c1 = a1 /. c1s;
c2 = a2 /. c2s;
d1 = b1 /. d1s;
d2 = b2 /. d2s;
e1 = d1 /. e1s;
e2 = d2 /. e2s;
f1 = b1 /. f1s;
f2 = b2 /. f2s;
Fdiag = 36/12 1/Factorial[4] D[Normal[
       Series[a1 + a2 + b1 + b2 + c1 + c2 + d1 + d2 + e1 + e2 + f1 + f2, {x, 0, 6}]], {x, 4}] /. x → 0;
ToMan = Expand[Fdiag /. ang1];
ToMan2 = ToMan /. ang2;
ToMan3 = ToMan2 /. ang3;
ToMan4 = ToMan3 /. ang4;
ToMan5 = Expand[ToMan4 /. ang5] /. d → 4;
SS = Sum[M2,i Oi, {i, 1, 7}];
SSS = k^4 κ^2 ToMan5;
Sols2 = Solve[{D[SS, {q1, 4}] == D[SSS, {q1, 4}],
    D[SS, {q1, 2}, {q1q2, 1}] == D[SSS, {q1, 2}, {q1q2, 1}],
    D[SS, {q1q2, 2}] == D[SSS, {q1q2, 2}],
    D[SS, {q1q2, 1}, {q1q3, 1}] == D[SSS, {q1q2, 1}, {q1q3, 1}],
    D[SS, {q1, 2}, {q2q3, 1}] == D[SSS, {q1, 2}, {q2q3, 1}],
    D[SS, {q1, 2}, {q2, 2}] == D[SSS, {q1, 2}, {q2, 2}],
    D[SS, {q1q2, 1}, {q3q4, 1}] == D[SSS, {q1q2, 1}, {q3q4, 1}]},
   {M2,1, M2,2, M2,3, M2,4, M2,5, M2,6, M2,7}];
Expand[SSS - SS /. {Sols2[[1]]}];
(*Contributions fromA3*)
a1 = -1/6 (x^2 q1^2 k^2 + x^4 q1^2 q2^2 + x^2 q1^2 (k^2 + x^2 q1^2 + x^2 q2^2 + 2 x kq1 + 2 x kq2 + 2 x^2 q1q2) +
      x^2 k^2 q2^2 + k^2 (k^2 + x^2 q1^2 + x^2 q2^2 + 2 x kq1 + 2 x kq2 + 2 x^2 q1q2) +
      x^2 q2^2 (k^2 + x^2 q1^2 + x^2 q2^2 + 2 x kq1 + 2 x kq2 + 2 x^2 q1q2)) RCa1;
```

```
a2 = -1/6 (x^2 q1^2 k^2 + x^4 q1^2 q2^2 + x^2 q1^2 (k^2 + x^2 q3^2 + x^2 q4^2 - 2 x kq3 - 2 x kq4 + 2 x^2 q3q4) +
      x^2 k^2 q2^2 + k^2 (k^2 + x^2 q3^2 + x^2 q4^2 - 2 x kq3 - 2 x kq4 + 2 x^2 q3q4) +
      x^2 q2^2 (k^2 + x^2 q3^2 + x^2 q4^2 - 2 x kq3 - 2 x kq4 + 2 x^2 q3q4)) RCa2;
b1 = a1 /. b1s;
b2 = a2 /. b2s;
c1 = a1 /. c1s;
c2 = a2 /. c2s;
d1 = b1 /. d1s;
d2 = b2 /. d2s;
e1 = d1 /. e1s;
e2 = d2 /. e2s;
f1 = b1 /. f1s;
f2 = b2 /. f2s;
Fdiag = 36/12 1/Factorial[4] D[Normal[
       Series[a1 + a2 + b1 + b2 + c1 + c2 + d1 + d2 + e1 + e2 + f1 + f2, {x, 0, 6}]], {x, 4}] /. x → 0;
ToMan = Expand[Fdiag /. ang1];
ToMan2 = ToMan /. ang2;
ToMan3 = ToMan2 /. ang3;
ToMan4 = ToMan3 /. ang4;
ToMan5 = Expand[ToMan4 /. ang5] /. d → 4;
SS = Sum[M3,i Oi, {i, 1, 7}];
SSS = k^4 κ^2 ToMan5;
Sols3 = Solve[{D[SS, {q1, 4}] == D[SSS, {q1, 4}],
    D[SS, {q1, 2}, {q1q2, 1}] == D[SSS, {q1, 2}, {q1q2, 1}],
    D[SS, {q1q2, 2}] == D[SSS, {q1q2, 2}],
    D[SS, {q1q2, 1}, {q1q3, 1}] == D[SSS, {q1q2, 1}, {q1q3, 1}],
    D[SS, {q1, 2}, {q2q3, 1}] == D[SSS, {q1, 2}, {q2q3, 1}],
    D[SS, {q1, 2}, {q2, 2}] == D[SSS, {q1, 2}, {q2, 2}],
    D[SS, {q1q2, 1}, {q3q4, 1}] == D[SSS, {q1q2, 1}, {q3q4, 1}]},
   {M3,1, M3,2, M3,3, M3,4, M3,5, M3,6, M3,7}];
Expand[SSS - SS /. {Sols3[[1]]}];
(*Contributions fromA4*)
a1 = -1/6 (x^4 q1q2^2 + x^2 kq1^2 + (-x kq1 - x^2 q1^2 - x^2 q1q2)^2 +
      x^2 kq2^2 + (-k^2 - x kq1 - x kq2)^2 + (-x kq2 - x^2 q1q2 - x^2 q2^2)^2) RCa1;
a2 = -1/6 (x^4 q1q2^2 + x^2 kq1^2 + (-x kq1 + x^2 q1q3 + x^2 q1q4)^2 + x^2 kq2^2 +
```

```
      (-k^2 + x kq3 + x kq4)^2 + (-x kq2 + x^2 q2q3 + x^2 q2q4)^2) RCa2;
b1 = a1 /. b1s;
b2 = a2 /. b2s;
c1 = a1 /. c1s;
c2 = a2 /. c2s;
d1 = b1 /. d1s;
d2 = b2 /. d2s;
e1 = d1 /. e1s;
e2 = d2 /. e2s;
f1 = b1 /. f1s;
f2 = b2 /. f2s;
Fdiag = 36/12 1/Factorial[4] D[Normal[
      Series[a1 + a2 + b1 + b2 + c1 + c2 + d1 + d2 + e1 + e2 + f1 + f2, {x, 0, 6}]], {x, 4}] /. x → 0;
ToMan = Expand[Fdiag /. ang1];
ToMan2 = ToMan /. ang2;
ToMan3 = ToMan2 /. ang3;
ToMan4 = ToMan3 /. ang4;
ToMan5 = Expand[ToMan4 /. ang5] /. d → 4;
SS = Sum[M_{4,i} O_i, {i, 1, 7}];
SSS = k^4 κ^2 ToMan5;
Sols4 = Solve[{D[SS, {q1, 4}] == D[SSS, {q1, 4}],
    D[SS, {q1, 2}, {q1q2, 1}] == D[SSS, {q1, 2}, {q1q2, 1}],
    D[SS, {q1q2, 2}] == D[SSS, {q1q2, 2}],
    D[SS, {q1q2, 1}, {q1q3, 1}] == D[SSS, {q1q2, 1}, {q1q3, 1}],
    D[SS, {q1, 2}, {q2q3, 1}] == D[SSS, {q1, 2}, {q2q3, 1}],
    D[SS, {q1, 2}, {q2, 2}] == D[SSS, {q1, 2}, {q2, 2}],
    D[SS, {q1q2, 1}, {q3q4, 1}] == D[SSS, {q1q2, 1}, {q3q4, 1}]},
   {M_{4,1}, M_{4,2}, M_{4,3}, M_{4,4}, M_{4,5}, M_{4,6}, M_{4,7}}];
Expand[SSS - SS /. {Sols4[[1]]}];
(*Contributions fromA_5*)
a1 = -1/12 (x^2 q1^2 (x kq2 - k^2 - x kq1 - x kq2 - x kq2 - x^2 q1q2 - x^2 q2^2) +
    x^2 q2^2 (x kq1 - k^2 - x kq1 - x kq2 - x kq1 - x^2 q1^2 - x^2 q1q2) +
    k^2 (x^2 q1q2 - x kq1 - x^2 q1^2 - x^2 q1q2 - x kq2 - x^2 q1q2 - x^2 q2^2) +
    (k^2 + x^2 q1^2 + x^2 q2^2 + 2 x kq1 + 2 x kq2 + 2 x^2 q1q2) (x kq1 + x kq2 + x^2 q1q2)) RCa1;
a2 = -1/12 (x^2 q1^2 (x kq2 - k^2 + x kq3 + x kq4 - x kq2 + x^2 q2q3 + x^2 q2q4) +
    x^2 q2^2 (x kq1 - k^2 + x kq3 + x kq4 - x kq1 + x^2 q1q3 + x^2 q1q4) +
```

```
      k^2 (x^2 q1q2 - x kq1 + x^2 q1q3 + x^2 q1q4 - x kq2 + x^2 q2q3 + x^2 q2q4) +
      (k^2 + x^2 q3^2 + x^2 q4^2 - 2 x kq3 - 2 x kq4 + 2 x^2 q3q4) (x kq1 + x kq2 + x^2 q1q2)) RCa2;
b1 = a1 /. b1s;
b2 = a2 /. b2s;
c1 = a1 /. c1s;
c2 = a2 /. c2s;
d1 = b1 /. d1s;
d2 = b2 /. d2s;
e1 = d1 /. e1s;
e2 = d2 /. e2s;
f1 = b1 /. f1s;
f2 = b2 /. f2s;
Fdiag = 36/12 1/Factorial[4] D[Normal[
       Series[a1 + a2 + b1 + b2 + c1 + c2 + d1 + d2 + e1 + e2 + f1 + f2, {x, 0, 6}]], {x, 4}] /. x → 0;
ToMan = Expand[Fdiag /. ang1];
ToMan2 = ToMan /. ang2;
ToMan3 = ToMan2 /. ang3;
ToMan4 = ToMan3 /. ang4;
ToMan5 = Expand[ToMan4 /. ang5] /. d → 4;
SS = Sum[M5,i Oi, {i, 1, 7}];
SSS = k^4 κ^2 ToMan5;
Sols5 = Solve[{D[SS, {q1, 4}] == D[SSS, {q1, 4}],
    D[SS, {q1, 2}, {q1q2, 1}] == D[SSS, {q1, 2}, {q1q2, 1}],
    D[SS, {q1q2, 2}] == D[SSS, {q1q2, 2}],
    D[SS, {q1q2, 1}, {q1q3, 1}] == D[SSS, {q1q2, 1}, {q1q3, 1}],
    D[SS, {q1, 2}, {q2q3, 1}] == D[SSS, {q1, 2}, {q2q3, 1}],
    D[SS, {q1, 2}, {q2, 2}] == D[SSS, {q1, 2}, {q2, 2}],
    D[SS, {q1q2, 1}, {q3q4, 1}] == D[SSS, {q1q2, 1}, {q3q4, 1}]},
   {M5,1, M5,2, M5,3, M5,4, M5,5, M5,6, M5,7}];
Expand[SSS - SS /. {Sols5[[1]]}];
(*Contributions fromA6*)
a1 = -1/12 (x^3 kq1 q1q2 + x kq1 (-x kq1 - x^2 q1^2 - x^2 q1q2) + x^2 q1q2 (-x kq1 - x^2 q1^2 - x^2 q1q2) +
      x^2 kq1 kq2 + x kq2 (-k^2 - x kq1 - x kq2) + x kq1 (-k^2 - x kq1 - x kq2) + x^3 q1q2 kq2 +
      x kq2 (-x kq2 - x^2 q1q2 - x^2 q2^2) + x^2 q1q2 (-x kq2 - x^2 q1q2 - x^2 q2^2) +
      (-k^2 - x kq1 - x kq2) (-x kq2 - x^2 q1q2 - x^2 q2^2) + (-x kq1 - x^2 q1^2 - x^2 q1q2) (-k^2 - x kq1 - x kq2) +
      (-x kq2 - x^2 q2^2 - x^2 q1q2) (-x kq1 - x^2 q1^2 - x^2 q1q2)) RCa1;
a2 = -1/12 (x^3 kq1 q1q2 + x kq1 (-x kq1 + x^2 q1q3 + x^2 q1q4) + x^2 q1q2 (-x kq1 + x^2 q1q3 + x^2 q1q4) +
```

```
      x^2 kq1 kq2 + x kq2 (-k^2 + x kq3 + x kq4) + x kq1 (-k^2 + x kq3 + x kq4) + x^3 q1q2 kq2 +
      x kq2 (-x kq2 + x^2 q2q3 + x^2 q2q4) + x^2 q1q2 (-x kq2 + x^2 q2q3 + x^2 q2q4) +
      (-k^2 + x kq3 + x kq4) (-x kq2 + x^2 q2q3 + x^2 q2q4) + (-x kq1 + x^2 q1q3 + x^2 q1q4)
       (-k^2 + x kq3 + x kq4) + (-x kq2 + x^2 q2q3 + x^2 q2q4) (-x kq1 + x^2 q1q3 + x^2 q1q4)) RCa2;
b1 = a1 /. b1s;
b2 = a2 /. b2s;
c1 = a1 /. c1s;
c2 = a2 /. c2s;
d1 = b1 /. d1s;
d2 = b2 /. d2s;
e1 = d1 /. e1s;
e2 = d2 /. e2s;
f1 = b1 /. f1s;
f2 = b2 /. f2s;
Fdiag = 36/(12 Factorial[4]) 1/(Series[a1 + a2 + b1 + b2 + c1 + c2 + d1 + d2 + e1 + e2 + f1 + f2, {x, 0, 6}]], {x, 4}] /. x → 0;
ToMan = Expand[Fdiag /. ang1];
ToMan2 = ToMan /. ang2;
ToMan3 = ToMan2 /. ang3;
ToMan4 = ToMan3 /. ang4;
ToMan5 = Expand[ToMan4 /. ang5] /. d → 4;
SS = Sum[M_{6,i} O_i, {i, 1, 7}];
SSS = k^4 κ^2 ToMan5;
Sols6 = Solve[{D[SS, {q1, 4}] == D[SSS, {q1, 4}],
    D[SS, {q1, 2}, {q1q2, 1}] == D[SSS, {q1, 2}, {q1q2, 1}],
    D[SS, {q1q2, 2}] == D[SSS, {q1q2, 2}],
    D[SS, {q1q2, 1}, {q1q3, 1}] == D[SSS, {q1q2, 1}, {q1q3, 1}],
    D[SS, {q1, 2}, {q2q3, 1}] == D[SSS, {q1, 2}, {q2q3, 1}],
    D[SS, {q1, 2}, {q2, 2}] == D[SSS, {q1, 2}, {q2, 2}],
    D[SS, {q1q2, 1}, {q3q4, 1}] == D[SSS, {q1q2, 1}, {q3q4, 1}]},
   {M_{6,1}, M_{6,2}, M_{6,3}, M_{6,4}, M_{6,5}, M_{6,6}, M_{6,7}}];
Expand[SSS - SS /. {Sols6[[1]]}];
(*Contributions fromA_7*)
a1 = -1/3 (x kq1 (-x kq2 - x^2 q1q2 - x^2 q2^2) +
      x^2 q1q2 (-k^2 - x kq1 - x kq2) + x kq2 (-x kq1 - x^2 q1^2 - x^2 q1q2)) RCa1;
a2 = -1/3 (x kq1 (-x kq2 + x^2 q2q3 + x^2 q2q4) + x^2 q1q2 (-k^2 + x kq3 + x kq4) +
```

```
      x kq2 (-x kq1 - x^2 q1q3 - x^2 q1q4)) RCa2;
b1 = a1 /. b1s;
b2 = a2 /. b2s;
c1 = a1 /. c1s;
c2 = a2 /. c2s;
d1 = b1 /. d1s;
d2 = b2 /. d2s;
e1 = d1 /. e1s;
e2 = d2 /. e2s;
f1 = b1 /. f1s;
f2 = b2 /. f2s;
Fdiag = 36/12 1/Factorial[4]
   D[Normal[Series[a1 + a2 + b1 + b2 + c1 + c2 + d1 + d2 + e1 + e2 + f1 + f2, {x, 0, 6}]], {x, 4}] /.
  x → 0; (*The 3 is 36/12, 36 symm factor and 12 because we sum 12 terms for symm.*)
ToMan = Expand[Fdiag /. ang1];
ToMan2 = ToMan /. ang2;
ToMan3 = ToMan2 /. ang3;
ToMan4 = ToMan3 /. ang4;
ToMan5 = Expand[ToMan4 /. ang5] /. d → 4;
SS = Sum[M7,i Oi, {i, 1, 7}];
SSS = k^4 κ^2 ToMan5;
Sols7 = Solve[{D[SS, {q1, 4}] == D[SSS, {q1, 4}],
    D[SS, {q1, 2}, {q1q2, 1}] == D[SSS, {q1, 2}, {q1q2, 1}],
    D[SS, {q1q2, 2}] == D[SSS, {q1q2, 2}],
    D[SS, {q1q2, 1}, {q1q3, 1}] == D[SSS, {q1q2, 1}, {q1q3, 1}],
    D[SS, {q1, 2}, {q2q3, 1}] == D[SSS, {q1, 2}, {q2q3, 1}],
    D[SS, {q1, 2}, {q2, 2}] == D[SSS, {q1, 2}, {q2, 2}],
    D[SS, {q1q2, 1}, {q3q4, 1}] == D[SSS, {q1q2, 1}, {q3q4, 1}]},
   {M7,1, M7,2, M7,3, M7,4, M7,5, M7,6, M7,7}];
Expand[SSS - SS /. {Sols7[[1]]}];
(*Calculation of eigenvectors and decompositions of the vectors of interest*)
Mat = ϵ/9 {{M1,1, M2,1, M3,1, M4,1, M5,1, M6,1, M7,1},
     {M1,2, M2,2, M3,2, M4,2, M5,2, M6,2, M7,2}, {M1,3, M2,3, M3,3, M4,3, M5,3, M6,3, M7,3},
     {M1,4, M2,4, M3,4, M4,4, M5,4, M6,4, M7,4}, {M1,5, M2,5, M3,5, M4,5, M5,5, M6,5, M7,5},
     {M1,6, M2,6, M3,6, M4,6, M5,6, M6,6, M7,6}, {M1,7, M2,7, M3,7, M4,7, M5,7, M6,7, M7,7}} /.
   {Sequence @@ Sols1[[1]], Sequence @@ Sols2[[1]], Sequence @@ Sols3[[1]],
    Sequence @@ Sols4[[1]], Sequence @@ Sols5[[1]],
    Sequence @@ Sols6[[1]], Sequence @@ Sols7[[1]]};
```

```
MatrixForm[Mat]
eVL = Eigenvectors[Transpose[Mat]] (*Left eigenvectors of the matrix*)
Solve[{0, 0, 0, 0, 0, 0, 1} == Sum[c_i eVL[[i]], {i, 1, 7}], {c_1, c_2, c_3, c_4, c_5, c_6, c_7}]
Solve[{0, 0, 0, 0, 1, 0, 0} == Sum[c_i eVL[[i]], {i, 1, 7}], {c_1, c_2, c_3, c_4, c_5, c_6, c_7}]
```

Out[170]//MatrixForm=

$$\begin{pmatrix} -\epsilon & \frac{\epsilon}{6} & 0 & -\frac{\epsilon}{3} & -\frac{\epsilon}{12} & \frac{\epsilon}{24} & 0 \\ 0 & -\frac{\epsilon}{2} & 0 & -\epsilon & 0 & \frac{\epsilon}{6} & -\frac{2\epsilon}{3} \\ 0 & 0 & -\frac{\epsilon}{3} & 0 & -\frac{\epsilon}{12} & -\frac{\epsilon}{72} & -\frac{\epsilon}{9} \\ 0 & 0 & 0 & -\frac{4\epsilon}{3} & 0 & \frac{2\epsilon}{9} & -\frac{5\epsilon}{9} \\ 0 & 0 & 0 & \frac{\epsilon}{9} & -\frac{\epsilon}{2} & -\frac{\epsilon}{6} & -\frac{4\epsilon}{9} \\ 0 & 0 & 0 & -\frac{4\epsilon}{9} & 0 & -\frac{5\epsilon}{6} & -\frac{2\epsilon}{9} \\ 0 & 0 & 0 & 0 & 0 & -\frac{\epsilon}{12} & -\frac{2\epsilon}{3} \end{pmatrix}$$

Out[171]= {{0, 0, 0, 2, 0, −1, 2}, {−54, 18, 0, −3, −9, 0, 19},
{−84, 28, 0, −30, −14, 19, 0}, {0, 0, 0, 8, 0, −11, 36},
{0, −11, 0, 12, −9, 0, 28}, {0, −33, 0, 36, 1, 7, 0}, {0, 0, 28, −2, −14, 1, 12}}

Out[172]= $\left\{\left\{c_1 \to \frac{3}{7}, c_2 \to -\frac{7}{95}, c_3 \to \frac{9}{190}, c_4 \to \frac{3}{70}, c_5 \to 0, c_6 \to 0, c_7 \to 0\right\}\right\}$

Out[173]= $\left\{\left\{c_1 \to \frac{5}{7}, c_2 \to -\frac{14}{95}, c_3 \to \frac{9}{95}, c_4 \to \frac{17}{140}, c_5 \to -\frac{3}{28}, c_6 \to \frac{1}{28}, c_7 \to 0\right\}\right\}$

BIBLIOGRAPHY

[1] L. Onsager. Reciprocal relations in irreversible processes. i. *Phys. Rev.*, 37:405–426, 1931.

[2] A. Attanasi, A. Cavagna, L. Del Castello, I. Giardina, T. S. Grigera, A. Jelić, S. Melillo, L. Parisi, O. Pohl, E. Shen, and M. Viale. Information transfer and behavioural inertia in starling flocks. *Nat. Phys.*, 10:691–696, 2014.

[3] J. Toner and Y. Tu. Long-range order in a two-dimensional dynamical XY model: How birds fly together. *Phys. Rev. Lett.*, 75:4326–4329, 1995.

[4] A. E. Patteson, A. Gopinath, M. Goulian, and P. E. Arratia. Running and tumbling with e. coli in polymeric solutions. *Sci. Rep.*, 5, 2015.

[5] M. J. Schnitzer. Theory of continuum random walks and application to chemotaxis. *Phys. Rev. E*, 48:2553–2568, 1993.

[6] A. Walther and A. H. E. Müller. Janus particles. *Soft Matter*, 4:663, 2008.

[7] J. Palacci, S. Sacanna, A. P. Steinberg, D. J. Pine, and P. M. Chaikin. Living crystals of light-activated colloidal surfers. *Science*, 339:936–940, 2013.

[8] V. Narayan, S. Ramaswamy, and N. Menon. Long-lived giant number fluctuations in a swarming granular nematic. *Science*, 317:105–108, 2007.

[9] T. Vicsek, A. Czirók, E. Ben-Jacob, I. Cohen, and O. Shochet. Novel type of phase transition in a system of self-driven particles. *Phys. Rev. Lett.*, 75:1226–1229, 1995.

[10] R. Di Leonardo, L. Angelani, D. Dell'Arciprete, G. Ruocco, V. Iebba, S. Schippa, M. P. Conte, F. Mecarini, F. De Angelis, and E. Di Fabrizio. Bacterial ratchet motors. *PNAS*, 107:9541–9545, 2010.

[11] P. Galajda, J. Keymer, P. Chaikin, and R. Austin. A wall of funnels concentrates swimming bacteria. *J. Bacteriol.*, 189:8704–8707, 2007.

[12] M. E. Cates and J. Tailleur. Motility-induced phase separation. *Annu. Rev. Condens. Matter Phys.*, 6:219–244, 2015.

[13] J. Stenhammar, D. Marenduzzo, R. J. Allen, and M. E. Cates. Phase behaviour of active brownian particles: the role of dimensionality. *Soft Matter*, 10:1489–1499, 2014.

[14] J. Tailleur and M. E. Cates. Statistical mechanics of interacting run-and-tumble bacteria. *Phys. Rev. Lett.*, 100:218103, 2008.

[15] T. Speck, J. Bialké, A. M. Menzel, and H. Löwen. Effective Cahn-Hilliard equation for the phase separation of active Brownian particles. *Phys. Rev. Lett.*, 112:218304, 2014.

[16] T. F. F. Farage, P. Krinninger, and J. M. Brader. Effective interactions in active Brownian suspensions. *Phys. Rev. E*, 91:042310, 2015.

[17] É. Fodor, C. Nardini, M. E. Cates, J. Tailleur, P. Visco, and F. van Wijland. How far from equilibrium is active matter? *Phys. Rev. Lett.*, 117:038103, 2016.

[18] R. Wittkowski, A. Tiribocchi, J. Stenhammar, R. J. Allen, D. Marenduzzo, and M. E. Cates. Scalar phi4 field theory for active-particle phase separation. *Nat. Commun.*, 5:4351, 2014.

[19] Y. Fily and M. C. Marchetti. Athermal phase separation of self-propelled particles with no alignment. *Phys. Rev. Lett.*, 108:235702, 2012.

[20] G. S. Redner, M. F. Hagan, and A. Baskaran. Structure and dynamics of a phase-separating active colloidal fluid. *Phys. Rev. Lett.*, 110:055701, 2013.

[21] G. S. Redner, A. Baskaran, and M. F. Hagan. Reentrant phase behavior in active colloids with attraction. *Phys. Rev. E*, 88:012305, 2013.

[22] H. C. Berg. *Random Walks in Biology*. Princeton University Press, 1983.

[23] J. Toner and Y. Tu. Flocks, herds, and schools: A quantitative theory of flocking. *Phys. Rev. E*, 58:4828–4858, 1998.

[24] P. C. Hohenberg and B. I. Halperin. Theory of dynamic critical phenomena. *Rev. Mod. Phys.*, 49:435–479, 1977.

[25] U. C. Täuber. *Critical Dynamics*. Cambridge University Press, 2014.

[26] E. Tjhung, C. Nardini, and M. E. Cates. Cluster phases and bubbly phase separation in active fluids: Reversal of the ostwald process. *Phys. Rev. X*, 8:031080, 2018.

[27] L. S. Ornstein and F. Zernike. Accidental deviations of density and opalescence at the critical point of a single subtance. *KNAW Proc.*, 17:793–806, 1914.

[28] S. Ma and G. F. Mazenko. Critical dynamics of ferromagnets in $6 - \epsilon$ dimensions: General discussion and detailed calculation. *Phys. Rev. B*, 11:4077–4100, 1975.

[29] D. Forster, D. R. Nelson, and M. J. Stephen. Large-distance and long-time properties of a randomly stirred fluid. *Phys. Rev. A*, 16:732–749, 1977.

[30] D. J. Amit and V. Martín-Mayor. *Field Theory, the Renormalization Group, and Critical Phenomena*. World Scientific Publishing Co., 2005.

[31] M. E. Peskin and D. V. Schroeder. *An Introduction to Quantum Field Theory*. Westview Press, 1995.

[32] F. Caballero, C. Nardini, F. van Wijland, and M. E. Cates. Strong coupling in conserved surface roughening: A new universality class? *Phys. Rev. Lett.*, 121:020601, 2018.

[33] J. Krug. Origins of scale invariance in growth processes. *Adv. Phys.*, 46:139–282, 1997.

[34] M. Kardar, G. Parisi, and Y. Zhang. Dynamic scaling of growing interfaces. *Phys. Rev. Lett.*, 56:889–892, 1986.

[35] M. Eden. *Symposium on Information Theory in Biology*. Pergamon, New York, 1958.

[36] F. Family and T. Vicsek. Scaling of the active zone in the eden process on percolation networks and the ballistic deposition model. *J. Phys. A: Math. Gen.*, 18:L75–L81, 1985.

[37] J. Krim and G. Palasantzas. Experimental observations of self-affine scaling and kinetic roughening at sub-micron lengthscales. *Int. J. Mod. Phys. B*, 09:599–632, 1995.

[38] T. Sun, H. Guo, and M. Grant. Dynamics of driven interfaces with a conservation law. *Phys. Rev. A*, 40:6763–6766, 1989.

[39] D. E. Wolf and J. Villain. Growth with surface diffusion. *Europhys. Lett.*, 13:389–394, 1990.

[40] A. Chakrabarti. Computer simulation of stochastically growing interfaces with a conservation law. *Journal of Physics A: Mathematical and General*, 23(17):L919–L922, sep 1990.

[41] J. Krug. Classification of some deposition and growth processes. *Journal of Physics A: Mathematical and General*, 22(16):L769–L773, aug 1989.

[42] E. Marinari, A. Pagnani, G. Parisi, and Z. Rácz. Width distributions and the upper critical dimension of kardar-parisi-zhang interfaces. *Phys. Rev. E*, 65:026136, Jan 2002.

[43] J. M. Kim and S. Das Sarma. Discrete models for conserved growth equations. *Phys. Rev. Lett.*, 72:2903–2906, May 1994.

[44] A.-L. Barabási and H. E. Stanley. *Fractal Concepts in Surface Growth*. Cambridge University Press, 1995.

[45] T. Halpin-Healy. Diverse manifolds in random media. *Phys. Rev. Lett.*, 62:442–445, Jan 1989.

[46] J. P. Bouchaud and M. E. Cates. Self-consistent approach to the kardar-parisi-zhang equation. *Phys. Rev. E*, 47:R1455–R1458, Mar 1993.

[47] R. Manella. *Stochastic Processes in Physics, Chemistry, and Biology*. Springer, New York, 2000.

[48] B. Delamotte. *An Introduction to the Nonperturbative Renormalization Group*, pages 49–132. Springer Berlin Heidelberg, Berlin, Heidelberg, 2012.

[49] D. Squizzato and L. Canet. Kardar-Parisi-Zhang equation with temporally correlated noise: A nonperturbative renormalization group approach. *Phys. Rev. E*, 100:062143, 2019.

[50] T. J. Newman and A. J. Bray. Strong-coupling behaviour in discrete kardar - parisi - zhang equations. *J. Phys. A: Math. Gen.*, 29:7917–7928, 1996.

[51] M. F. Torres and R. C. Buceta. Numerical integration of KPZ equation with restrictions. *J. Stat. Mech: Theory Exp.*, 2018:033208, 2018.

[52] E. Sherman and G. Pruessner. Mounding in epitaxial surface growth. *arXiv*, 1204.3017, 2012.

[53] P. Meakin. The growth of rough surfaces and interfaces. *Physics Reports*, 235(4):189 – 289, 1993.

[54] C. Escudero. Geometric principles of surface growth. *Phys. Rev. Lett.*, 101:196102, Nov 2008.

[55] F. Caballero, C. Nardini, and M. E. Cates. From bulk to microphase separation in scalar active matter: A perturbative renormalization group analysis. *J. Stat. Mech.*, 123208, 2018.

[56] M. A. Srednicki. *Quantum field theory*. Cambridge University Press, 2010.

[57] G. Gompper and M. Schick. Self-assembling amphiphilic systems. In *Phase Transitions and Critical Phenomena*, volume 16. C. Domb, C. and J. L. Lebowitz, editors. Academic Press, 1994.

[58] S. A. Brazovskii. Phase transition of an isotropic system to a nonuniform state. *J. Exp. Theor. Phys.*, 41:85, 1975.

[59] G. H. Fredrickson and E. Helfand. Fluctuation effects in the theory of microphase separation in block copolymers. *J. Chem. Phys.*, 87:697–705, 1987.

[60] U. Seifert. Stochastic thermodynamics, fluctuation theorems and molecular machines. *Rep. Prog. Phys.*, 75:126001, 2012.

[61] J. L. Lebowitz and H. Spohn. A Gallavotti–Cohen-Type symmetry in the large deviation functional for stochastic dynamics. *J. Stat. Phys.*, 95:333–365, 1999.

[62] C. Nardini, É. Fodor, E. Tjhung, F. van Wijland, J. Tailleur, and M. E. Cates. Entropy production in field theories without time-reversal symmetry: Quantifying the non-equilibrium character of active matter. *Phys. Rev. X*, 7:021007, 2017.

[63] K. G. Wilson and M. E. Fisher. Critical exponents in 3.99 dimensions. *Phys. Rev. Lett.*, 28:240–243, Jan 1972.

[64] F. Caballero and M. E. Cates. Stealth entropy production in active field theories near ising critical points. *Phys. Rev. Lett.*, 124:240604, Jun 2020.

[65] T. Markovich et al. Manuscript in preparation.